

AD-A141 193

EXPERIMENTAL AND THEORETICAL STUDIES OF CREEP CRACK
GROWTH(U) MASSACHUSETTS INST OF TECH CAMBRIDGE
R M PELLOUX ET AL. 20 MAR 84 AFOSR-TR-84-0387

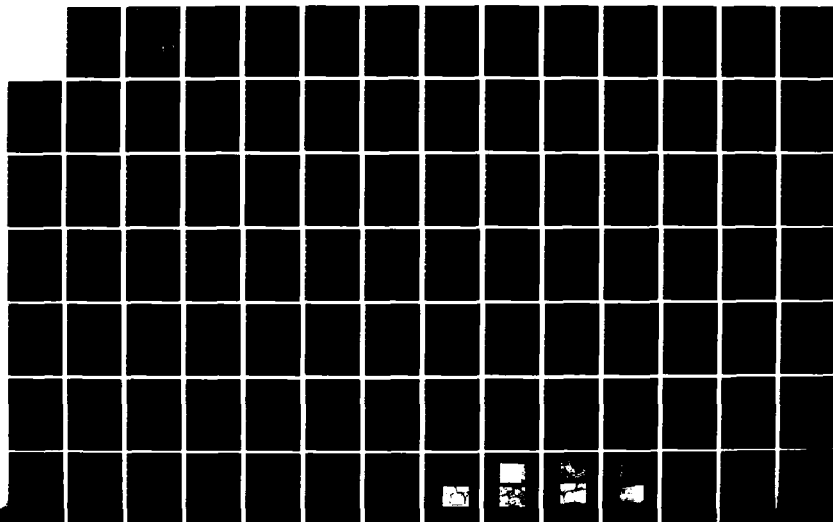
1/2

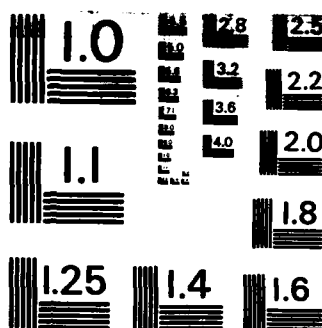
UNCLASSIFIED

AFOSR-82-0087

F/G 11/6

NL





MICROCOPY RESOLUTION TEST CHART
NATIONAL BUREAU OF STANDARDS-1963-A

UNCLASSIFIED

SECURITY CLASSIFICATION OF THIS PAGE (When Data Entered)

REPORT DOCUMENTATION PAGE

READ INSTRUCTIONS
BEFORE COMPLETING FORM

1. REPORT NUMBER AFOSR-TR-84-0387	2. GOVT ACCESSION NO.	3. RECIPIENT'S CATALOG NUMBER
4. TITLE (and Subtitle) Experimental and Theoretical Studies of Creep Crack Growth		5. TYPE OF REPORT & PERIOD COVERED Final
7. AUTHOR(s) Prof. Regis M. Pelloux Kenneth R. Bain Philippe Bensussan		6. PERFORMING ORG. REPORT NUMBER
9. PERFORMING ORGANIZATION NAME AND ADDRESS Massachusetts Institute of Technology Cambridge, MA 02139		8. CONTRACT OR GRANT NUMBER(s) AFOSR -82-0087
11. CONTROLLING OFFICE NAME AND ADDRESS Air Force Office of Scientific Research Bolling Air Force Base, DC 20332		10. PROGRAM ELEMENT, PROJECT, TASK AREA & WORK UNIT NUMBERS 61102F 2306/A1
14. MONITORING AGENCY NAME & ADDRESS (if different from Controlling Office)		12. REPORT DATE March 20, 1984
		13. NUMBER OF PAGES 141
		15. SECURITY CLASS. (of this report) UNCLASSIFIED
		15a. DECLASSIFICATION/DOWNGRADING SCHEDULE

DISTRIBUTION STATEMENT (of this Report)

FOSR/NE: ATTN. DR. A.H. ROSENSTEIN - 16 copies
FML/LLM: BRANCH CHIEF - 1 copy
FML/LLN - 1 copy Att: T. Nicholas

Approved for public release;
distribution unlimited.

DISTRIBUTION STATEMENT (of the abstract entered in Block 20, if different from Report)

SUPPLEMENTARY NOTES

DTIC
ELECTE

MAY 18 1984

E

19. KEY WORDS (Continue on reverse side if necessary and identify by block number)
creep crack growth rate, nickel base superalloys, high strength aluminum alloys, automated testing procedures, fracture mechanics, environment effects.
20. ABSTRACT (Continue on reverse side if necessary and identify by block number)
A two part research program was conducted to study the mechanics of creep crack growth in 1) nickel base superalloys as a function of alloy chemistry and test environment at 704°C; 2) a high strength aluminum alloy 2219-T851 at 175°C. The creep crack growth rate data is reported and analyzed in terms of fracture mechanics parameters. The automated test procedures used for the aluminum alloys are discussed in detail. An iterative model based on creep damage accumulation was derived to predict the creep crack growth rates.

DD FORM 1 JAN 73 1473 EDITION OF 1 NOV 65 IS OBSOLETE

UNCLASSIFIED

SECURITY CLASSIFICATION OF THIS PAGE (When Data Entered)

84 05 15 229

AFOSR-TR- 84 - 0387

FINAL REPORT

to

AIR FORCE OFFICE OF SCIENTIFIC RESEARCH

Project Manager: Dr. A. H. Rosenstein

Grant No. AFOSR 82-0087

EXPERIMENTAL AND THEORETICAL STUDIES OF CREEP CRACK GROWTH

AIR FORCE OFFICE OF SCIENTIFIC RESEARCH (AFSC)
NOTICE OF TRANSMITTAL TO DTIC

This technical report has been reviewed and is
approved for public release IAW AFR 190-12.

Distribution is unlimited.

MATTHEW J. KEEPER

Chief, Technical Information Division

Principal Investigator

Regis M. Pelloux

Professor of Materials Engineering
Department of Materials Science and Engineering
Massachusetts Institute of Technology
Cambridge, MA 02139

Research Assistants

Kenneth Bain
Philippe Bensussan

Approved for public release;
distribution unlimited.

March 1984

Table of Contents (cont'd)

	<u>Page</u>
1.1 Material and heat treatment.....	30
1.2 Microstructural characterization.....	30
1.3 Mechanical testing -- Specimen geometry.....	32
2. Experimental results.....	38
2.1 Mechanical properties--constitutive equations.....	38
2.2 Creep crack growth tests.....	39
2.3 Fractography of creep crack growth tests.....	42
3. Discussion.....	43
III. Conclusion.....	47
IV. Recommendations for additional research.....	49
Personnel.....	50
Technical Publications.....	51
References.....	52
Appendixes.....	58
Tables.....	
Figures.....	



Accession For	
NTIS GRA&I	<input checked="" type="checkbox"/>
DTIC TAB	<input type="checkbox"/>
Unannounced	<input type="checkbox"/>
Justification	
By _____	
Distribution/	
Availability Codes	
Dist	Avail and/or Special
A-1	

Table of Contents

	<u>Page</u>
I. Introduction.....	1
II. Literature Review.....	3
1. Creep crack growth of Nickel base superalloys.....	6
2. Effect of environment on CCG of Ni base superalloys.....	10
3. Creep crack growth in aluminum alloys.....	12
Part A: Creep crack growth of Nickel-base superalloys.....	15
1. Experimental procedures.....	15
1.1 Material and heat treatment.....	15
1.2 Microstructural characterization.....	15
1.3 Mechanical testing--specimen geometry.....	16
2. Experimental Results.....	19
2.1 Mechanical properties--constitutive equation.....	19
2.2 Creep crack growth tests.....	20
2.3 Fractography of creep crack growth tests.....	21
2.4 Creep crack initiation tests.....	22
3. An iterative model for CCG prediction.....	22
3.1 Stress calculation.....	23
3.2 The accumulation of creep strain.....	25
3.3 Environmental considerations.....	27
4. Discussion.....	27
Part B: Creep crack growth in 2219 aluminum alloys.....	30
1. Experimental procedures.....	30

I. INTRODUCTION

Cracks can nucleate and propagate in metals and alloys at high temperature under the influence of creep damage, fatigue damage and/or environment induced damage. Until recently, a large majority of high temperature components, such as superalloy jet-engine parts, low-alloy and stainless steel assemblies in conventional and nuclear power plants, and titanium and aluminum components in hot sections of aircraft structures, were designed with high temperature fracture data based on smooth-bar and notched-bar stress rupture test results. In such tests, fracture is caused by the nucleation and propagation of multiple cracks in initially defect free specimen. The present trend toward an emphasis on higher and higher performance has led to designs with low safety factors. Components life in service may then be limited by the propagation of pre-existing defects.

The need to develop reliable methods to estimate the remaining life of parts containing cracks has motivated extensive research programs on high temperature crack propagation, and in particular, on Creep Crack Growth, i.e., the propagation of a single macroscopic crack under sustained load at temperatures well within the creep regime. [1-5]

In the case where creep damage only is present, it is now well established that a crack propagates by nucleation, growth and coalescence of intergranular cavities on grain boundaries lying ahead of the crack tip [1], [6], [7], [8], [9], [10], [11], [12], [13]. Whether the role of an aggressive environment is to accelerate one of these stages or to cause damage of a completely different nature is still not clear in all cases [13]. A strong emphasis has been put on the determination of load-geometry parameters which would provide unique correlations with the creep crack

growth rates. Such correlations are obviously essential to transfer test results to engineering situations. In spite of the large amount of work performed in this direction, this area of research is still highly controversial. In order to optimize the microstructure of alloys to improve their resistance to creep crack growth, an understanding of the micromechanisms of crack growth is also required. In addition, such a knowledge may substantiate the validity of extrapolations of test data.

The significance of environment in the materials resistance to creep crack growth has been identified and documented in detail. The environmental effect is a function of numerous parameters, such as, alloy system, heat treatment and microstructure, chemistry, temperature and loading history. Several mechanisms have been proposed to explain the experimental results, but none has been conclusively proven. The exact micromechanisms responsible for the environmental effect and their kinetics are still poorly understood. Only with further investigation, we will be able to obtain more insight in the physics and the mechanics of these processes.

The following research was performed to investigate the effect of test procedures, alloy system and environment on Creep Crack Growth. This study was primarily concerned with:

- The applicability of fracture mechanics concepts to Creep Crack growth.
- The environmental effect on Creep Crack Growth.
- The identification of the micromechanisms of Creep Crack Growth.
- The prediction of creep crack growth rates for different alloy systems.

II. LITERATURE REVIEW

Creep crack growth has been extensively studied in aluminum alloys, titanium alloys, nickel, iron and cobalt base superalloys, carbon steels, chromium molybdenum-vanadium and in stainless steels. The effects of the test temperature, the test environment, alloy heat treatment and micro-structure have been reported for some of these alloys.

Creep crack growth rates have been correlated using the stress intensity factor (K), the crack opening displacement (COD), the J-Integral for plasticity (J), the C^* -integral for time dependent plasticity (C), and the net section stress (σ_{net}). Several studies have been published comparing the practical applicability of these correlating parameters (15,16,17,18,19, 20,21).

Materials susceptible to creep crack growth (CCG) can be said to be either creep brittle or creep ductile. Creep brittle materials fail by CCG with almost no bulk creep deformation, while creep ductile materials fail by CCG with extensive bulk creep deformation, even under initial small scale yielding loading conditions. For example it has been shown that nickel base superalloys are creep brittle at temperatures as high as 760°C and 304 stainless steel is creep ductile at temperatures as low as 538°C. The distinction between these two extreme behaviors can be rationalized to a certain extent by using concepts of fracture mechanics of creeping solids.

Creep crack growth tests have been performed using various specimens under tensile and/or bending loading modes, such as center crack (CC), single edge notch tension (SEN(T)), single edge notch bend (SEN(B)), double edge notch (DEN), compact tension (CT), double cantilever beam (DCB) and wedge opening load (WOL) specimens. For given loading conditions, the creep crack

growth rates have been found to be very sensitive to the degree of stress triaxiality in the crack plane (22,18,23). Crack front tunnelling and specimen size dependence of the creep crack growth rates have been observed when specimens with low constraints have been used (e.g., 18,40,24,25). Thick or side grooved specimens in which the through-thickness deformation is constrained over most of the thickness of the specimen have thus been often selected (e.g., 18,27,17,26-30). Both side groove depth and side groove root radius are of importance in the increase of the constraints over the specimen net section. The effect of the side groove depth only and not of the side groove tip radius has, to our knowledge, been reported in the literature.

The creep crack growth rates show in general a three stage behavior similar to the one described in figure 1 when they are reported on a log-log plot da/dt versus either K (e.g., 18,32,17,21,20,33,31-35), C^* (e.g., 18,32,37,38,39,17,21,30,31), σ_{net} , σ_{ref} (e.g., 53,64,66,68,52,103) or a displacement rate (e.g., 31) for tests where the loading parameter of interest increases. The creep crack growth rates can be fitted in each stage to a power law (32):

$$\frac{da}{dt} = D X^n \quad (L-1)$$

where X is the loading parameter of interest. Stage I corresponds to an initial transient where da/dt varies very rapidly with the loading parameter. A very high exponent n for X is thus expected in this stage. No unique correlation between a loading parameter and the creep crack growth rates can be expected in this regime since stage I has been shown to depend strongly on the applied load and on the initial conditions (32,33,34). This is not the

case for stage II (32,33,34) where there is a unique correlation between the creep crack growth rates and a loading parameter, when specimens with "high enough" constraints and "low enough" loading parameter gradients are used. A lower exponent n than in stage I is usually found in stage II. Finally, the creep crack growth rates accelerate very rapidly in stage III which corresponds to the onset of unstable fast fracture and which lasts for a negligible fraction of the life of the specimen.

The creep crack growth rates have also been sometimes observed to first decrease and then increase during stage I for constant load tests (40,1,24, 19,41) as well as for constant stress intensity factor tests (43,42,19,61,77, 59).

A unique correlation between da/dt and a loading parameter may thus be valid only over a fraction of the life of a specimen. Such a correlation is thus not sufficient to estimate the total life of a cracked component, and the component size and geometry, the initial conditions and the load parameter history may also be required. Correlations between the time to failure by creep crack growth and the initial stress intensity factor for nickel base superalloys (18,17,34,44,45), the initial C^* -integral for 316 stainless steel, and the reference stress for Cr-Mo-V steels (27,23), have also been reported. A threshold initial stress intensity factor below which no creep crack growth could be experimentally detected has been also determined in some cases (18,17,34,44). Some typical experimental results which are summarized in Table I and which are concerned more specifically with the determination of creep crack growth rate correlations in structural alloys are discussed now.

II-1 Creep Crack Growth in Nickel - Base - Superalloys

Creep crack growth has been studied in most nickel base superalloys, namely Astroloy (33,34,46,47,14), Udimet 700 (18,13,48,4), IN 100 (33,34,49,50), Merl 76 (33,51,52), IN 792 (34,44,46,104,109,111), Rene 95 (33,34,45,46), Inconel X-750 (48,41,4,53), Inconel 600 (41), Inconel 625 (41), IN 718 (13,17,48,34,36,4,46,4,95,104,106,111,4), Inconel 738 (54), Nimonic 105 (54), Nimonic 115 (34,46), AF 115 (51), Nimonic PE 16 (41), Waspaloy (34,35,46), and MAR-M432 (B6) (51). Information about the testing conditions, the specimen sizes and geometries, the range of crack growth rates, the proposed loading parameters to correlate with the creep crack growth rates for all these alloys are succinctly listed in Table I. These alloys were either P/M HIP (e.g., 33,19,44-47,14,96,54,109-112,14,51,52), wrought (44,46,54) or cast (54). Specimen blanks cut from hot rolled plates, castings, forgings or extruded rods were used (see Table I). The creep crack growth tests were performed mostly in the 650°C-760°C range, and at temperatures as high as 850°C for Udimet 700 (18,13,48,4), Inconel 738 (54) and as low as 540°C for Inconel X-750 (48,41,4), Inconel 600 (41), and Inconel 718 (47,13,48,34,46,46,4), and even as low as 425°C for Inconel 718 (46). An increase of the creep crack growth rates with temperature has been observed for most alloys except for Inconel 625 (41). In the cases where the effect of the test environment was also assessed, the creep crack growth rates were found to be higher in air than in inert environments (vacuum, He or Ar atmospheres) by several orders of magnitude in Rene 95 (33, 45), in Inconel 718 (13,48,36,46) and in Inconel X-750 (48,41,4,53,55) for example (see figure 2). The creep crack growth rates were shown to be only slightly sensitive to the test environment in Astroloy (48,47,14) (see figure 2) in Udimet 700 (48) and in

Nimonic PE16 (41). Modifications of the chemical composition of these alloys were found to have significant effects on the creep crack growth rates (51), and in particular, minute additions of some elements which segregate to the grain boundaries such as B, Zr and Hf were shown to improve the alloy resistance to air embrittlement (33,51). A more detailed review of the environmental effect in Ni-base Superalloys will be given in the next section. Correlations between the resistance of alloys to creep crack growth and their processing history (44), their heat treatment (13,34,44,46,56) and the associated microstructural characteristics such as grain size (33,44,46), grain boundary morphology (44m 46m 50), and grain boundary precipitate size and distribution (56) have also been studied.

Creep crack growth tests were performed using either side-grooved or non-side-grooved specimens (See Table I). Severe crack front tunnelling was observed for Inconel 718 at 650°C in CT specimens as thick as 25 mm (47,48), for IN 100 at 730°C in CT specimens as thick as 18 mm and in ring specimens as thick as 6 mm (19) and for Mar1 76, AF11 and MAR-M432 (B6) in CC specimens (51). Yet, cracks were found to grow with only a slight crack front curvature in Inconel X-750 at 540-650°C and in Udimet 700 at 850°C in specimens thicker than 12.5 mm (48). Crack tip tunnelling was not observed or reported when specimens with at least 5 to 10% side grooves were used.

All nickel base superalloys appear to be creep brittle for the testing conditions described above and listed in Table I. It is only at high temperature above 800°C that some alloys have been observed to become creep ductile (41). Creep crack growth rates have been almost always correlated with the stress intensity factor. The question of the validity of the choice of the stress intensity factor to correlate with the creep crack growth rates

has been addressed only in a few studies which are reviewed now.

When reported as a function of the stress intensity factor, the creep crack growth rates in the state II regime for a given specimen size and geometry have been shown to be somewhat independent of the applied load and of the initial stress intensity factor (18,17,13,48,33,34,19,49,59,50). The creep crack growth rates in stage I have been found to depend very strongly on the applied load and on the initial stress intensity factor (18,17,13,48,33,34,19,49,50). A correlation of the creep crack growth rates with the stress intensity factor can thus be valid only in the stage II regime of creep crack growth.

There was no specimen size effect for IN 718 at 650°C in CT specimens of thickness ranging from 2.6 mm up to 25.4 mm (13,4). The creep crack growth rates in IN 100 at 730°C were observed to increase with the specimen thickness when 6 mm to 18 mm thick CT specimens or 3 mm to 6 mm thick Ring specimens were used (19). An upper bound for the creep crack growth rates was nevertheless reached for CT specimens thicker than 15 mm (19). An opposite trend has been reported for IN 718 at 540°C and 650°C where the creep crack growth rates were found to be lower in 25 mm thick than in 19 mm thick CT specimens (17). These results cannot however be considered as conclusive since the thin and thick specimens were respectively machined from stocks taken from two different heats (17).

Creep crack growth rates have been measured using different specimen geometries in Astroloy, IN 100, Merl 76, Rene 95, Inconel X-750 and Inconel 718 (see Table I). Given the sensitivity of the creep crack growth rates to the alloy processing variables, comparisons of data from different studies where these parameters are not precisely described may be hazardous. Creep

crack growth tests were performed in IN 100 at 650°C using side grooved constant-K DCB specimens and CC specimens machined from the same batch of material (49). Comparable creep crack growth rates were measured for a given stress intensity factor in the stage II regime for the CC specimens and in the steady state regime for the DCB specimens, independently of the initial crack length. It was thus concluded that the stress intensity factor correlated with the creep crack growth rate in IN 100 at 650°C (49).

A fair correlation was also found between the creep crack growth rates in IN 100 at 730°C and the stress intensity factor for crack growth tests performed under constant applied load in CT specimens and ring specimens in which K is almost constant (19) although both types of specimens came from different forgings.

A three stage behavior was also observed when the creep crack growth rates for constant load tests in CT specimens in Inconel 718 at 540-760°C (17) and in Udimet 700 at 850°C (18) were plotted as a function of the nominal stress. The scatter for tests performed with specimens of different thicknesses and under different constant applied loads was found to be more significant than when the stress intensity factor was used (18,17). The creep crack growth rates were also tentatively correlated with the C^* -integral estimated by Landes and Begley's multi-specimen method (84) adapted to constant load tests. Only a few results were reported for Inconel 718 (17) and no conclusions could really be drawn. The creep crack growth rates in Udimet 700 versus the C^* -integral for different tests gave totally separate curves (18,14). Correlations of the creep crack growth rates with the stress intensity factor, the net section stress and the C^* -integral calculated by Landes and Begley's method were tried for IN 100 at

730°C for constant load tests in CT specimens and ring specimens of different thicknesses (19). All these parameters were found to correlate with the creep crack growth rates measured in the CT specimens (19). Nevertheless, the creep crack growth rates were observed to reach a constant steady state value in the ring specimens where K remains approximately constant, although the net section stress was shown to increase (19). The net section stress and the C^* -integral were however shown to have a doubtful physical meaning in the ring specimens (57). More consistent results were also obtained when the creep crack growth rates in Astroloy, IN 792, Inconel 718, Nimonic 115, Rene 95, and Waspaloy at 700°C were correlated with the stress intensity factor rather than with the net section stress for constant load tests using CT specimens (34). Too few experimental results were presented to justify a comparison of the stress intensity factor with the C^* -integral as a correlating parameter.

The stress intensity factor appears however to be the best load-geometry parameter to correlate with the stage II creep crack growth rates in nickel base superalloys under most experimental conditions. This result could be expected since these alloys are creep brittle at temperatures as high as 760°C and even higher.

II.2 Effect of environment on CCGR of Ni-base Superalloys

The effect of oxygen on the CCGR has been studied by Huang (14) on Astroloy, Sadananda and Shahinian (4,5) on In-718, X-750, and Udimet 700, Pineau (58) on IN-718, and by Floreen (59) on PE16, and Bain (60) on Rene-95. The effect of oxygen on CCGR ranges from only a slight increase in CCGR for Astroloy to a 1000 times increase in the CCGR for IN-718 and Rene-95.

Figure 2 shows the range of air and inert environment results for several Ni-base alloys at 650°C. The CCGR results in an inert environment are in a narrow range of CCGR well below the air results. This is not surprising since all the alloys have essentially similar creep and tensile properties at this temperature. The CCGR in air were much faster than in an inert environment but the amount of increase in the CCGR varies significantly from alloy to alloy. The effect of oxygen on CCGR depends strongly on each alloy's ability to resist oxygen embrittlement.

Embrittlement by oxygen in Ni-base alloys at temperatures above 500°C results in marked decrease in the creep-rupture life (61), and a decrease in notched stress rupture life (62), lower fracture ductility (63), an increase in fatigue crack growth rates (64), and in creep crack growth rates (5).

While the embrittlement of nickel-base alloys by oxygen has been observed, the mechanism by which oxygen causes embrittlement remains unknown. Several theories have been put forth to explain oxygen embrittlement. These theories are:

1. Reduction of surface energy at $\gamma - \gamma'$ interfaces (65)
2. Complex oxide formation along grain boundaries (66,67)
3. Carbon dioxide bubble formation (68)
4. Sulfur release due to oxidation of grain boundary sulfides. (69,70)

All of the above embrittlement mechanisms depend on the diffusion rates of oxygen along grain boundaries. Elements which segregate to grain boundaries and reduce the number of vacancies can be expected to reduce the diffusivity of oxygen along grain boundaries. Alloying additions which increase the cohesive strength of the carbide-g.b. interface will inhibit the

nucleation of grain boundary cavities and reduce the amount of embrittlement in the alloy by oxygen.

11.3. Creep Crack Growth in Aluminum Alloys

Creep crack growth rates have been measured in 2219-T851 aluminum alloy at 150°C in non side-grooved CT specimens under different loads and different initial stress intensity factors by Kaufman et al. (24) (see figure 3). Only one specimen geometry was used, and, in spite of a specimen thickness of more than 5 cm, extensive crack front tunnelling was observed. A good correlation between K and da/dt independent of the load and the initial K was found in stage II. The results of a study of creep crack growth in 2219-T851 at 175°C presented in reference (22) are described and discussed in the results and discussion sections of this thesis.

Creep crack growth has been studied in RR58 aluminum alloy in the temperature range 100-200°C by Webster and co-workers (43,72,42,25,30) (see figure 3). Tests have been performed on side grooved constant- K DCB specimens and on side grooved DCB specimens with parallel faces of similar dimensions. The crack growth rates were found to vary during constant- K tests, but a correlation between the minimum creep crack growth rate and the stress intensity factor was determined (25). Two specimen thicknesses were used (9.5 and 25 mm) and the minimum creep crack growth rates for a given K were lower in the thinnest specimens where crack front tunnelling was observed in spite of the presence of side grooves (25). Yet, no unique correlation could apparently be determined between K and the creep crack growth rates measured in both types of DCB specimens (72,15) though RR58 was observed to be creep brittle (15,57). The creep crack growth rates measured during constant- K

tests were found to correlate very well however with the C^* -integral calculated analytically according to the non linear beam theory (43,42). Constant crack growth rates were measured in tests where the load was adjusted in order to maintain C^* constant. Unfortunately, no unique correlation could be obtained between this analytical C^* -integral and da/dt measured in specimens of different sizes and geometries (72). This analytical calculation of C^* is however not valid for RR58 in the 100-200°C range of temperatures since the singularity at the crack tip cannot be neglected. As a matter of fact, Branco and Radon (57), have shown that the rotation of the specimen arms around a plastic hinge at the crack tip has to be taken into account in addition to the bending deformations in order to be able to predict load point displacements which match the experimental displacements measured by Webster and co-workers (25). The best specimen size and geometry independent correlation of the creep crack growth rates was found with the C^* -integral calculated by the approximate experimental method using load and displacement rate data recorded during the crack growth tests according (72,15,30). Although the creep crack growth rates for a given value of the C^* -integral were found to be somewhat independent of the specimen thickness (30), they were shown to increase by a factor of about 2 when the constraints were significantly increased as the specimen net section was decreased from 80% down to 50% of the specimen thickness (30). Since the creep component of the total displacement in these creep crack growth experiments has been estimated as being a fraction of the total displacement, smaller than 6% at temperatures lower than 150°C and smaller than 24% only at 200°C (15), this excellent correlation may be no more than a correlation between da/dt and da/dt itself. The exponent $n = .9$ determined for this correlation is in agreement with this

conclusion.

Creep crack growth tests have been performed in 6061 aluminum at 220, 275 and 325°C using non side grooved CT specimen, grooved CT specimens under constant load (73,94) (see figure 3). No unique load-independent correlation was found between the creep crack growth rates and either the stress intensity factor, the net section stress, the reference stress (73), or the load point displacement rate (73,94). An apparent correlation was nevertheless determined between da/dt at 220°C and the C^* -integral with $n = 0.9$ when C^* was calculated either according to the non-linear beam theory or according to the dimensional analysis for deeply cracked CT specimens. The $\frac{da}{dt}$ versus C^* curves were shown to be actually distinct for different loads (58). A good correlation was however found between the creep crack growth rates and the C^* -integral estimated by Landes and Begley's multi-specimen method, with $n = 1.0$, assuming that a unique relation existed between da/dt and $\dot{\Delta}$ independently of the applied load (73). The creep crack growth rates were shown to be nevertheless proportional to the empirical parameter $(\dot{\Delta}/P^\alpha)^{1/\theta}$ where both α and $1/\theta$ increase with temperature (73,94). Consequently, the load dependence of the da/dt versus $\dot{\Delta}$ correlation is more pronounced as the temperature is increased which agrees with an expected enhancement of the creep ductility of 6061 aluminum alloy as the temperature is raised.

Part A: Creep Crack growth of Ni-base alloys

A.1 Experimental procedures

A.1.1. Material and heat treatment

Four γ/γ' nickel base superalloys were chosen for this study. They are Low Carbon Astroloy, Merl-76, Low Carbon IN-100, and Rene-95. The alloys were produced by HIP processing of PM alloys into 9/16" diameter rod. These alloys were chosen for study as a result of the varying susceptibility to grain boundary embrittlement in oxygen. The powder mesh size for each alloy is shown in Table II along with the particle diameter. Rene-95 was obtained in two mesh sizes.

Table III describes the thermal and HIP processing given to the alloys used in this study. The heat treatment was chosen to give the alloys similar mechanical properties.

The chemistries for the alloys are shown in Table IV. The calculated γ' volume fraction for each alloy is also given in Table IV [74].

A.1.2. Microstructural characterization

Several samples of heat treated material were mounted in Buehler plastimet, ground on 240, 320, 400, and 600 grit silicon carbide paper, then ground with three μm paste on nylon cloth and finally polished with Nalcoag 1060 (colloidal silica solution) on nylon cloth. The specimens were etched using No. 2 stainless reagent (100 ml methanol, 50 ml HCl, and 5 gm FeCl_3).

The etched specimens were observed under both a Zeiss Universal optical microscope and an AMR-1000 A scanning electron microscope. Figures 47 show the after heat treatment microstructures of Astroloy, Merl-76, In-100, and Rene-95 respectively. IN-100 and Astroloy have coarse grain size with

carbides decorating the grain boundaries. Merl-76 and Rene-95 have a finer grain size with large primary particles along the boundaries.

A.1.3 Mechanical Testing - Specimen geometry

Tensile, creep, creep rupture, notched stress rupture, and creep crack growth tests were performed at 704°C on all four alloys. The test procedures for these tests are described in the following sections.

Tensile Testing

Testing was performed using an Instron Tensile Machine. The test was performed at 704°C at a displacement rate of .02 inches per minute. An A.T.S. three-zone resistance heater with a Leeds and Northrup Electromax III temperature controller was used for heating the specimen. Load versus displacement was recorded using a strip chart recorder incorporated in the Instron machine. Yield stress (.2 per cent) and ultimate tensile strength were determined graphically. Total elongation and reduction of area were measured directly on the failed bar.

Smooth Bar Creep Testing

Tests were conducted to obtain the minimum creep rate versus stress at 704°C. Creep rate tests were conducted at 704°C within the stress range from 650 to 1050 MPa. Temperature control was accurate to within $\pm 4^\circ\text{C}$ within the specimen gauge section. The elongation was measured using an extensometer connected to a dc-dc LVDT with a .25 inch range from 0 to 100 mV. Tests were conducted using an A.T.S. level arm tester. The steady state creep rate was recorded at each stress level. The stress was increased in steps in order to obtain several stress and steady state creep rate points per specimen. Several smooth bars were tested at one stress level and the time to rupture was recorded along with the minimum creep rate.

Notched Stress Rupture Testing

The specimen geometry is shown in Figure 8. The stress concentration factor is $K_t = 3$ (60° flank angles, and root radius .013 inch). Tests were conducted at 704°C in air using the same A.T.S. level arm testing system and temperature controller. Only time to rupture was recorded at various stress levels.

Creep Crack Growth Rate Testing

Creep crack growth rate tests were conducted at constant load using a level arm tester supplied by Applied Testing System Company (ATS). Temperature was controlled within $\pm 4^\circ\text{C}$ within the gauge section of the specimen using a 3-zone resistance heater. Tests were conducted in two environments: in air and in an inert environment of 99.999 percent pure argon. A retort supplied by ATS was used in the argon tests. Argon tests were conducted at an over pressure of 5 psig in order to insure no back streaming of air.

A single edge-notched test specimen is used in the creep crack growth rate tests. (Figure 9). This specimen has side grooves to prevent crack tip tunnelling as a result of the slower creep crack growth rate in the plane stress condition which would otherwise exist on the specimen surface.

A starter notch is cut using a 150 mm thick diamond saw. Specimens were fatigue precracked at room temperature. The maximum stress intensity, K , used in precracking is less than the initial stress intensity used in subsequent creep crack growth testing.

Crack length Measurement Technique

Crack length is measured using the d.c. electrical potential technique (75,76). The short crack length and large range of crack length/width

ratio afforded by the SEN specimen geometry gives a resolution of 10 μm change in crack length. A 30 amp constant d.c. current is passed through the specimen and the potential across the crack mouth versus time is recorded.

Each specimen is individually calibrated using the initial and final crack lengths and d.c. potentials. This removes the variation in crack length determination as a result of the uncertainty in the potential probe spacing, Y . The theoretical solution by Johnson (77) was used to calibrate the crack length time from the d.c. potential:

$$\frac{V_a}{V_{a_0}} = \frac{\cosh^{-1} \left[\frac{\cosh(\pi Y/2W)}{\cos(\pi a/2W)} \right]}{\cosh^{-1} \left[\frac{\cosh(\pi Y/2W)}{\cos(\pi a_0/2W)} \right]}$$

where V_a is the initial potential across the crack mouth, Y is one-half the potential load spacing, W is the specimen width, and a_0 is the initial crack length.

The stress intensity factor, K , for the SEN specimen is given by the formula suggested by Brown and Shrawly (78).

$$K_I = \sigma \sqrt{\pi a} \left(1.12 - 0.23 (a/w) + (a/w)^2 - 21.7 (a/w)^3 + 30.4 (a/w)^4 \right)$$

where:

K = the stress intensity factor

σ = the gross section stress

a = the crack length

w = the width of the specimen

This equation is for a single edge notched specimen which is free to bend.

The gross section stress for a notched specimen with side grooves is given

as (see Appendix I) (79).

$$\sigma = \frac{P}{W \sqrt{bb_{\text{net}}}}$$

where:

P = applied load

b = gross thickness

b_{net} = net section thickness

A.2 Experimental Results

A.2.1 Mechanical properties constitutive equation

A tensile test at 704°C was conducted for each alloy. The tensile test results are shown in Table V. The U.T.S., .2% Y.S., and Elastic Modulus for all the alloys are approximately the same. The percentage elongation varies by a factor of three from 5.0% for Rene-95 to 15.4% for Astroloy. The specimens with low ductility exhibited failure by the propagation of surface cracks. The plastic strain hardening exponent N_p and proportionality constant B are also given in Table V ($\sigma = B_p (\epsilon_p)^{N_p}$).

The steady state creep rate for each alloy was measured in air at 704°C for a range of applied stresses from 600 to 1100 MPa. The results are shown in Figure 10 in a plot of stress versus steady state creep rate. The exponent and constant from the secondary creep rate equation are also shown. ($\sigma(\text{MPa}) = B_c (\dot{\epsilon}_s)^{N_c}$). In the range of steady state creep rate from 10^{-8} sec^{-1} to 10^{-4} sec^{-1} . The behavior of the four alloys is the same. Only Rene-95 exhibits a slight increase in the creep exponent.

A.2.2 Creep Crack growth tests

Creep Crack Growth Results

Creep crack growth tests were performed in air and 99.999% pure argon on all four alloys. The creep crack growth rates at 704°C for PM/HIP low carbon Astroloy, Merl-76, IN-100, Rene-95 (60 mesh size) and Rene-95 (120 mesh size) are shown in Figures 11 through 15 respectively.

All the curves have the same general shape shown in Figure 1: an initial transient stage which is strongly dependent upon the initial loading condition, a second stage where a good correlation between da/dt and K exists for all the alloys tested in both air and argon. The scatter is within one half an order of magnitude in CCGR.

The effect of the initial stress intensity factor was studied more systematically in Merl-76. The initial stress intensity factor K_i , was varied from $K_i = 14.2 \text{ MPa } \sqrt{\text{m}}$ to $43.2 \text{ MPa } \sqrt{\text{m}}$ for PM/HP Merl-76 at 704°C in an air atmosphere (Figure 16). The initial transient behavior, Stage I cracking, does not correlate with K . The relative time spent during stage I was also function of the K_i . It was usually observed that the extent of stage I cracking decreased as the value of the initial stress intensity factor was decreased.

A comparison of CCGR versus K curves for all the alloys in air at 704°C is given in Figure 16. The results indicate that all the alloys exhibit CCGR between 10^{-7} m/s to 10^{-5} m/s in a range of K from 20 to 100 $\text{MPa } \sqrt{\text{m}}$. The slopes in the stage II region of the curves vary from 2 to 4. Astroloy and Merl-76 have the lowest CCGR in air while Rene-95 (60 and 120 mesh) and IN-100 have the fastest CCGR.

In all the alloys the fracture path is totally intergranular. Fracture

surfaces in Astroloy have intergranular prior particle boundary cracking at K greater than $60 \text{ MPa} \sqrt{\text{m}}$.

A comparison of the CCGR versus K curves for all the alloys in argon at 704°C is shown in Figure 4.10. The CCGR in argon are compared to the air results in Figure 18. The CCGR for all the alloys is higher in air than in argon. The slopes of the stage II region of crack growth in argon is higher than in air and it ranges from 3.5 to 6. Astroloy has the lowest CCGR at low K , but Merl-76 becomes slower at higher K values. Rene-95 (120 mesh) and IN-100 have the fastest CCGR in argon at all values of K .

The fracture path in argon is intergranular, along grain boundaries which are also along the prior powder particle boundaries.

A.2.3 Fractography of CCG tests

Fracture surfaces were observed for both air and argon CCGR tests using an AMR-1000 Scanning Electron Microscope. The fracture path was intergranular for all CCGR tests. In the argon CCGR tests the crack followed prior powder particle boundaries. The prior particle boundaries in PM/HIP alloys are heavily decorated with carbides. Figure 19 shows the fracture mode of PM/HIP low C Astroloy at 704°C tested a) in air and b) in pure argon. The fracture surface shows more grain boundary cavitation in argon than in air as is shown in Figure 19. In air, the fracture path follows both prior powder particle boundaries and grain boundaries which cut through the particles (Figure 20). This is specially the case for high K values and fast crack growth values. The fracture surfaces of Low C IN-100 and Rene-95 tested in argon are shown in Figure 21. Figure 22 shows the fracture surface of Rene-95 in air at 704°C .

A.2.4 Creep crack initiation tests

The SEN specimens used in the Creep Crack growth testing were fatigue precracked prior to testing at high temperatures. A long initiation time was observed in case where the specimens were not fatigue precracked and it became apparent that the creep crack propagation time represented only a small fraction (up to 10%) of the total life of the specimen. It was thus desirable to investigate any existing correlation between the creep crack initiation times and the propagation behavior of these materials. A series of notched stress rupture tests were performed at 704°C in air and the results are presented in Figure 23. For the specimen geometry used, it was satisfactory for a first order approximation to assume that the rupture time was equal to the initiation time. The results indicated that Rene-95 had a shorter rupture time than the other three alloys tested which was in accordance with the fastest creep crack growth rates of Rene 95. At high stress Merl-76 gave the longest time to rupture, but at lower stress a crossover occurs and Astroloy has the longest time to rupture. Similar picture was also observed in the creep crack growth behavior of these alloys. (Figure 17). Thus the NSR results can be interpreted as giving a measure of the relative CCGR behavior of the four alloys when tested in air.

A.3. An iterative model for creep crack growth prediction

A simple iterative model for creep crack growth was developed based on the accumulation of damage ahead of the crack tip for a specimen of a creep brittle material under conditions of small scale yielding. The basic assumptions involved in the derivation of the model are the following:

1. Creep crack advance is the result of creep damage accumulation in a

process zone ahead of the crack tip. Damage is expressed as creep strain accumulation in elements of the size of the critical microstructural parameters (i.e. grain size for air tests and prior powder particle size for argon tests).

2. The crack advances by one element when the element immediately ahead of the crack tip achieves a critical value of creep strain.
3. The effect of environment is taken into account by reducing the critical value of creep strain.
4. The rate of creep strain accumulation is calculated by using the material constitutive equations and the stress distribution ahead of the crack tip described by fracture mechanics concepts for creeping solids.

A brief description of the model follows. Emphasis has been paid on the calculation procedures and the criteria for crack advance.

A.3.1 Stress Calculations

- At time $t=0$:

The stress in far field is σ_0 . Closer to the crack tip, at radius "r" the stresses are described by the elastic stress intensity factor, K_I (80).

$$\sigma_E = \frac{K_I}{\sqrt{2\pi r}} f_E(\theta) \quad (A.1)$$

where: σ_E = equivalent stress

$f_E(\theta)$ = factor that depends only on the angle (θ) from the plane of the crack.

r = distance from crack tip

The equivalent stress, σ_E , in the plastic region ahead of the crack tip is given by the HRR singularity (81,82)

$$\sigma_E \propto \left[\frac{K^2}{r} \right]^{[1/(Np+1)]} \quad (A.2)$$

where: Np is the stress exponent of the plasticity constitutive equation:

$$\dot{\epsilon}^P = Bp(\sigma)^{Np} \quad (A.3)$$

where: $\dot{\epsilon}^P$ is the plastic strain

- At time $t > 0$:

The stresses in the plastic and elastic zones relax as a result of creep strain ahead of the crack tip. The relaxation is described by Riedel and Rice (83,84)

$$\sigma_E = \left[\frac{0.29K^2}{r E(N_C+1) B_C t} \right]^{[1/(N_C+1)]} f_E(\theta, N_C) \quad (A.4)$$

where: B_C and N_C are the material constants for Norton's law:

$$\dot{\epsilon}_C = B_C (\sigma)^{N_C} \quad (A.5)$$

where: $\dot{\epsilon}_C$ is the minimum creep rate

The RR stress calculation indicates that at time 0 the stress (σ_E) starts at infinity. This is obviously impossible and an upper bound on stress is the stress predicted for $t=0$ by HRR. A transition time can be calculated at

which the creep relaxed stress given by the RR calculation (Eq. A.9) is the same as the stress at r and $t=0$ given by HRR (Eq. A.2)

$$t_{\text{transition}} = \frac{0.29K^2}{B_c E (N_c + 1) r (\sigma_{t=0})^{(N_c + 1)}} \quad (\text{A.6})$$

This calculated transition time does not relate to the real test time, but it is only a starting time for subsequent creep strain accumulation.

A.3.2 The accumulation of creep strain

The creep strain ahead of the crack tip is calculated by integrating Norton's Law expression using the stress given by the RR analysis:

$$\epsilon_c(t) = \int_0^{t_f} \dot{\epsilon}_c dt = \int_0^{t_f} B_c (\sigma_{RR})^{N_c} dt \quad (\text{A.7})$$

where:

$\epsilon_c(t)$ = creep strain as a function of time

t_f = time interval to advance the crack

σ_{RR} = time dependent stress given by the RR singularity

The result of integrating Equation A.7 is

$$\epsilon_c(t) = \left[\left(\frac{0.29K^2}{E r} \right)^{N_c} B_c (N_c + 1) t \right]^{[1/(N_c + 1)]} \quad (\text{A.9})$$

Equation A.9 predicts the creep strain ahead of the crack, but for short time the accumulation of strain is very fast resulting from the infinite stresses predicted at $t=0$ by the RR singularity. The creep strain corresponding to the transition time is given by the following expression:

$$\epsilon_c(\text{transition}) = \frac{0.29K^2}{rE\sigma_{t=0}} \quad (\text{A.10})$$

It is interesting to note that this strain is independent of B_c and N_c . This transition strain is subtracted from the calculated creep strain to compensate for the over-prediction in stress at short time by the RR singularity. The time increment for crack advance by one element is given:

$$\Delta t = \left[\frac{\epsilon_i(t_{\text{trans}}) + \epsilon_{\text{crit}} - \epsilon_i}{\left[\left(\frac{0.29K^2}{Er} \right) B_c (N_c + 1) \right]^{(N_c + 1)}} \right] - t_{\text{transition}} \quad (\text{A.11})$$

where ϵ_{crit} is the critical strain for fracture and ϵ_i is the accumulated strain in that element from previous iterations. (note : $\epsilon_i = 0$ for the first jump). This is graphically illustrated in Figure 24.

The creep strain in an element ahead of the crack tip is calculated as:

$$\epsilon_c(\Delta t) = \left[\left[\frac{0.29K^2}{Er} \right]^{N_c} N_c (N_c + 1) (\Delta t + t_{\text{rans}}) \right]^{(1/(N_c + 1))} - \epsilon_c(t_{\text{rans}}) \quad (\text{A.12})$$

Creep strain were accumulated only for elements within the plastic zone. Elements outside the plastic zone are assumed to accumulate negligible creep strain as a result of the smaller stresses in the elastic region. However, at low values of K the creep in the elastic region may become significant. It should be noted that the plastic strain and primary creep strain are assumed to make a negligible contribution to the total amount of damage.

After each crack advance the stresses are reset to the calculated stresses at $t=0$ given by the HRR singularity for the new crack length. Once the stresses are reset the entire process begins again for the next jump in crack length.

A.3.3 Environmental considerations

The effect of environment in nickel-base alloys, has been experimentally documented by:

- loss of creep ductility
- change in fracture path

which results in faster creep crack growth rates in air than in inert environment. These experimental facts have been taken into account in the analysis. The critical creep strain required for crack advance was taken to be smaller in the air than the argon tests. The latter was given by the Monkman-Grant relationship (i.e. $\dot{\epsilon}_c t_{fr} = \epsilon_{crit}$). The critical creep strain in air is determined by fitting the predicted CCGR to the actual CCGR. Since the environmental damage changes the fracture path, the element size was equal to the grain size for air tests and equal to the prior powder size for the argon tests.

A.4 Discussion

The model was used to predict the CCGR for the four alloys studied. Figures 25 and 26 show the predicted crack growth behavior in air and in argon for low carbon Astroloy and Merl-76 respectively. The model predicts the experimental results within a factor of 2 for all the alloys. The predicted results show an initial transient corresponding to the stage I of the experimental creep crack growth curve. This results from the fact the crack tip is advancing through initially undamaged material for the first few jumps. Consequently a lower CCGR is observed upon loading which quickly (depending upon the initial K) rises to the stage II region. Many of the results reported in the literature reflect primarily this initial transient,

and any conclusions based on stage I CCGR data are questionable.

Thus the variation in the slope of the da/dt versus K curve is a result of the increasing number of elements accumulating creep damage as the plastic zone size increases with the crack advance. This process is taking place until a stage of dynamic equilibrium is established between the rate of crack advance and the rate of damage accumulation ahead of the crack tip. This determines approximately the onset of stage II of the creep crack growth curve.

The effect of grain size on CCGR was taken into account by changing the element size or crack step size. This caused changes in both the magnitude of CCGR for a given value of K and the slope of the da/dt versus K . The larger grain size resulted in higher slope and lower creep crack growth rate.

The effect of yield strength on CCGR can also be demonstrated by the proposed model. As the yield strength decreases the predicted CCGR also decreases as a result of lower stresses in the plastic zone and larger plastic zone size. This result has been observed, by industrial research groups. The process of reducing the yield strength of an alloy to decrease its creep crack growth susceptibility is referred to as "de-tuning" an alloy.

The model predicts the CCGR in air by using a smaller element size and a smaller critical strain for fracture than for the argon case. The reduction in the element size in air tests accounts for the observed change in fracture path from predominantly prior particular boundaries in argon to intergranular fracture in air. The decrease in fracture ductility in air is observed to vary from alloy to alloy. The critical strain for an inert environment is obtained from short time creep-rupture tests by multiplying the minimum creep

rate and the time to failure. The required change in ductility for each alloy is given in Table VI. The reduction in critical strain is a result of the embrittling effect of oxygen.

The ratio of the grain boundary concentration of boron to the grain boundary concentration of boron in Astroloy is also reported in Table 6. This expression shows the relative amount of B per unit of grain boundary volume. The weight percent B per unit grain boundary volume is proportional to the w/o B in the bulk times the average grain size divided by the grain boundary thickness (S). Boron content was found to give the best correlation with creep ductility. Figure 27 shows the ratio of creep ductility in air to that in argon used in the model versus the grain boundary concentration of Boron normalized by the grain boundary of Boron in low carbon Astroloy. The high Boron alloys have the best resistance to grain boundary embrittlement. Similar results were reported by Woodford when studying the effect of boron on oxygen embrittlement of IN-718 (85). The development of boron modified superalloys may increase the resistance to creep crack growth in the presence of oxygen.

Part B: Creep Crack growth in 2219-T851 Aluminum alloys

B.1 Experimental procedures

B.1.1 Material and heat treatment

The reported work was performed on a 2219 commercial aluminum alloy. The alloy was provided by "ALCOA" in the form of 1.27 cm thick rolled plates in the T851 temper (i.e., solution heat-treated, stress-relieved by stretching (1 1/2 to 3 percent permanent set), cold worked and artificially aged).

In order to gain some insight into the micromechanisms of intergranular creep cavity nucleation and of creep crack growth the experimental program was executed on 2219 heat treated to two different tempers (see Table VII)

Most of the tests were performed on 2219 in the T851 "as received" conditions (see Table VII). Tests were also performed in the T-mod (mod = modified) temper: T851/Solution Treated at 540°C for 2 hours/Water Quenched/Aged at 510°C for 2 hours/Water Quenched/Aged at 177°C for 18 hours.

B.1.2 Microstructural characterization

The handbook typical composition of this essentially aluminum-copper alloy (86) is given in Table VIII.

Samples of both tempers of 2219 aluminum alloy were mounted in thermosetting Bakelite (Buehler's Plastimet), ground on 120, 240, 320, 400 and 600 grit silicon carbide paper, polished with 6 mm diamond paste on nylon cloth, and polished with 1 μ m and 0.3 μ m alumina on felt cloths. The final polish was achieved with either 0.05 μ m alumina or a colloidal

silica solution on a fine felt cloth. It was found to be very important, in order to obtain good results, not to bypass any of the last polishing steps. In order to prevent particle pull-outs during polishing, it was necessary to apply only moderate pressure on the samples. No reproducible results could be obtained with electro-polishing techniques. In addition, excessive pitting associated with second phase particles was always encountered.

The polished metallographic samples were etched for 10 - 20 s with Keller's reagent (2 ml HF (48%), 3 ml HCl (concentrated), 5 ml HNO₃ (concentrated), 190 ml H₂O), washed in a stream of warm water and blown dry. The samples were then observed with an optical microscope (Zeiss Universal Microscope) or gold coated and observed with a Scanning Electron Microscope (AMR 1000A).

Optical and SEM micrographs of the microstructure of the rolling plane are presented in figures 28 and 29. In contrast to 2219 - T851 for which the grain boundary particles are barely discernable in the optical micrograph shown in figure 28, the grain boundary particles in 2219 - T mod are clearly visible for the same magnification. This difference in intergranular precipitate size is confirmed by the high magnification SEM micrographs of figures 29. There is no doubt that these precipitates are Al₂ Cu. The size and spacing distributions of these intergranular precipitates were measured by an approximate linear intercept method applied to the grain boundaries. Rather broad distributions independent of the plane of observation were determined. The mean values of the intergranular particle diameter and spacing distributions are given in Table II for both 2219 - T851 and 2219 - T mod.

The grain size in the rolling, short transverse and transverse and long transverse directions were also obtained by the linear intercept method. The results showed that no grain growth resulted from the T mod heat treatment. The average grain dimensions in the rolling, long and short transverse directions were determined to be respectively approximately:

$$50 \mu\text{m} \times 50 \mu\text{m} \times 25 \mu\text{m}.$$

Stringers of transgranular constituent particles can be seen aligned with the rolling direction on figure (28). According to Kaufman and Low (87), the large light grey particles are undissolved θ -Al₂ Cu, the large dark ones are Cu₂ Fe Al₇, and the smaller dark grey ones are Cu₃ Mn₂ Al₂₀. EDAX spectrum analysis did show evidence of Fe in large constituent particles, but no further phase identification was attempted. Finally, the background transgranular θ' - precipitates cannot be unambiguously resolved, even on the high magnification SEM micrographs (figure (29)).

B.1.3 Mechanical testing-specimen geometry

• Tensile testing

High temperature tensile tests were performed on a screw driven universal testing machine under constant crosshead displacement rate. An air circulation furnace was attached to the frame of the testing machine. The temperature was checked within $\pm 2^\circ\text{C}$ with a chromel-alumel thermocouple touching the specimen. Tensile tests were performed on cylindrical bars of gage length at least 2.54 cm and diameter 0.635 mm. Tests were run at 150, 175 and 200°C. Crosshead displacement rates of 5.08×10^{-5} m/min up to 5.08×10^{-3} m/min were selected.

- Creep testing

Creep tests were performed on dead-load lever-arm testing machines. The same type of furnace as for the tensile tests was used. The specimen geometry was identical as the one described in the previous section. In order to measure the creep strain rates, the specimen elongations were recorded with a DC-DC LVDT connected to the extensometer attached to the specimen gage length.

- Crack growth testing

Crack growth tests are performed on an Instron 1350 servo-hydraulic testing machine under the control of a DEC PDP 11/23. An Instron environmental chamber is clamped to the frame of the testing machine. Load on the specimen is applied through stainless steel pull rods extending into the chamber, to which steel grips for CT specimens are attached.

The temperature is checked within $\pm 2^{\circ}\text{C}$ with a Chromel-Alumel thermocouple touching the specimen. Prior to testing, the temperature is allowed to fully stabilize for about two hours.

Opening displacements are measured using an Instron clip gage dynamic extensometer attached, outside the furnace, to a long tubular steel extensometer spring-loaded against the knife edges on the specimen.

Prior to high temperature testing, the specimens are all fatigue-precracked at room temperature under computer control. They are then brought to high temperature and tested, also under computer control.

In this study, the results of two categories of crack growth tests are reported:

- (1) CREEP CRACK GROWTH tests, where the applied load cycle includes a hold time at maximum load;
- (2) FATIGUE CRACK GROWTH tests, where the applied load cycle does not include any hold time at maximum load.

The CT specimens were machined from the as - received or heat treated plates in the (T-L) and (L-T) orientations (see Figure 30). The dimensions of the specimens are given in Figure 31.

The starter notch length is:

$$a_0 = 0.8" = 2.03 \text{ cm}$$

.1" or .05" deep side grooves were machined on most of the specimens.

Two 0.050" thick steel knife edges attached on the front face of the specimens above and below the notch allowed measurements of opening displacements, at a normalized distance $.675"/2.5" = .27$ ahead of the loading line.

DCB specimens were also machined from the as received plates (in the T-851 temper) in the (T-L) and the (S-L) orientations (see figure 31). The dimensions of these specimens are given in Figure 32.

• Crack length measurement technique

Though the potential drop methods have been successfully used for nickel base superalloys and steels (88), the compliance method has been preferred in this study because of the expected lack of sensitivity of the electrical methods when applied to highly conductive alloys such as the aluminum alloys.

For CT specimens with no side grooves, a calibration of crack length versus compliance measured at the location of the knife edges has been obtained using the results reported in [89]. (See Appendix 2):

$$\frac{a}{w} = 1.025 - 6.07807 U + 47.1092 U^2 - 509.145 U^3 + 2417.19 U^4 - 4064.67 U^5 \quad (B-1)$$

where U is defined by:

$$U = 1/((bE' \frac{\Delta v}{\Delta P})^{1/2} + 1) \quad (B-2a)$$

with $E' = E$ under plane stress conditions (B-2b)

$$E' = \frac{E}{2(1 - \nu)} \text{ under plane strain conditions,} \quad (B-2c)$$

and where $bE' \frac{\Delta v}{\Delta P}$ is the normalized compliance as measured at the location of the knife edges.

An experimental calibration of crack length as a function of compliance was performed for specimens with 40% side grooves. In order to compile load-displacement data for different a/w values, either machined notches or fatigue cracks were introduced in 40% side-grooved CT specimens. In the latter case, the crack was propagated by fatigue between consecutive measurements of the compliance of the specimen, at R ratios alternatively equal to 0.5 surfaces from which crack lengths were easily deduced.

The following least-square fit was obtained:

$$\frac{a}{w} = .943769 - 4.29331 U + 38.0499 U^2 - 698.674 U^3 + 4721.32 U^4 - 10886.8 U^5 \quad (B-3)$$

where U is defined as:

$$U = 1/((bE \frac{\Delta v}{\Delta P})^{1/2} + 1) \quad (B-4)$$

Large discrepancies were found between the compliance calibrations for specimens with 40% side grooves and for smooth specimens under both plane stress and plane strain conditions.

Replacing the thickness b by an empirical effective thickness defined by:

$$b_{eff} = b - (b - b_{net})^2/b \quad (B-5)$$

in (B-2a) has been reported to take up to 50% side grooves into account [90]. A relatively good agreement was found between our experimental calibration (equations (B-3) and (B-4)) and this empirical one (equations (B-1) and (B-2) modified by (B-5)), under plane strain conditions for a/w ratios up to about 0.6, and under plane stress conditions for larger a/w values (figure 33).

In our study, crack lengths were calculated from compliance measurements at the location of the knife edges by using:

- (1) the experimental calibration (B-3) for specimens with 40% side grooves;
- (2) the calibration (B-1) under plane stress conditions for smooth specimens;
- (3) the calibration (B-1) under plane strain conditions for specimens with 20% side grooves.

The validity of these choices was checked by directly measuring the actual initial and final crack lengths on the fracture surfaces of broken specimens.

Stress intensity factor calculation

The stress intensity factor K as a function of crack length to width ratio a/w was calculated for standard smooth CT specimens according to the classical equation [91]:

$$K = \frac{P}{b \sqrt{w}} \frac{(2 + a/w)}{(1 - a/w)^{3/2}} f(a/w)$$

with $f(a/w) = .886 + 4.64 \frac{a}{w} - 13.32 \left(\frac{a}{w}\right)^2 + 14.72 \left(\frac{a}{w}\right)^3 - 5.6 \left(\frac{a}{w}\right)^4$

For CT specimens with side grooves, the following well-accepted formula was used [92,94] (See Appendix 1):

$$K = \frac{P}{\sqrt{bb_{net}} w} \frac{(2 + a/w)}{(1 - a/w)^{3/2}} f(a/w) \quad (B-7)$$

where $f(a/w)$ has already been defined.

An experimental verification of this K -calculation for 40% side grooved specimens was performed. By assuming that the location of the axis of rotation of the arms of the specimen was not largely affected by the presence of side grooves, the loading line compliance for specimens with 40% side grooves was estimated, from which an experimental stress intensity factor was calculated (see Appendix 3):

$$K_{exp} = \frac{P}{\sqrt{bb_{net}} w} \frac{(2 + a/w)}{(1 - a/w)^{3/2}} (.374907 + 6.52948 \frac{a}{w} - 10.5935 \left(\frac{a}{w}\right)^2$$

$$+ .703939 \left(\frac{a}{w}\right)^3 + 6.28039 \left(\frac{a}{w}\right)^4) \quad (B-8)$$

The stress intensity factors given by (B-7) and (B-8) differ by less than 10% for a/w up to .65. Since the applicability of the concepts of the Linear Elastic Fracture Mechanics is questionable for longer crack lengths, and since it was not possible to check the eventual non-correlation between the location of the axis of rotation of the arms of the specimen and the side grooves, the expression (B-7) was used with confidence in this study.

B.2 Experimental results

B.2.1 Mechanical properties-constitutive equations

All the tensile tests were run in the (T) direction (i.e., the tensile specimen were machined parallel to the long-transverse direction) Young's modulus, the 0.2% yield stress, the UTS and the total elongation at fracture are shown in Table X. The constants of the uniaxial plastic constitutive law ($\epsilon^{(pl)} = B_p \sigma^{n_p}$) are also given. The constants n_p and B_p were obtained by least square fits on all the data corresponding to given test conditions. In agreement with the room temperature hardness of 2219-T851 and of 2219-Tmod, the T851 temper has a higher strength than the Tmod temper. This can be explained by the coarser precipitates in the Tmod temper.

Steady state secondary creep strain rates were measured over 4 orders of magnitude ranging from $1 \times 10^{-8} \text{ s}^{-1}$ to $1 \times 10^{-14} \text{ s}^{-1}$. 2219-Tmod was found to creep 2 to 3 orders of magnitude faster than 2219-T851. The constants n_c and B_c of the power laws creep uniaxial constitutive law $\dot{\epsilon}_{(cr)} = B_c \sigma^{n_c}$

were determined by least square fits through the experimental data, and are given in Table XI. The constants of the Monkman-Grant relationship ($\dot{\epsilon}_s t_f = C_{MG}$) are the creep ductilities are given for both alloys in Table XII.

B.2.2 Creep crack growth test results

The results of creep crack growth tests performed under load control on CT specimens and under opening displacement control on DCB specimens are presented in this section. The experimental programs given in Tables XIII, XIV were designed: 1) to study the applicability of fracture mechanics concepts to creep crack growth in creep brittle materials and 2) to identify the micromechanism of creep crack growth in 2219-T851 and 2219-Tmod.

- Creep crack growth test results in (T specimen)

- a) Effect of Hold Time and Cyclic frequency

For automated creep crack growth tests performed in 2219-T851 in the (T-L) orientation in air with hold time 10, 30, 100, 300 and 1000 seconds, 10 seconds loading and unloading, $R=0.5$ and $P_{max}=5344N$, the crack growth rates per cycle (da/dN) for a given maximum stress intensity factor were found to increase with increasing hold times (Figure 34). This shows that, as expected, time dependent damage is encountered in addition to cyclic damage during such tests.

For fatigue crack growth tests with a triangular wave shape with $R=0.05$, crack growth rates per cycle (da/dN) at a given maximum stress intensity factor are independent of frequency in the range 0.02 HZ - 3HZ (see figure 35). For a frequency of 0.02Hz, the crack growth rates per cycle for given maximum stress intensity factors were found to be lower for a triangular load wave than for a trapezoidal load wave, which demonstrates the highly damaging effect of a held time of maximum load.

Only the hold time at maximum load and the loading and unloading were taken into account in estimating the cycle frequency because there was no crack growth observed during the short hold time (5 sec) elapsed at minimum load. The crack growth rates per cycle for tests with hold times can be written for a given maximum stress intensity factor as:

$$\frac{da}{dN} = \frac{1}{\text{Frequency}} \frac{da}{dt} \quad (B-9)$$

where $\frac{da}{dt}$ (= crack growth rates per unit time) are found to be independent of the cycle hold time. Thus all the crack growth data presented in Figure 34 fall in a narrow scatter band on a da/dt versus K_{max} plot where da/dt is calculated as explained above. (Figure 36)

b) Effect of R ratio

As can be seen in Figure 37, a decrease of the R ratios from 0.5 down to 0.05 does not affect the crack growth rates in 2219-T851 in the (T-L) orientation. The maximum stress intensity factor K_{max} and not the stress intensity factor range (ΔK) provides thus the driving force for crack growth.

The creep crack growth rates per unit time for a creep crack growth test with 300s hold time, and $R=0.05$ are compared in figure 38 to crack growth rates measured during experiments with no unloadings ($R=1.0$) performed in 2219-T851. In the latter tests, crack lengths were obtained from averaged opening displacement data and the knowledge of the length of the initial fatigue precrack and the corresponding specimen compliance. The crack growth rates per unit time are the same for both tests except at low crack growth rates where the apparent crack velocities are higher for the

tests with no unloadings. This can be explained by the fact that any increase of the opening displacement during a tests is due both to creep deformation and crack advance, the creep component being negligible only at high crack growth rates. The low crack growth rates will thus be overestimated by the opening displacement measurements during tests with no unloadings.

c) Effect of the initial stress intensity factor

The crack growth curves da/dt versus K_{max} of 2219-T851 also exhibit the stage II behavior, Figure 39. The transient stage I regime of crack growth is function of the initial stress intensity factor, and is not a threshold for crack growth.

d) Constant- K_{max} tests

In constant maximum stress intensity factor tests performed as CT specimen, the maximum load was adjusted at each cycle. In such tests, K_{max} could be maintained within $\pm 0.5\%$ of the target K for crack length to width ratios from 0.35 to 0.65. The crack growth rates for this whole range of crack lengths fall right in the scatter band of the results of the constant maximum load tests in the stage II regime (see figure 40).

These results suggest that for simple K histories such as those followed during constant maximum load or constant maximum stress intensity factor tests there exists a correlation between da/dt versus K_{max} in the quasi-steady or steady state crack growth regime wide plane strain condition.

e) Effect of microstructure

The creep crack growth rates for constant maximum load tests performed at 175°C in air on 2219-T851 and 2219-Tmod ni the (T-L) orientation

are showing in figure 41. The creep crack growth rates in 2219-T851 are found to be about one order of magnitude higher than those in 2219-Tmod. Although 2219-Tmod creeps at faster rates than 2219-T851, the lower yield stress and the higher creep ductility of the former alloy can explain this difference in creep crack growth rates.

- Creep Crack Growth Test Results in DCB Specimens

Constant opening displacement creep crack growth tests were performed in air and in vacuum in 2219-T851 at 175°C in the (T-L) and the (S-L) orientation in DCB specimen. The results of these tests are compiled in Table XV. As can be seen on this Table, the creep crack growth rates under such decreasing-K conditions are found to be independent of the specimen orientation. More importantly, the creep crack growth rates in 2219-T851 are independent of the test environment since crack growth increments for given initial conditions are comparable in air and in vacuum. Creep crack growth in 2219-T851, and undoubtedly also in 2219-Tmod, is thus controlled by creep damage and not by environment induced damage. The average creep crack growth rates listed in Table XV are very low compared to extrapolations of the stage II creep crack growth rates measured in CT specimens. These conclusions do not take into account the creep stress relaxation in the DCB specimens under constant opening displacement.

B.2.3 Fractography

The SEM fractographs of Figures (42) through (44) show evidence of both intergranular and transgranular fracture processes. The relative importance of these fracture modes was found to be a function of the heat treatment, of the crack growth rate, and eventually the specimen geometry.

The data listed in Table XVI show that the amount of intergranular fracture area decreases as da/dt increases.

The schematic of figure 45 explains the elongated shape of the grains on fracture surfaces of (T-L) specimens. As can be seen on the high magnification fractographs of grain facets of 2219-T851 and 2219-Tmod shown in Figure (46) and (47) respectively, the intergranular damage develops as creep cavitation. The non-equilibrium crack-like shape of the cavities visible in the grain boundaries normal to the plane of the fractographs, their large size and the very high triaxial tensile stresses at the crack tip of a creep brittle material suggest a cavity growth process. The ridges on the grain facets in the plane of the fractographs shown in figure (46) and (47) can be identified as the remains of ligaments between cavities about to coalesce in grain boundaries perpendicular to the plane of fracture.

B.3 Discussion

Both the applicability of fracture mechanics concepts to creep crack growth in 2219 aluminum alloy and the micromechanisms of creep crack growth are discussed in this section.

a) Applicability of Fracture Mechanics to Creep Crack Growth

For constant maximum load tests and constant maximum stress intensity factor tests, a correlation between da/dt and K_{max} was reported for a steady state or quasi-steady state regime of creep crack growth under constrained conditions. This correlation was found to be independent of the initial conditions. Whether other loading parameters could also provide a correlation is discussed now.

The net section stress, the nominal stress, the reference stress and

the C^* -integral were also estimated for constant load tests and constant stress intensity factor tests in 2219-T851 at 175°C. The equations which were used to calculate these loading parameters and the stress intensity factor are listed in Table XVII along with references where they were originally given. The creep crack growth rates for constant load tests fall on totally separate separate curves when they are plotted versus the net section stress (see figure 48). That the net section stress does not correlate with the creep crack growth rates in CT specimens is not surprising since the bending stresses at the crack tip are dominant as can be verified from the equation giving the nominal stress. Both the nominal stress and the reference stress are found to correlate satisfactorily with the creep crack growth rates in the stage II regime of crack growth for constant P_{max} tests independently of the initial conditions (Figure 49 and 50). The only significant difference between figure (49) and figure (50) lies in the ranges of values of the nominal and the reference stress. Exponents close to 4 are found for da/dt -correlations with both the nominal stress and the reference stress. The similitude between the da/dt correlations with the nominal stress, and reference stress and the stress intensity factor can be explained by the fact that the variations of both stress parameters are dominated by the variations of $[(1+a/w)/(1-a/w)^2]$ while those of the stress intensity factor are dominated by the similar variations of $[(2+a/w)/(1-a/w)^{3/2}]$. The C^* -integral appears to correlate also with the stage II creep crack growth rates for constant P_{max} tests. The stress intensity factor, the C^* -integral, the nominal stress and the reference stress all seem to correlate with the stage II creep crack growth rates for constant load tests. It is thus very difficult to determine unambiguously

the appropriate loading parameter to correlate with the creep crack growth rates from constant P_{\max} tests results only.

Although the creep crack growth rates were found to remain essentially constant during constant stress intensity factor tests the nominal stress, the reference stress and the C^* -integral were shown to increase steadily with crack length during the same tests (see figures (51), (52), and (53)). In spite of the results of the constant of the constant load tests, neither the nominal stress, one reference stress nor the C^* -integral can then correlated with the stage II creep crack growth rates in 2219-T851 aluminum alloy. It is only with the stress intensity factor that such a correlation can be attained. In order to determine a correlating load-parameter for creep crack growth, it is thus essential that tests where the creep crack growth rates can be maintained constant be performed.

b) Micromechanisms of creep crack growth in 2219-T851 aluminum alloy

The creep damage accumulates under the form of intergranular creep cavities in 2219 aluminum alloy. It is likely that intergranular creep cavities grow in the near tip stresses until a critical stage where separated grain boundaries link and join the main crack by localized ductile shear. Such a mechanism is schematically shown on figure (54). According to this suggested mechanism, the transgranular fracture does not proceed by time dependent creep processes, but by time-independent plastic processes instead. As the applied stress intensity factor is increased, the critical density of separated grain boundaries for crack advance by ductile shear is expected to decrease. The creep crack growth mechanism shown in figure (54) is thus in agreement with the observed increase of

the transgranular fracture area fraction with the stress intensity factor and the creep crack growth rates.

c) Creep Crack growth Prediction

The creep crack growth model, presented in section A, based on creep strain accumulation in the plastic zone ahead of the crack tip proposed by Bain (33) was found to provide a good fit to the experimental data for 2219-T851 and 2219-Tmod if the creep ductilities of these alloys were assumed to be 0.06 and 0.2 respectively (see figure (55)). These values are not very different from those determined experimentally (see Table XVIII).

III. Conclusions

1) The creep crack growth behavior of two different alloy systems was investigated. Four Nickel-base Superalloys and two heat treatments of aluminum alloy 2219 were tested. The Nickel-base superalloys which were HIP/PM products, with different powder particle size and various boron and zirconium contents exhibited strong environmental effect. Both treatments of the 2219 aluminum alloy were insensitive to environment. The single edge notch (SEN) specimen geometry was used for the testing of the Ni-base superalloys. Compact tension and DCB specimens were used for testing the 2219 aluminum alloys. The validity of the application of LEFM concepts was verified.

2) Creep crack growth rates were measured for the four Ni-base superalloys at 704°C in both air and in a 99.999% pure argon environment. The alloys tested were low carbon Astroloy, Merl-76, low carbon IN-100 and Rene 95. The creep crack growth ranged from 10^{-9} m/s to 10^{-4} m/s, and the stress intensity factor ranged from $10\text{MPa}\sqrt{\text{m}}$ to $120\text{MPa}\sqrt{\text{m}}$. The presence of oxygen during CCG resulted in an increase in the measured CCGR over the CCGR in pure argon for a given K in all the alloys tested. The increase in CCGR varies for the alloys tested, with Rene 95 (60 mesh) having the largest increase and low carbon IN-100 having the smallest increase in CCGR due to oxygen.

3) The creep crack growth rates were measured in 2219-T851 at 150, 175 and 200°C and in the Tmod at 175°C. The creep crack growth rates were measured in the 1×10^{-8} - 3×10^{-6} m/s range for applied maximum stress intensity factors varying from 16 to 32 $\text{MPa}\sqrt{\text{m}}$. Creep crack growth tests performed in 2219-T851 at 175°C in air and in vacuum on DCB specimens under

constant opening displacement showed that the crack growth process in 2219 is not controlled by environment induced damage.

4) The creep crack growth curves da/dt versus K were found to show three stages. Stage I corresponds to an initial transient, where da/dt varies very rapidly with K and depends on the initial loading conditions. Stage II corresponds to a quasi-steady regime of crack growth. Stage III corresponds to fast fracture.

5) A unique correlation was shown to exist between the stress intensity factor and the stage II creep crack growth rates in both alloy systems.

6) The environmental effect in the Ni-base Superalloys was due to the embrittlement of the grain boundaries due by oxygen diffusion. The increase in the measured CCGR in air resulted from a change in fracture path and a decrease in creep ductility.

7) The grain boundary chemistry of the Ni-base Superalloys is critical in determining its susceptibility to oxygen embrittlement. Alloys with high concentrations of boron tend to have a smaller reduction in creep ductility and lower increase in CCGR in air than alloys with low Boron content.

8) A computer model was developed to predict the CCG behavior of the alloys. The model is based on the accumulation of damage in the form creep strain ahead of the crack tip. The results of the model were in very good agreement with actual CCGR results, and the model provided some insights in the CCG process. The model predicts that grain size, critical strain, and creep rate will all significantly affect the CCGR. The model also predicts that load history effects will significantly alter the CCGR measured.

IV. Recommendations for additional research

The following research problems should be considered:

1) The reproducibility of creep crack growth tests should be assessed. A careful error analysis should be performed in order to quantify precisely the sources of data scatter within one data set and from test to test.

2) The effect of stress triaxiality on creep crack growth (e.g., crack front tunnelling) should be studied both experimentally and theoretically.

3) The crack nucleation stage and the propagation stage of "short" cracks under creep conditions should be considered.

4) A study of transient regimes of crack growth should be undertaken by running tests under programmed load. The effects of load sequence and of previous history should be considered.

5) Decreasing-K tests should be performed in order to determine whether there is a threshold for non-propagating creep cracks.

6) The relative importance of creep damage and of environment induced damage, and, more particularly, of oxidation, should be quantified for each alloy of interest. The optimization of the microstructure of these alloys to increase their resistance to creep cavitation and/or oxidation in order to improve their resistance to creep crack growth should be considered.

7) In all cases, the validity of extrapolation of test data to engineering applications should be carefully studied.

PERSONNEL

Principal Investigator

R. M. Pelloux
Professor
Massachusetts Institute of Technology
Department of Materials Science and Engineering
Cambridge, MA 02139

Research Assistants

K. R. Bain, currently with Allison Gas Turbine Operations Division
of General Motors, Indianapolis, IN 46206

P. L. Bensussan, currently Ingenieur de l'Armement, ETCA, 94114
Arcueil Cedex, France.

J. W. Prybylowski, Materials Science and Engineering Department,
Massachusetts Institute of Technology, Cambridge, MA 02139.

Ioannis P. Vasatis, Materials Science and Engineering Department,
Massachusetts Institute of Technology, Cambridge, MA 02139.

TECHNICAL PUBLICATIONS

1. R. M. Pelloux, "Fractography", in Atomistics of Fracture, ed. R.M. Latanision and J. R. Pickens, Plenum Pub. Corp., 1983, p.241-251.
2. P. L. Bensussan, D. A. Jablonski, R. M. Pelloux, "A Study of Creep Crack Growth in 2219-T851 Aluminum Alloy Using a Computerized Testing System", Met. Trans. A, V.15A, Jan. 1984, p. 107-120.
3. K. R. Bain, R. M. Pelloux, "Effect of Environment on Creep Crack Growth in PM/HIP Rene-95", Met. Trans, Vol. 15A, Feb. 1984, p.381.
4. J. Prybylowski, R. M. Pelloux, and Peter Price, "The Effects of Argon Contamination in a PM/HIP Nickel Base Superalloy", Powder Metallurgy, 1 Carlton House Terrace, London, SW1Y SDB, England, August 1983 (in print)
5. P. L. Bensussan and R. M. Pelloux, "Creep Crack Growth in 2219-T851 Aluminum Alloy: Application of Fracture Mechanics Concepts", submitted to Int. Congress on Fracture, Prof. Raj N. Dubey, University of Waterloo, Ont. Canada N2L3G1, January 1984.
6. K. R. Bain and R. M. Pelloux, "Effect of Oxygen on Creep Crack Growth in PM/HIP Nickel base Superalloys", submitted and accepted by Metall. Soc. of AIME, Warrendale, PA. 15086, February 1984.
7. J. S. Huang and R. M. Pelloux, "Application of High Temperature Fracture Mechanics to the Prediction of Creep Crack Growth Role for a High Strength Nickel base Superalloy", ASTM STP. 833.
8. R. M. Pelloux, "Fracture Prevention in the Aeronautical and Space Industries (Keynote Lecture), Int. Conf. on Fracture Prevention in Energy and Transport Systems, Rio de Janeiro, December 1983.
9. K. R. Bain, I. P. Vasatis, R. M. Pelloux, "Prediction of Creep Crack Growth Rate in PM/HIP Nickel Base Superalloys", to be submitted to Journal of Materials Science and Engineering, 1984.

REFERENCES

- [1] K. Sadananda, P. Shahinian: Creep Crack Growth Behavior and Theoretical Modelling, Met. Sci. J., 15, 1981, p. 425-432.
- [2] L.S. Fu: Creep Crack Growth in Technical Alloys at Elevated Temperature--A Review, Eng. Fract. Mech., 13, 1980, p. 307-330.
- [3] M.H. El Haddad, T.H. Topper, B. Mukherjee: Review of New Developments in Crack Propagation Studies, JTEVA, 9, 1981, p. 65-81.
- [4] K. Sadananda, P. Shahinian, Crack Growth Under Creep and Fatigue Conditions, in Creep-Fatigue - Environment Interactions, Eds. R.M. Pelloux and N.S. Stoloff, AIME, 1980, p. 86-111.
- [5] R.M. Pelloux, J.S. Huang: Creep-Fatigue-Environment Interactions in Astroloy, Ibid, p. 151-164.
- [6] J.L. Bassani: Macro and Micro-Mechanical Aspects of Creep Fracture, in Advances in Aerospace Structures and Materials - I, Eds. S.S. Wang and W.J. Renton, ASME, 1981.
- [7] J.L. Bassani: Creep Crack Extension by Grain-Boundary Cavitation, in Creep and Fracture of Engineering materials and Structures, Eds. B. Wilshire and D.R. Owen, 1981, p. 329-344.
- [8] J.L. Bassani, V. Vitek: Propagation of Cracks Under Creep Conditions, to appear in the Proceedings of the 9th U.S. National Congress of Applied Mechanics, Eds. L.B. Freund and C.F. Shir.
- [9] W.D. Nix, D.K. Matlock, R.J. Dimelfi: A Model for Creep Fracture Based on the Plastic Growth of Cavities at the Tips of Grain Boundary Wedge Cracks, Acta Met, 25, 1977, p. 495 - 503.
- [10] R.J. Dimelfi, W.D. Nix: The Stress Dependence of the Crack Growth Rate During Creep, Int. J. of Fract., 13, 1977, p. 341-348.
- [11] R. Raj, S. Baik: Creep Crack Propagation by Cavitation Near Crack Tips, Met. Sci. J., 14, 1980, p.383.
- [12] V. Vitek, T. Takasugi: Mechanisms of Creep Crack Growth, in Micro and Macro Mechanisms of Crack Growth, Eds. K. Sadananda, B.B. Rath and D.J. Michel, AIME, 1982, p. 107-118.
- [13] K. Sadananda, P. Shahinian: High Temperature Time-Dependent Crack Growth, Ibid, p. 119-130.
- [14] J.S. Huang: Fatigue Crack Growth and Creep Crack Growth of P/M HIP Low Carbon Astroloy at High Temperatures, Sc. D. Thesis, MIT, February, 1981.

- [15] K.M. Niklbin and B.A. Webster, Micro and Macro Mechanisms of Crack Growth, edited by K. Sadananda, BB. Ruth and D.J. Mickel, AIME, 1982, p. 137.
- [16] D.J. Smith and G.A. Webster, "Influence of Cyclic Loading on Crack Growth of .5% Cr, .5% Mo, .25% V steel", to be presented at the Fourth International Conf. on Behavior of Materials, Stockholm, August. 1983.
- [17] K. Sadananda and P. Shahinian, Met. Trans, A., 8A, 1977, p. 439.
- [18] K. Sadananda and P. Shahinian, Met. Trans, A., 9A, 1978, p. 79.
- [19] R.C. Donath, J. Nicholas and C.S. Fu, Fracture Mechanics: Thirteenth Conference, ASTM STP 743, edited by R. Roberts, p. 186.
- [20] L.S. Fu, Eng. Fract. Mech., vol 13, 1980, p. 307.
- [21] H.P. Van Leeuwen, Eng. Fract. Mechanics, vol. 9, 1977, p. 951.
- [22] P.L. Bensussan, D.A. Jablonski and R.M. Pelloux: Metall. Trans. A., 1984, vol. 15A, pp. 107-120.
- [23] G.J. Neate: Mater. Sci. Eng., 1978, vol. 33, pp. 165-173.
- [24] J.G. Kaufman, K.O. Bogardus, D.A. Mauney and R.C. Malcom: in Mechanics of Crack Growth, AST, STP 590, J.R. Rice and P.C. Paris, eds., American Society for Testing and Materials, Philadelphia, PA, 1976, pp. 149-168.
- [25] J.L. Kenyon, G.A. Webster, J.C. Radon and C.E. Turner: in Proceedings of the International Conference on Creep and Fatigue at Elevated Temperature Applications, I. Mech. E. Conf. Publ., vol. 13, Edmunds, England, 1973, Paper No. C156/73.
- [26] G.J. Neate and M.J. Siverns: in Proceedings of the International Conference on Creep and Fatigue at Elevated Temperature Applications, I Mech, E. Conf. Publ., vol. 13, Edmunds, England, 1973, Paper No. C234/73.
- [27] S. Taira and R. Ohtani: in Proceedings of the International Conference on Creep and Fatigue at Elevated Temperature Applications, I. Mech. E. Conf. Publ., vol 13, Edmunds, England, 1973, Paper No. C213/73.
- [28] D.J. Gooch: Mater. Sci. Eng., 1977, vol. 29, pp. 227-240.
- [29] K. Ohji, K. Ogura, S. Kubo and Y. Katada: in Proceedings of the International Conference on Engineering Aspects of Creep, I. Mech. E. Conf. Publ., vol. 2, Edmunds, England, 1980, Paper No. C240/80.

- [30] K.M. Nibkin, D.J. Smith and G.A. Webster: to be published in Advances in Life Prediction Methods at Elevated Temperatures, ASME, New York, N.Y., 1984.
- [31] S. Taira and R. Ohtani: in Proceedings of the Second International Conference on Mechanical Behavior of Materials, American Society for Metals, Metals Park, OH, 1978, pp. 155-182.
- [32] E.M. Christian, D.J. Smith, G.A. Webster and E.G. Ellison: in Advances in Fracture Research, D. Francois, ed., vol. 3, Pergamon Press, Oxford, England, 1981, pp. 1295-1302.
- [33] K. Bain: Effect of Oxygen on Creep Crack Growth in Nickel-Base-Superalloys, Ph.D. Thesis, Dept. of Materials Science and Engineering, Massachusetts Institute of Technology, Cambridge, MA, September 1983.
- [34] S. Floreen: Metall. Trans. A, 1975, vol. 6A, pp. 1741-1749.
- [35] I. Vasatis and R.M. Pelloux: Massachusetts Institute of Technology, Cambridge, MA, unpublished research, 1983.
- [36] J. Prybylowski and R.M. Pelloux: Massachusetts Institute of Technology, Cambridge, MA, unpublished research, 1983.
- [37] R. Koterazawa and T. Mori: J. Eng. Mater. Technol., Trans. ASME, 1977, vol. 99, pp. 298-305.
- [38] S. Taira, R. Ohtani and T. Kitamura: J. Eng. Mater. Technol., Trans. ASME, 1979, vol. 101, pp. 154-161.
- [39] E. Maas and A. Pineau: to be published in the Proceedings of the Fourth International Conference on the Mechanical Behavior of Materials (ICM4), Stockholm, Sweden, August 1983.
- [40] K. Sadananda and P. Shahinian: in Cavities and Cracks in Creep and Fatigue, J. Gittus, ed., Applied Science Publishers, London, England, 1982, pp. 109-195.
- [41] K. Sadananda and P. Shahinian: Metall. Trans. A, 1983. vol. 14A, pp. 1467-1480.
- [42] G.A. Webster: in Mechanics and Physics of Fracture, F.J. Bradshaw, ed., The Institute of Physics and the Metals Society, Cambridge, England, 1975, Paper No. 18.
- [43] K.M. Nibkin, G.A. Webster and C.E. Turner: in Cracks and Fracture, ASTM STP 601, J.L. Swedlow and M.L. Williams, eds., American Society for Testing and Materials, Philadelphia, PA, 1976, pp. 47-62.
- [44] J.M. Larson and S. Floreen: Metall. Trans. A, 1977, vol. 8A, pp. 51-55.

- [45] K. Bain: Creep Crack Growth Rates of Rene 95 in Air and Pure Argon, S.M. Thesis, Dept. of Materials Science and Engineering, Massachusetts Institute of Technology, Cambridge, MA, February 1982.
- [46] S. Floreen: in Creep-Fatigue - Environment Interactions, R.M. Pelloux and N.S. Stoloff, eds., AIME, New York, NY, 1980., pp. 112-128.
- [47] R.M. Pelloux and J.S. Huang: in Creep-Fatigue-Environment Interactions, R.M. Pelloux and N.S. Stoloff, eds., AIME, New York, NY, 1980, pp. 151-164.
- [48] K. Sadananda and P. Shahinian: Mater. Sci. Eng., 1980, vol. 43, pp. 159-168.
- [49] A.E. Gemma: Eng. Fract. Mech., 1979, vol. 11, pp. 763-774.
- [50] B. Wu and R.M. Pelloux: Massachusetts Institute of Technology, Cambridge, MA, unpublished research, 1981.
- [51] C.C. Law and M.J. Blackburn: Metall. Trans. A, 1980, vol. 11A, pp. 495-507.
- [52] J. Prybylowski: The Effects of Argon Contamination in Hot Isostatically Pressed Merl 76 Powder Billets, S.M. Thesis, Dept. of Materials Science and Engineering, Massachusetts Institute of Technology, Cambridge, MA, February 1981.
- [53] F. Gabrielli and R.M. Pelloux: Metall. Trans. A, 1982, vol. 13A pp. 1083-1090.
- [54] R.B. Scarlin: Mater. Sci. Eng., 1977, vol. 30, pp. 55-64.
- [55] D.J. Gooch, JR. Haigh and B.L. King: Met. Sci. J., 1977, vol. II, pp. 545-550.
- [56] S. Floreen: in Micro and Macro Mechanics of Crack Growth, K. Sadananda, B.B. Rath and D.J. Michel, eds., AIME, New York, NY, 1982, pp. 177-184.
- [57] C.M. Branco and J.C. Radon: in Proceedings of the International Conference on Engineering Aspects of Creep, I. Mech. E. Conf. Publ., vol. 2, Edmunds, England, 1980, Paper no. C210/80, pp. 43-48.
- [58] A. Pineau, "Subcritical Crack Growth Due to Fatigue, Stress Corrosion and Creep", ISPRA, 1981.
- [59] S. Floreen and J.M. Davidson, Met. Trans. A., 14A. 1983, p.895.
- [60] K.R. Bain and R.M. Pelloux, "Effect of Environment on Creep Crack Growth in Rene-95", Metall. Trans. A, 1984, Vol. 15A, p. 381.
- [63] R.H. Bricknell and D.A. Woodford, Met. Trans. A., 12A, 1981, p. 425.

- [64] J. Reuchet and L. Remy, Met. Trans. A, 14A, 1983, p. 141.
- [65] M. Prager and G. Sines, Journal of Basic Eng., 1971, p. 225.
- [66] D.A. Woodford and R.H. Bricknell, Met. Trans. A, 12A, 1981, p. 1467.
- [67] P.M. Chaka and C.J. McMahon, Jr., Met. Trans. A., vol 5., 1974, p. 441.
- [68] D.A. Woodford, Met. Trans. A, 12A, 1981, p. 299.
- [69] R.H. Bricknell, R.A. Mulford, and D.A. Woodford, Met. Trans. A, 13A, 1982, p. 1223.
- [70] R.A. Mulford, Met. Trans. A, 14A, 1983, p. 865.
- [71] K. Sadananda and P. Shahinian: Eng. Fract. Mech., 1981, vol. 15, pp. 327-342.
- [72] K.M. Nibkin, G.A. Webster and C.E. Turner: in Fracture 1977 - Advances in Research on the Strength and Fracture of Materials, D.M.R. Taplin, ed., vol. 2, University of Waterloo Press, Waterloo, Canada, 1977, pp. 627-634.
- [73] V.M. Radhakrishnan and A.J. McEvily: J. Eng. Mater. Technol., Trans. ASME, 1980, vol. 102, pp. 200-206.
- [74] O.H. Kriege and J.M. Baris, Trans. ASM 62, p. 195, 1969.
- [75] R.O. Ritchie, "Crack Growth Monitoring: Some Considerations on the Electrical Potential Method", University of Cambridge, 1972.
- [76] M.D. Halliday and C.J. Beevers, The Measurement of Crack Length and Shape during Fracture and Fatigue, 1980, p. 85.
- [77] H.H. Johnson, Materials Research and Standards, Vol. 5, 1965, p. 442.
- [78] W.F. Brown and J.E. Strawly, Plane Strain Crack Toughness Testing of High Strength Metallic Materials, ASTM ST0 410, Philadelphia, 1966.
- [79] C.F. Shih, H.F. DeLorenzi, Int. Journ. of Materials, 1, 1966, p. 770.
- [80] D. Broek, Elementary Engineering Fracture Mechanics, Sijthoff and Noordoff ed., 1978.
- [81] J.R. Rice and G.F. Rosengren: J. Mech. Phys. Solids, 1968, vol. 16, pp. 1-12.
- [82] J.W. Hutchinson: J. Mech. Phys. Solids, 1968, vol. 16, pp. 13-31.
- [83] H. Riedel and J.R. Rice: in Fracture Mechanics: Twelfth Conference, ASTM STP 700, P.C. Paris, ed., American Society for Testing and Materials. Philadelphia, PA, 1980, pp. 112-130.

- [84] J.D. Landes and J.A. Begley: in Mechanics of Crack Growth, ASTM STP 590. J.R. Rice and P.C. Paris, eds., American Society for Testing and Materials, Philadelphia, PA, 1976, pp. 128-148.
- [85] D.A. Woodford, Met. Trans. A, 12A; 1981, p. 229.
- [86] ASM Metals Handbook, 9th ed., vol. 2, ASM, Metals Park, OH, 1979.
- [87] J.G. Kaufman and J.R. Low: in Proceedings of the Second International Conference on Mechanical Behavior of Materials, Special Volume, American Society for Metals, Metals Park, OH, 1978, pp. 415-471.
- [88] E. Hornbogen: Aluminium, 1967, vol. 43, pp. 166-170.
- [89] A. Saxena and S.J. Hudak: Int. J. Fracture, 1978, vol. 14, pp. 453-468.
- [90] C. F. Chih and H.G. deLorenzi: Int. J. Fracture, 1977, vol. 13, pp. 544-548.
- [91] ASTM E399-81, Annual Book of ASTM Standards, Part 10, ASTM, Philadelphia, PA, 1982, p. 611.
- [92] C.N. Freed and J.M. Krafft: J. Mater., 1966, vol. 1, pp. 770-790.
- [93] P. LeFort and D. F. Mowbray: J. Test. Eval., Trans. ASME, 1978, vol. 6, pp. 119.
- [94] V.M. Radhakrishnan and A.J. McEvily: J. Eng. Mater. Technol., Trans. ASME, 1980, vol. 102, pp. 350-355.
- [95] J.A. Williams and A.T. Price: J. Eng. Mat. Technol., Trans. ASME, 1975, vol. 97, pp. 214-222.
- [96] V. Kumar and C.F. Shih: in Fracture Mechanics: Twelfth Conference, ASTM STP 700, P.C. Paris, ed., American Society for Testing and Materials, Philadelphia, PA, 1980, pp. 406-438.
- [97] V. Kumar and C.F. Shih: in Proceedings of the International Conference on Engineering Aspects of Creep, I. Mech. E. Conf. Publ., vol. 2, Edmunds, England, 1980, Paper No. C228/80, pp. 211-214.

Appendix 1

Stress Intensity Factor for Specimens With Side Grooves

The elastic stiffness of the arms of a specimen in which a bending mode of loading is dominant is almost not modified by the presence of side grooves. The elastic compliances of smooth specimens and of side-grooved specimens under such loading conditions are thus almost identical. The energy release rate per unit length of crack front is thus given by (9):

$$G_{\text{no side grooves}} = \frac{P^2}{2b} \left(\frac{\partial C}{\partial a} \right)_{\text{no side grooves}}$$

$$G_{\text{side grooves}} = \frac{P^2}{2b_{\text{net}}} \left(\frac{\partial C}{\partial a} \right)_{\text{side grooves}}$$

where G = the elastic energy release rate; and

C = the elastic specimen compliance.

Since $C_{\text{side grooves}} \approx C_{\text{no side grooves}}$, then:

$$G_{\text{side grooves}} = \left(\frac{b}{b_{\text{net}}} \right) G_{\text{no side grooves}}.$$

Since $K = \sqrt{EG}$, finally

$$K_{\text{side grooves}} = \left(\frac{b}{b_{\text{net}}} \right)^{1/2} K_{\text{no side grooves}}.$$

By substituting the expression for the stress intensity factor, then we derive expression for the gross section stress for the notched specimen with side grooves which is:

$$\sigma = \frac{P}{w \sqrt{BB_{\text{net}}}}$$

Appendix 2

COMPLIANCE CALIBRATION AT THE LOCATION OF KNIFE EDGES

FOR SMOOTH CT SPECIMENS

For CT specimens with no side grooves, the loading line normalized compliance $(Eb \frac{\Delta v}{\Delta P})_{LL}$ is given by ([35]):

$$\begin{aligned} (Eb \frac{\Delta v}{\Delta P})_{LL} = & \left(\frac{1 + a/w}{1 - a/w} \right)^2 \left(2.1630 + 12.219 \frac{a}{w} - 20.065 \left(\frac{a}{w} \right)^2 - 0.9925 \left(\frac{a}{w} \right)^3 \right. \\ & \left. + 20.609 \left(\frac{a}{w} \right)^4 - 9.9314 \left(\frac{a}{w} \right)^5 \right) \end{aligned} \quad (A2-1)$$

The normalized compliance at the location of the knife edges $(Eb \frac{\Delta v}{\Delta P})$ is given by:

$$(Eb \frac{\Delta v}{\Delta P}) = \left(\frac{x_0/w + 0.27}{x_0/w} \right) (Eb \frac{\Delta v}{\Delta P})_{LL} \quad (A2-2)$$

where x_0/w is the normalized location of the axis of rotation of the arms of the specimen given by ([35]):

$$\begin{aligned} \frac{x_0}{w} = & -0.0995314 + 3.02437 \frac{a}{w} - 7.95768 \left(\frac{a}{w} \right)^2 + 13.546 \left(\frac{a}{w} \right)^3 - 10.6274 \left(\frac{a}{w} \right)^4 \\ & + 3.1133 \left(\frac{a}{w} \right)^5 \end{aligned} \quad (A2-3)$$

A least square fit of a/w as a function of $(Eb \frac{\Delta v}{\Delta P})$ yields then:

$$\frac{a}{w} = 1.025 - 6.07807 U + 47.1092 U^2 - 509.145 U^3 + 2417.19 U^4 - 4064.67 U^5 \quad (A2-4)$$

where U is defined by:

$$U = 1 / \left((Eb \frac{\Delta v}{\Delta P})^{1/2} + 1 \right) \quad (B-2a)$$

with:

$E' = E$ under plane stress conditions

(B-2b)

$E' = \frac{E}{1 - \nu^2}$ under plane strain conditions.

(B-2c)

Appendix 3

EXPERIMENTAL STRESS INTENSITY FACTOR FOR SPECIMENS WITH 40% GROOVES

Assuming that the location (x_0/w) of the axis of rotation of the arms of the specimen is not affected by the presence of side grooves, the loading line compliance for CT specimens with 40% side grooves is given by:

$$(bE \frac{\Delta v}{\Delta P})_{LL} = (\frac{x_0/w}{x_0/w + .27}) \cdot (bE \frac{\Delta v}{\Delta P}) \quad (A3-1)$$

where x_0/w is given by (A2-3) as a function of a/w , a/w being obtained from (B-3):

$$x_0/w = -0.0995314 + 3.02437 \frac{a}{w} - 7.95768 \left(\frac{a}{w}\right)^2 + 13.546 \left(\frac{a}{w}\right)^3 - 10.6274 \left(\frac{a}{w}\right)^4 + 3.1133 \left(\frac{a}{w}\right)^5 \quad (A2-3)$$

$$\frac{a}{w} = .943769 - 4.29331 U + 38.0499 U^2 - 698.674 U^3 + 4721.32 U^4 - 10886.8 U^5 \quad (B-3)$$

with $U = 1/((Eb \frac{\Delta v}{\Delta P})^{1/2} + 1)$, $(Eb \frac{\Delta v}{\Delta P})$ being the compliance at the location of the knife edges.

A least square fit resulted in:

$$(Eb \frac{\Delta v}{\Delta P})_{LL} = \left(\frac{1 + a/w}{1 - a/w}\right)^2 (5.47027 - 4.6455 \frac{a}{w} - 23.0476 \left(\frac{a}{w}\right)^2 + 152.81 \left(\frac{a}{w}\right)^3 - 268.902 \left(\frac{a}{w}\right)^4 + 153.152 \left(\frac{a}{w}\right)^5) \quad (A3-2)$$

which leads to:

$$K_{exp} = \frac{P}{\sqrt{bb_{net}w}} \left(\frac{1}{2} \frac{\partial}{\partial} \frac{(Eb \Delta v / \Delta P) LL}{(a/w)} \right)^{1/2} \quad (A3-3)$$

or, by a least square fit:

$$K_{exp} = \frac{P}{\sqrt{bb_{net}w}} \frac{(2 + a/w)}{(1 - a/w)^{3/2}} \left(.374907 + 6.52948 \frac{a}{w} - 10.5935 \left(\frac{a}{w} \right)^2 \right. \\ \left. + .703939 \left(\frac{a}{w} \right)^3 + 6.28030 \left(\frac{a}{w} \right)^4 \right) \quad \text{which is (B-8).} \quad (A3-4)$$

TABLE I

CREEP CRACK GROWTH CORRELATIONS
IN STRUCTURAL ALLOYS

1) Nickel - Base - Superalloys

<u>Alloy</u>	<u>Testing Conditions</u>	<u>Specimen Geometries</u>	<u>da/dt (m/s)</u>	<u>Loading Parameters</u>	<u>Stage II Correlation</u>	<u>References</u>
Astroloy (Forged)	704°C Air	CT	2×10^{-8} - 3×10^{-6}	σ_{net} K (30-70 MPa \sqrt{m})	no correl. $r \approx 6$	34, 46
Astroloy (P/M-HIP)	650-760°C Air, Argon	SEN(T)	1×10^{-9} - 6×10^{-6}	K (30-90 MPa \sqrt{m})	$r \approx 6$	43, 14
Astroloy (P/M-HIP)	704°C Air, Argon	SEN(T)	1×10^{-9} - 1×10^{-6}	K (20-90 MPa \sqrt{m})	$r \approx 3$ (Air) $r \approx 9$ (Ar)	36
Udimet 700 (Forged)	650-850°C Air	CT	7×10^{-9} - 7×10^{-7}	σ_{nom} (eq. 11) (500-1500 MPa)	$r \approx 5$	18, 13, 4
				K (50-150 MPa \sqrt{m})	$r \approx 5$	
				C* (eq. 16)	poor correl.	
				$(8 \times 10^{-8} - 1 \times 10^{-5})$ MPa.m/s)		

TABLE I (cont'd)

CREEP CRACK GROWTH CORRELATIONS
IN STRUCTURAL ALLOYS

1) Nickel - Base - Superalloys (cont'd)

<u>Alloy</u>	<u>Testing Conditions</u>	<u>Specimen Geometries</u>	<u>da/dt (m/s)</u>	<u>Loading Parameters</u>	<u>Stage II Correlation</u>	<u>References</u>
Udimet 700 (rolled)	850°C Air, Vacuum	CT	6×10^{-9} - 2×10^{-6}	K (40-100 MPa \sqrt{m})	$n=4$	48
IN 100 (Gatorized)	650°C Air	Cst-K DCB CC	1×10^{-9} - 3×10^{-8}	K (30-50 MPa \sqrt{m})	$n=7$	49
IN 100	700°C Air	SEN(T)	3×10^{-10} - 1×10^{-4}	K (20-150 MPa \sqrt{m})	$n=1.4-4.7$	50
IN 100 (P/M-HIP)	730°C Air	CT Ring Spec.	1×10^{-7} - 4×10^{-6}	σ_{net} (30-60 MPa) C^* (eq. 16) $(5 \times 10^{-7} - 1 \times 10^{-5} \text{ MPa}\cdot\text{m/s})$	$n=5$ (CT only) $n=0.7$ (CT only)	19
IN 100 (P/M-HIP)	704°C Air, Argon	SEN(T)	1×10^{-9} - 3×10^{-6}	K (30-90 MPa \sqrt{m})	$n=5$	
Merl 76 (P/M-HIP)	704°C Air	CC	1×10^{-8} - 2×10^{-6}	K (20-100 MPa \sqrt{m}) K (13-25 MPa \sqrt{m})	$n=3$ $n=5$	33 51

TABLE I (cont'd)

CREEP CRACK GROWTH CORRELATIONS
IN STRUCTURAL ALLOYS

1) Nickel - Base - Superalloys (cont'd)

Alloy	Testing Conditions	Specimen Geometries	da/d. (m/s)	Loading Parameters	Stage II Correlation	References
Merl 76 (P/M-HIP)	704°C Air, Argon	SEN(T)	1×10^{-9} - 2×10^{-5}	K (15-100 MPa \sqrt{m})	$n \approx 3-4$	33
Merl 76 (P/M-HIP)	700°C Air	SEN(T)	1×10^{-7} - 1×10^{-6}	K (20-100 MPa \sqrt{m})	$n \approx 3$	52
IN 792 (Forged)	700°C Air	CT	-	K, σ_{net}	-	34
IN 792 (P/M-HIP, Wrought)	650-760°C Air	CT	-	K	-	44, 46
René 95 (Forged)	700°C Air	CT	5×10^{-7} - 1×10^{-4}	σ_{net}	no correl.	34, 46
				K (20-40 MPa \sqrt{m})	$n=8$	
René 95 (P/M-HIP)	650-760°C Air, Argon	SEN(T)	6×10^{-9} - 2×10^{-6}	K (10-90 MPa \sqrt{m})	$n \approx 4-6$	45
René 95 (P/M-HIP)	700°C Air, Argon	SEN(T)	1×10^{-9} - 1×10^{-6}	K (12-80 MPa \sqrt{m})	$n \approx 1-4$	33
Inconel X-750 (Rolled)	540-650°C Air, Vacuum	CT	6×10^{-9} - 8×10^{-6}	K (30-120 MPa \sqrt{m})	$n \approx 1-4$	48, 4

TABLE I (cont'd)

CREEP CRACK GROWTH CORRELATIONS
IN STRUCTURAL ALLOYS

1) Nickel - Base - Superalloys (cont'd)

<u>Alloy</u>	<u>Testing Conditions</u>	<u>Specimen Geometries</u>	<u>da/dt (m/s)</u>	<u>Loading Parameters</u>	<u>Stage II Correlation</u>	<u>References</u>
Inconel X-750 (Rolled)	650°C Air, Argon	SEN(T)	1×10^{-9} - 1×10^{-5}	K (20-70 MPa \sqrt{m})	$n \approx 6$	53
Inconel X-750 (Rolled)	540-650°C Air, Vacuum	CT	6×10^{-9} - 8×10^{-6}	K (30-120 MPa \sqrt{m})	$n \approx 1-4$	41
				C^* (eq. 28)	$n \approx 1.0$	
				$(3 \times 10^{-7} - 8 \times 10^{-6}$ MPa.m/s)		
Inconel 600 (Rolled)	540-870°C Air, Vacuum	CT	No CCG Observed	-	-	41
Inconel 625 (Rolled)	650-760°C Air	CT	4×10^{-9} - 3×10^{-7}	K (40-100 MPa \sqrt{m})	$n \approx 7$	41
				C^* (eq. 28)	$n \approx 0.6-1.6$	
				$(3 \times 10^{-7} - 4 \times 10^{-6}$ MPa.m/s)		
IN 718 (Hot Rolled)	540-760°C Air	CT	3×10^{-7} - 8×10^{-6}	K (20-70 MPa \sqrt{m})	$n \approx 3$	34, 46
				σ_{net}	no correl.	

TABLE I (cont'd)

CREEP CRACK GROWTH CORRELATIONS
IN STRUCTURAL ALLOYS

1) Nickel - Base - Superalloys (cont'd)

<u>Alloy</u>	<u>Testing Conditions</u>	<u>Specimen Geometries</u>	<u>da/dt (m/s)</u>	<u>Loading Parameters</u>	<u>Stage II Correlation</u>	<u>References</u>
IN 718 (Rolled)	540-760°C Air	CT	7×10^{-9} - 7×10^{-6}	K (20-100 MPa \sqrt{m})	$n \approx 1$	17
				σ_{nom} (eq. 11) (200-1500 MPa)	no correl.	
				C^* (eq. 16) $(6 \times 10^{-10} - 3 \times 10^{-7}$ MPa.m/s)	$n \approx 0.3$	
IN 718 (Hot Rolled)	540-650°C Air, Vacuum	CT	3×10^{-10} - 1×10^{-6}	K (20-100 MPa \sqrt{m})	$n \approx 1$	13, 48
IN 718 (Hot Rolled)	425-760°C Air	CT	3×10^{-10} - 2×10^{-5}	K (20-100 MPa \sqrt{m})	$n \approx 1$	4
IN 718 (P/M-HIP)	540-650°C Air, Argon	SEN(T)	2×10^{-10} - 1×10^{-5}	K (10-80 MPa \sqrt{m})	$n \approx 7$	36

TABLE I (cont'd)

CREEP CRACK GROWTH CORRELATIONS
IN STRUCTURAL ALLOYS

1) Nickel - Base - Superalloys (cont'd)

<u>Alloy</u>	<u>Testing Conditions</u>	<u>Specimen Geometries</u>	<u>da/dt (m/s)</u>	<u>Loading Parameters</u>	<u>Stage II Correlation</u>	<u>References</u>
Inconel 738 (Cast)	850°C Air	SEN	1×10^{-10} - 1×10^{-5}	K (20-100 MPa \sqrt{m})	n=5	54
Nimonic 105 (Wrought)	750°C Air	SEN	1×10^{-10} - 1×10^{-6}	K (20 - 100 MPa \sqrt{m})	n=3	54
Nimonic 115 (Extruded)	700°C Air	CT	2×10^{-8} - 7×10^{-6}	K (40 - 90 MPa \sqrt{m})	n=6	34, 46
AF 115 (P/M-HIP)	700°C Air	CC	1×10^{-9} - 1×10^{-6}	K (10 - 30 MPa \sqrt{m})	n=5	51
Nimonic PE16 (Hot Rolled)	650°C Air, Vacuum	CT	3×10^{-9} - 2×10^{-7}	K (60 - 120 MPa \sqrt{m})	n=5	41
Waspaloy (Forged)	700°C Air	CT	5×10^{-8} - 5×10^{-6}	σ_{net}	no correl.	34, 46
				K (20-50 MPa \sqrt{m})	n=5	
Waspaloy (Forged)	650-700°C Air, Argon	SEN(T), CT	2×10^{-10} - 7×10^{-5}	K (20-130 MPa \sqrt{m})	n=4-6	35
Mar-M432(B6) (P/M-HIP)	700°C Air	CC	3×10^{-6} - 7×10^{-6}	K (15-30 MPa \sqrt{m})	n=1	51

TABLE (1)

CREEP CRACK GROWTH CORRELATIONS
IN STRUCTURAL ALLOYS

2) Aluminum Alloys

Alloy	Testing Conditions	Specimen Geometries	da/dt (m/s)	Loading Parameters	Stage II Correlation	References
2219-T851	150°C Air	CT	$7 \times 10^{-9} - 7 \times 10^{-6}$	K (16-45 MPa \sqrt{m})	$n=3.4$	24
RR 58	100-200°C Air	Cst-K DCB	$8 \times 10^{-10} - 2 \times 10^{-7}$	K (18-24 MPa \sqrt{m})	$n=30$	24
RR 58	150°C Air	Cst-K DCB	$3 \times 10^{-9} - 3 \times 10^{-8}$	C* (eq. 29b)	$0.5 \leq n \leq 1.0$	43,42
RR 58	150°C Air	Cst-K DCB, DCB, DT	$8 \times 10^{-10} - 8 \times 10^{-7}$	K (13-30 MPa \sqrt{m})	no correl.	72
				C* (eq. 29b)	poor correl.	
				C* (eq. 29a)	$n=0.9$	
RR 58	100-200°C Air	Cst-K DCB	$1 \times 10^{-10} - 6 \times 10^{-8}$	K (15-25 MPa \sqrt{m})	no correl.	15
				C* (eq. 29a)	$n=0.9$	
RR 58	150-200°C Air	Cst-K DCB	$3 \times 10^{-9} - 6 \times 10^{-7}$	C* (eq. 29a)	$n=0.9$	30
				$(3 \times 10^{-10} - 6 \times 10^{-8})$ MPa.m/s		
6061	220-320°C Air	CT	$6 \times 10^{-9} - 2 \times 10^{-7}$	K, σ_{net} , σ_{ref}	no correl.	73,94
				C* (eq. 29a)	no correl.	
				C* (eq. 28)	no correl.	
				C* (eq. 16)	no correl.	
				\dot{a}	no correl.	
				$(\dot{a}/(P/P_0)^2)^{1/\theta}$	$\theta=0.5-0.9$	
					$\alpha=1.3-6.0$	

Table II

Powder Size

	Mesh	Particle diameter, μm
Astroloy	100	149
Merl-76	325	45
In-100	60	250
Rene-95	60	250
Rene-95	120	125

Table III

Thermal Processing

1. HIP Cycle

a. Astroloy - 1232° C/4 hours/furnace cool/15 Ksi

b. IN-100, Merl-76, Rene-95 - 1177°C/4 hours/ Furnace Cool/15 Ksi

2. Heat Tretament

Solution: 1177°C/4 hours/air cool

Age: 871°C/8 hours/air/cool

982°C/4 hours/air/cool

650°C/24 hours/air/cool

760°C/8 hours/air/cool

Table IV

Alloy Chemistries

	Sample 1 Astroloy %	Sample 2 Rene-95 %	Sample 3 Merl-76 %	Sample 4 IN-100 %
Chromium	14.8	14.0	12.2	12.2
Cobalt	16.3	7.71	17.8	18.3
Molybdenum	4.82	3.33	3.20	3.39
Columbium	.004	3.36	1.36	<.001
Aluminum	3.97	3.31	4.71	4.88
Titanium	3.39	2.41	4.19	4.17
Hafnium	.01	.01	.10	<.01
Vanadium	<.001	.007	.009	.97
Carbon	.044	.082	.034	.082
Boron	.025	.007	.020	.021
Zirconium	.037	.064	.050	.037
Oxygen	.0129	.0137	.0238	.0111
Sulfur	<.001	.001	<.001	<.001
Phosphorus	.014	<.001	<.001	<.001
Nitrogen	.0008	.0020	.0029	.0016
Silicon	.02	.07	.10	.04
Iron	.24	.18	.077	.082
Tungsten		3.42		
Nickel	Remainder	Remainder	Remainder	Remainder
γ' Volume Fraction (Calculated)	0.46	0.38	0.58	0.63

Table V

704°C Tensile Test Results

	U.T.S. (MPa)	.2% Y.S. (MPa)	% El.	E (GPa)	Bp (MPa)	Np
Rene-95	1199	947	5.0	167	1083	.099
IN-100	1167	1012	8.4	162	1103	.058
MERL-76	1164	1012	13.1	160	1103	.056
Astroloy	1200	950	15.4	170	1055	.088

Table VI

Alloy	$\frac{\epsilon_{\text{crit/air}}}{\epsilon_{\text{crit/argon}}}$	$\frac{\text{w/o B in G.B.}}{\text{w/o B in G.B. Astroloy}}$
Astroloy	1.0	1.0
MERL-76	0.2	.30
IN-100	0.71	.70
Rene-95	0.1	.26

Table VII

Heat Treatments

Temper	Solution Treatment	Aging Treatment	Final Hardness (Rockwell B Scale)
T-851	535-540°C/Quenched	175-180°C for 18-36 hrs	74 ± 1
T-mod	540°C for 2 hours/ Water Quenched	510°C for 2 hours/Water Quenched/177°C for 18 hours	61 ± 1

Table VIII

Chemical Composition of 2219 Aluminum Alloy (w%)

Cu	Mn	Zr	V	Ti	Si	Fe	Mg	Zn	Other	Al
6.3	.3	.18	.10	.06	<.2	<.3	<.02	<.10	<.05 .15 max total	Bal.

Table IX

Grain Boundary Precipitate
Average Diameter and Spacing

	Average Diameter (μm)	Average Spacing (μm)
2219 - T851	0.6	3
2219 - Tmod	3	8

Table X

Tensile Test Results

Material	T(°C)	Deformation Rate (s ⁻¹)	E (MPa)	Y (MPa)	UTS (MPa)	Fracture Elongation (%)	B _p (t)	n _p
2219-T851	150	3 x 10 ⁻⁴	-	287	324	17	1.9 x 10 ⁻⁴⁹	19
2219-T851	175	3 x 10 ⁻⁴	7.1 x 10 ⁴	272	297	17	7.0 x 10 ⁻⁴⁹	23
2219-T851	200	3 x 10 ⁻⁴	6.8 x 10 ⁴	242	262	17	1.3 x 10 ⁻⁶²	25
2219-T851	175	3 x 10 ⁻³	7.1 x 10 ⁴	286	325	19	9.8 x 10 ⁻⁴⁹	18
2219-T851	175	3 x 10 ⁻⁵	7.1 x 10 ⁴	256	272	16	1.05 x 10 ⁻⁷⁴	30
2219-Tmod	175	3 x 10 ⁻³	7.1 x 10 ⁴	232	279	30	2.7 x 10 ⁻³⁷	14
2219-Tmod	175	3 x 10 ⁻⁴	7.1 x 10 ⁴	232	265	30	1.0 x 10 ⁻⁴³	17
2219-Tmod	175	3 x 10 ⁻⁵	7.1 x 10 ⁴	225	245	18	2.0 x 10 ⁻⁵	21

$$\epsilon(t)_{(p1)} = B_p \sigma(MPa)^{n_p}$$

Table XI

Secondary

Creep Strain Rates

Material	T(°C)	$B_c^{(\dagger)}$	n_c
2219-T851	150	1.1×10^{-69}	26
2219-T851	175	1.2×10^{-63}	24
2219-T851	200	1.4×10^{-59}	23
2219-T851	175	1.3×10^{-50}	19

$$^{(\dagger)} \dot{\epsilon}^{(cr)} (s^{-1}) = B_c \sigma (MPa)^{n_c}$$

Table XII

Creep Rupture Data at 175°C in air

Material	m	$C_{M.C.}$	$\epsilon_f^{(cr)} = \dot{\epsilon}_s^{(cr)} t_f$
2219-T851	0.91	0.08	0.024 ± 0.008
2219-Tmod	0.88	1.19	0.23 ± 0.06

Table XIII

Crack Growth Tests Performed on CT Specimens

Heat Treatment	Spec I.D.	Orient	Side Grooves (%)	Temp (°C)	Envir	Type of Test	R	Frequency (Hz)	Hold Time(s)	Loading Time(s)	Initial K_{max} (MPa \sqrt{m})
T851	19A04	(L-T)	40	175	AIR	CGR, P-5344M	0.5	-	var.	10	16
T851	19B01	(L-T)	40	175	AIR	CGR, P-5344M	0.5	-	var.	10	18
T851	19B03	(L-T)	40	175	AIR	CGR, P-5344M	0.5	9.8×10^{-4}	1000	10	16
T851	19B04	(L-T)	40	175	AIR	CGR, P-5344M	0.5	3.1×10^{-3}	300	10	16
T851	19B02	(L-T)	40	175	AIR	CGR, P-5344M	0.5	8.3×10^{-3}	100	10	16
T851	19B05	(L-T)	40	175	AIR	CGR, P-5344M	0.5	0.02	30	10	16
T851	19B09	(L-T)	40	175	AIR	CGR, P-5344M	0.5	0.03	10	10	16
T851	19B06	(L-T)	40	175	AIR	CGR, P-5344M	0.05	8.3×10^{-5}	100	10	16
T851	19B29	(L-T)	40	175	AIR	CGR, P-3786M	1.0	-	-	10	16
T851	19B18	(L-T)	40	175	AIR	CGR, P-6618M	0.5	9.8×10^{-4}	1000	10	16
T851	19B17	(L-T)	40	175	AIR	CGR, P-6146M	0.5	3.1×10^{-3}	300	10	16
T851	19B20	(L-T)	40	175	AIR	CGR, P-6681M	0.5	8.3×10^{-3}	100	10	20
T851	19B19	(L-T)	40	175	AIR	CGR, P-8017M	0.5	8.3×10^{-3}	100	10	25
T851	19B24	(L-T)	40	175	AIR	CGR, K-16MPa \sqrt{m}	0.5	3.1×10^{-3}	300	10	16
T851	19B22	(L-T)	40	175	AIR	CGR, K-20MPa \sqrt{m}	0.5	8.3×10^{-3}	100	10	20
T851	19B23	(L-T)	40	175	AIR	CGR, K-25MPa \sqrt{m}	0.5	8.3×10^{-3}	100	10	25
T851	19B21	(L-T)	40	198	AIR	CGR, P-5344M	0.5	8.3×10^{-3}	100	10	16
T851	19B16	(L-T)	40	175	AIR	FCP, P-5344M	0.05	0.02	-	10	16
T851	19B14	(L-T)	40	175	AIR	FCP, P-5344M	0.05	0.1	-	10	16
T851	19B08	(L-T)	40	175	AIR	FCP, P-5344M	0.05	1	-	10	16
T851	19B15	(L-T)	40	175	AIR	FCP, P-5344M	0.05	3	-	10	16
Tmod	19M03	(L-T)	40	175	AIR	FCP, P-5344M	0.5	3.1×10^{-3}	300	10	20
Tmod	19M01	(L-T)	40	175	AIR	CGR, K-20MPa \sqrt{m}	0.5	3.1×10^{-3}	300	10	20
Tmod	19M02	(L-T)	40	175	AIR	CGR, K-25MPa \sqrt{m}	0.5	3.1×10^{-3}	300	10	25

Table XIV

Crack Growth Tests Performed on DCB Specimens

HEAT TREATMENT	SPEC. I.D.	ORIENT.	SIDE GROOVES (%)	TEMP (°C)	ENVIR.	KNIFE-EDGES OPENING DISPL.(m)	APPROXIMATE INITIAL K(MPa \sqrt{m})
T851	TL02	(T-L)	40	175	Air	3.8×10^{-4}	14
T851	TL03	(T-L)	40	175	Vacuum	3.8×10^{-4}	14
T851	TL05	(T-L)	40	175	Air	4.6×10^{-4}	17
T851	SL05	(S-L)	40	175	Air	3.8×10^{-4}	14
T851	SL07	(S-L)	40	175	Vacuum	3.8×10^{-4}	14
T851	SL08	(S-L)	40	175	Air	4.6×10^{-4}	17
T851	SL09	(S-L)	40	175	Vacuum	4.6×10^{-4}	16

Table XV

Creep Crack Growth Test Results in 2219-T851 at 175°C using DCB Specimens

Specimen I.D.	Environment	Initial K (MPa \sqrt{m})	Initial Crack Length (cm)	Test Duration (s)	Crack Length Increment	Average Crack Growth Rate	Estimated K (using eq. (VIII-7)) (MPa \sqrt{m})
TL02	Air	13.7	1.176 \pm 0.010	1.2 \times 10 ⁶	310 \pm 40	2.6 \times 10 ⁻¹⁰	8.2
TL03	Vacuum	13.8	1.166 \pm 0.005	1.2 \times 10 ⁶	220 \pm 50	1.8 \times 10 ⁻¹⁰	8.1
TL05	Air	16.9	1.138 \pm 0.010	5.9 \times 10 ⁵	480 \pm 70	8.1 \times 19 ⁻¹⁰	10.1
SL06	Air	13.8	1.161 \pm 0.003	1.2 \times 10 ⁶	350 \pm 70	2.9 \times 10 ⁻¹⁰	8.2
SL07	Vacuum	13.8	1.161 \pm 0.001	1.2 \times 10 ⁶	390 \pm 90	3.2 \times 10 ⁻¹⁰	8.2
SL08	Air	16.8	1.146 \pm 0.003	5.9 \times 10 ⁵	650 \pm 80	1.1 \times 10 ⁻⁹	10.0
SL09	Vacuum	16.3	1.184 \pm 0.003	5.9 \times 10 ⁵	730 \pm 70	1.2 \times 10 ⁻⁹	9.7

Table XVI

Relative Amount of Intergranular Fracture
for Creep Crack Growth Tests
in 2219-T851 and 2219-Tmod

Material	Specimen Geometry	Specimen ID	Specimen Orientation	K (MPa \sqrt{m})	da/dt (m/s)	Percentage of Intergranular Fracture Area (%)
2219-T851	CT	19B23	(T-L)	25	3×10^{-7}	28
2219-T851	CT	19B22	(T-L)	20	1×10^{-7}	34
2219-T851	CT	19B24	(T-L)	16	4×10^{-8}	53
2219-T851	DCB	TL02	(T-L)	<10	$\sim 3 \times 10^{-10}$	>90
2219-T851	DCB	SL06	(S-L)	<10	$\sim 3 \times 10^{-10}$	~ 100
2219-Tmod	CT	19M02	(T-L)	25	3×10^{-8}	67
2219-Tmod	CT	19M01	(T-L)	20	1×10^{-8}	80

Table XVII

Expressions of Different Loading Parameters for CT Specimens

• Stress intensity factor:

$$K = \frac{P}{(bb_{\text{net}}w)^{1/2}} \frac{(2 + a/w)}{(1 - a/w)^{3/2}} f(a/w) \quad (91,92,93)$$

with $f(a/w) = .886 + 4.64(a/w) - 13.32(a/w)^2 + 14.72(a/w)^3 - 5.6(a/w)^4$

• Net section stress:

$$\sigma_{\text{net}} = \frac{P}{b_{\text{net}}(w - a)}$$

• Nominal stress:

$$\sigma_{\text{nom}} = \frac{P}{b_{\text{net}}(w - a)} \left(1 + 3 \frac{w + a}{w - a}\right) \quad (17,18)$$

• Reference stress:

$$\sigma_{\text{ref}} = 2.02 \frac{P}{b_{\text{net}}w} \frac{(1 + a/w)}{(1 - a/w)^2} \quad (71,40,95)$$

• C* integral:

$$C^* = \frac{b}{b_{\text{net}}} B_c(w-a) h_1(a/w, n_c) [P/(\alpha b(w-a)n(a/w))]^{n_c} + 1 \quad (96,97)$$

with $\alpha = 1.455$ in plane strain

$\alpha = 1.072$ in plane stress

$$n(a/w) = \left[\left(\frac{2a}{w-a} \right)^2 + 2 \left(\frac{2a}{w-a} \right) + 2 \right]^{1/2} - \left[\left(\frac{2a}{w-a} \right) + 1 \right]$$

$$h_1(a/w, 20)^\dagger = 27.33 - 228.8(a/w) + 745.7(a/w)^2 - 1181(a/w)^3$$

$$+ 912.7(a/w)^4 - 275.0(a/w)^5 \quad \text{for } 0.25 < a/w < 1.0$$

[†]The error which arises from the fact that $h_1(a/w, n_c)$ is assumed to be equal to $h_1(a/w, 20)$ is estimated as being negligible.

Table XVIII

Comparison between the Measured and the Predicted
Steady State Creep Crack Growth Rates for
Constant-K Tests

	2219 - T851		2219 - Tmod	
	K=20 MPa \sqrt{m}	K=25 MPa \sqrt{m}	K=20 MPa \sqrt{m}	K=25 MPa \sqrt{m}
Predicted CCGR (m/s)	1×10^{-7}	6×10^{-7}	7×10^{-9}	8×10^{-8}
Measured CCGR (m/s)	1×10^{-7}	3×10^{-7}	1×10^{-8}	3×10^{-8}

TYPICAL CREEP CRACK GROWTH CURVE

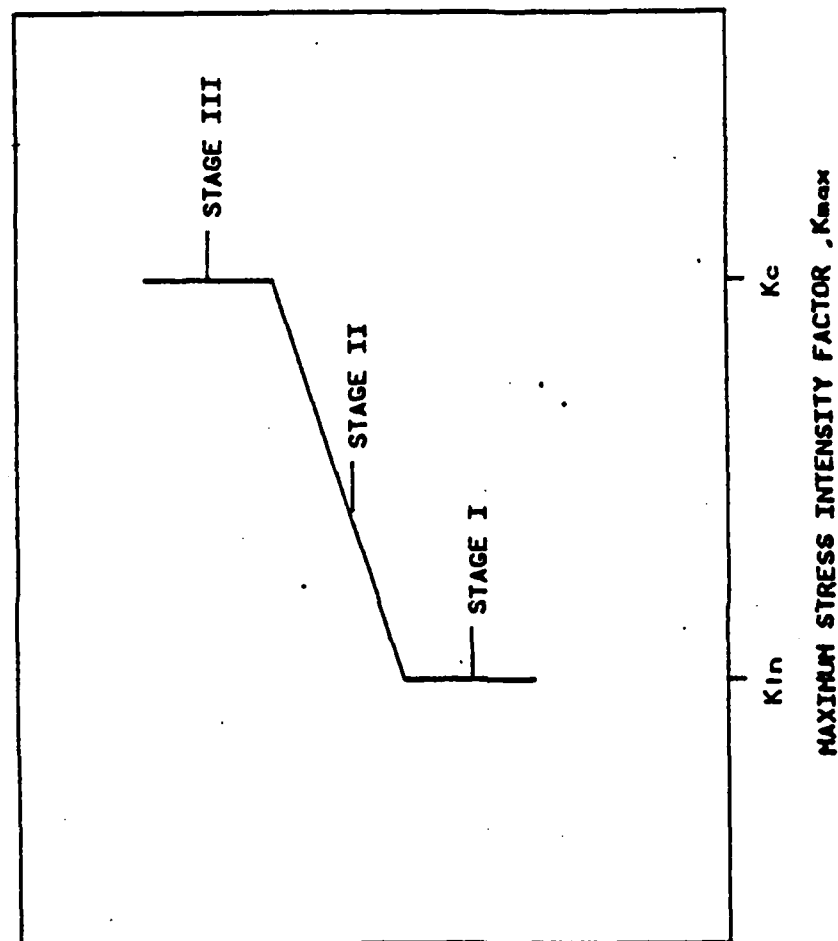


FIGURE (1) Typical log - log creep crack growth curve

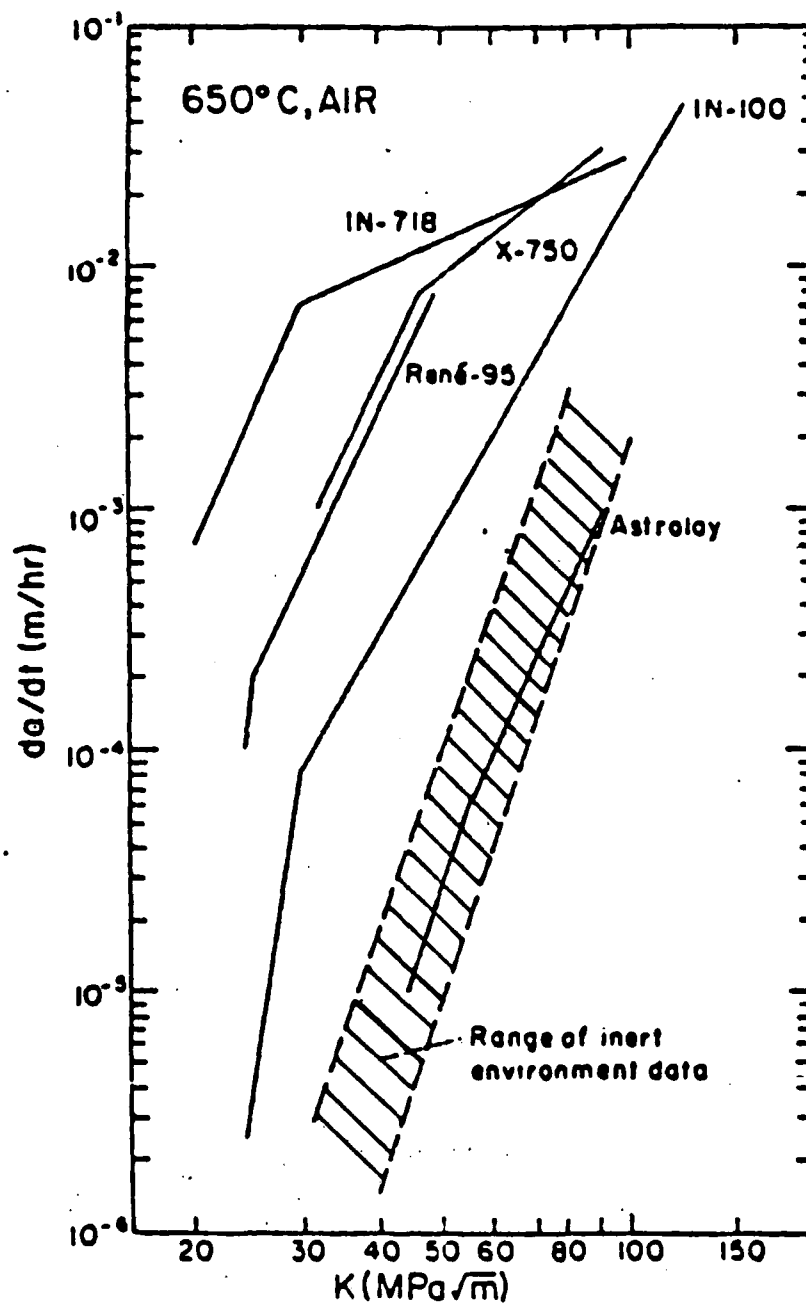


FIGURE (2) Creep crack growth rates in several nickel-base-superalloys

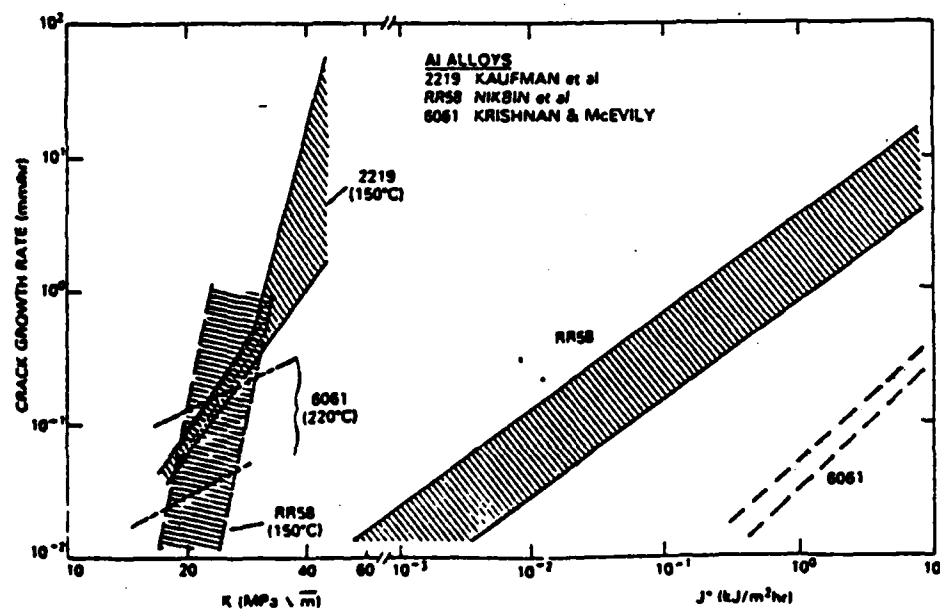
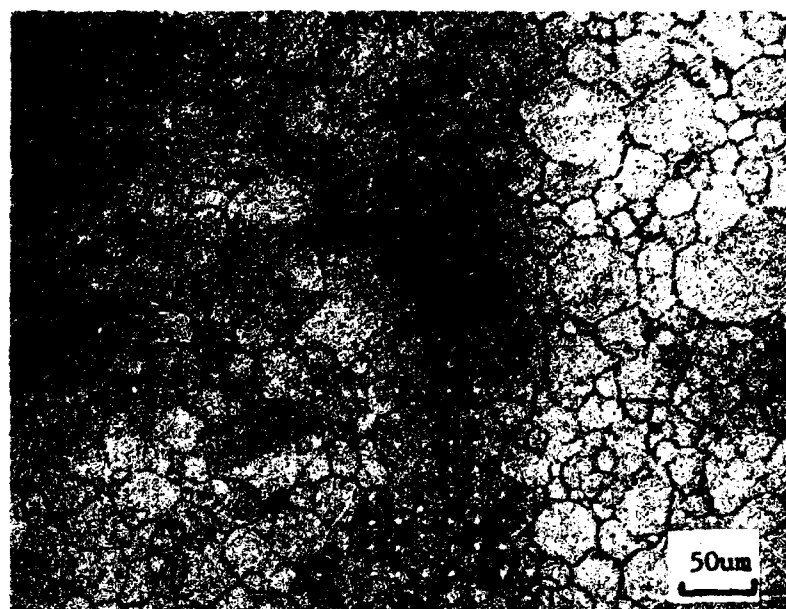
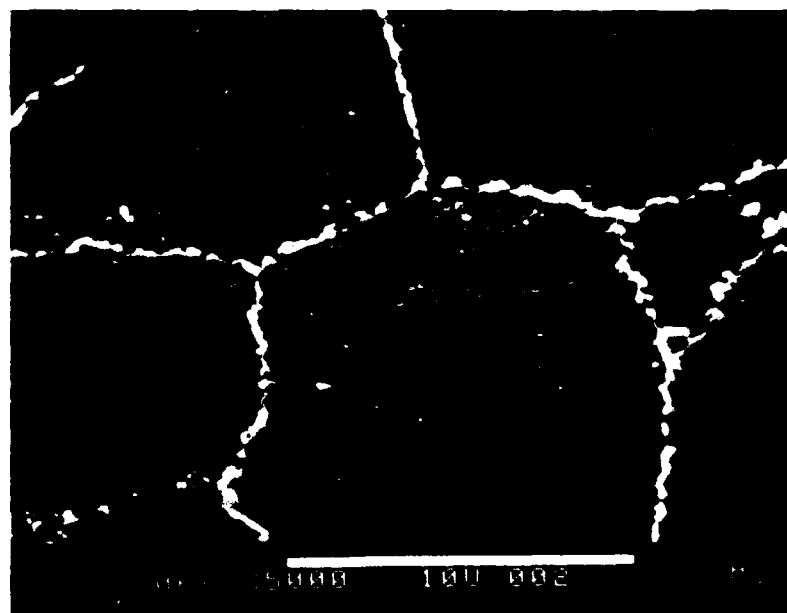


FIGURE (3) Creep crack growth rates in several aluminum alloys

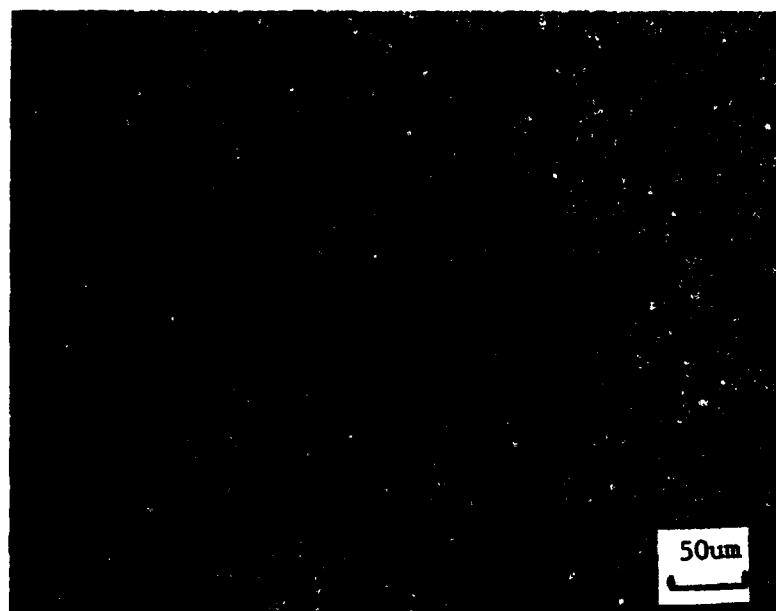


(a)

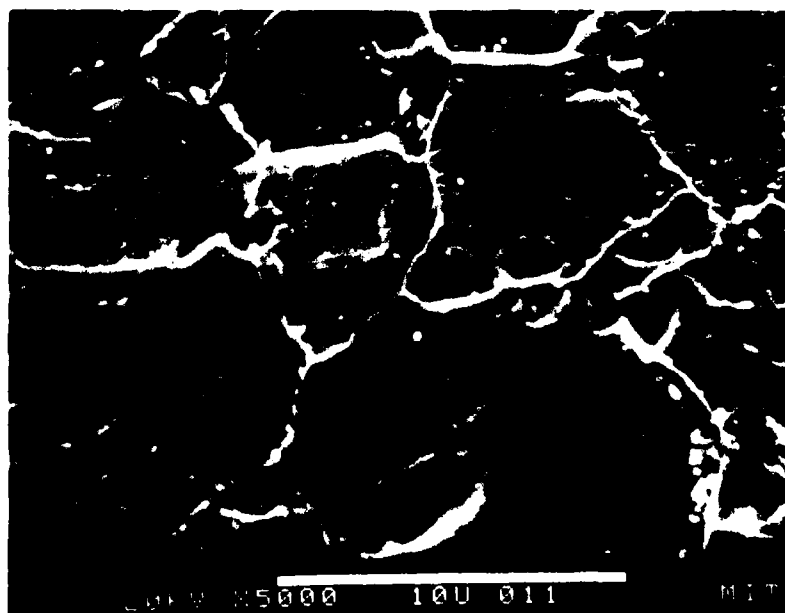


(b)

FIGURE (4) Photomicrographs of PM/HIP low carbon Astroloy.
(a) optical, (b) SEM (etchant: 100ml Methanol,
50ml HCl, and 5g FeCl_3)

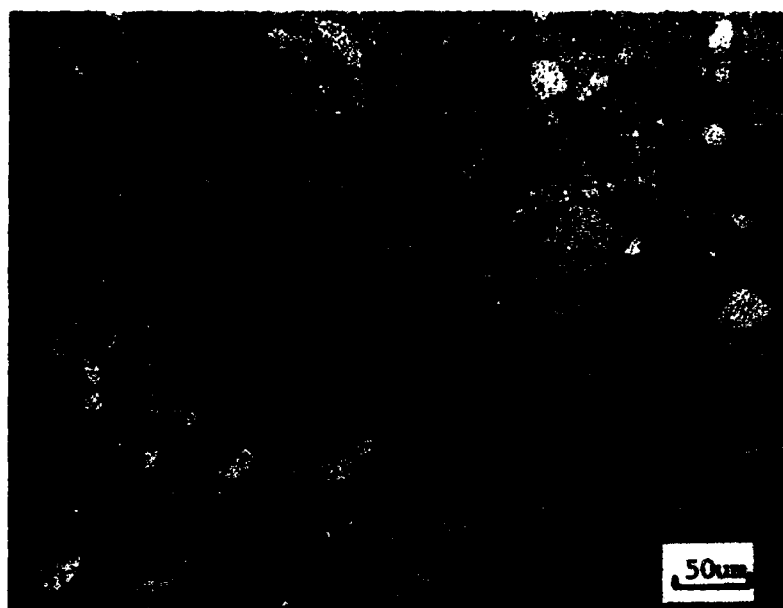


(a)

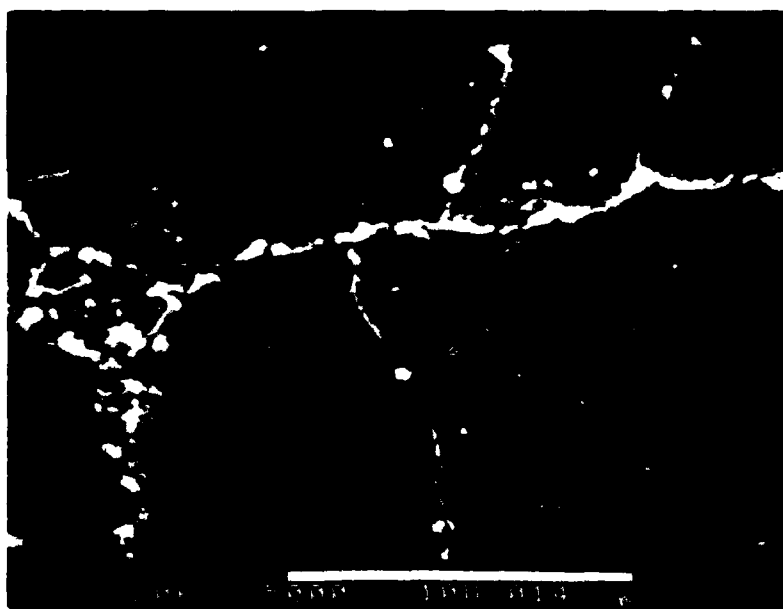


(b)

FIGURE (5) Photomicrographs of PM/HIP MERL-76. (a) optical
(b) SEM (etchant: 100ml Methanol, 50ml HCl, and
5g FeCl_3)

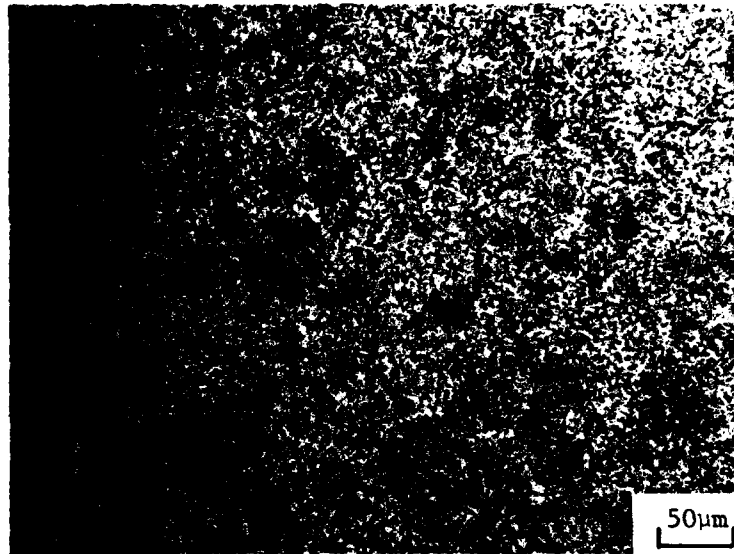


(a)



(b)

FIGURE (6) Photomicrographs of PM/HIP low carbon IN-100.
(a) optical, (b) SEM. (etchant: 100 ml Methanol,
50 ml HCl, and 5 gm FeCl_3)



Photomicrograph of P/M HIP Rene 95. mag. 200X (etchant:
100 ml methanol, 50 ml HCl, 5 g FeCl_3)

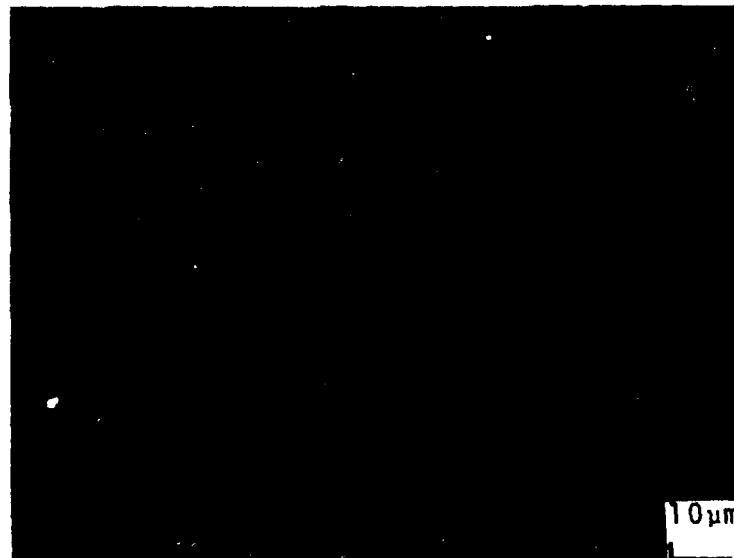


Figure (7) Photomicrograph of P/M HIP RENE 95. mag. 1000X (etchant:
100 ml methanol, 50 ml HCl, 5 g FeCl_3)

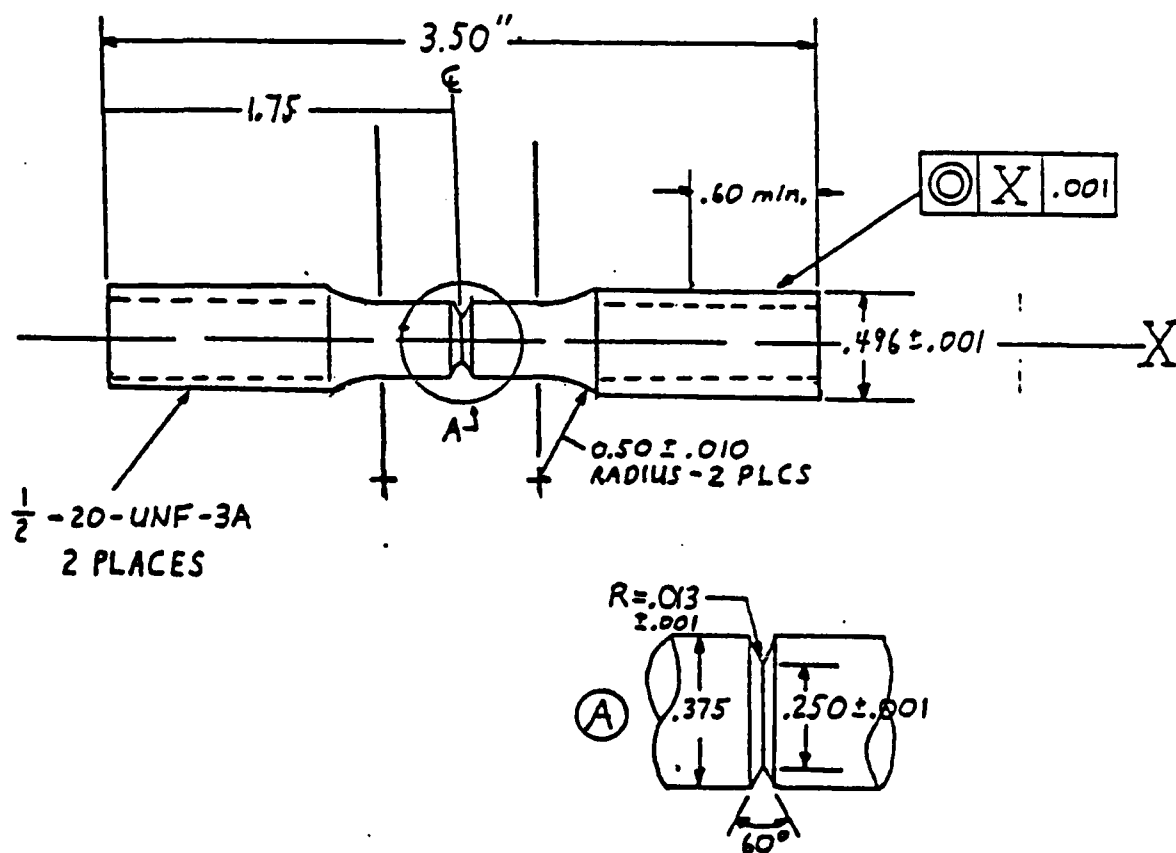


FIGURE (8) Notched Stress-Rupture (NSR) specimen geometry.
(Dimensions in inches)

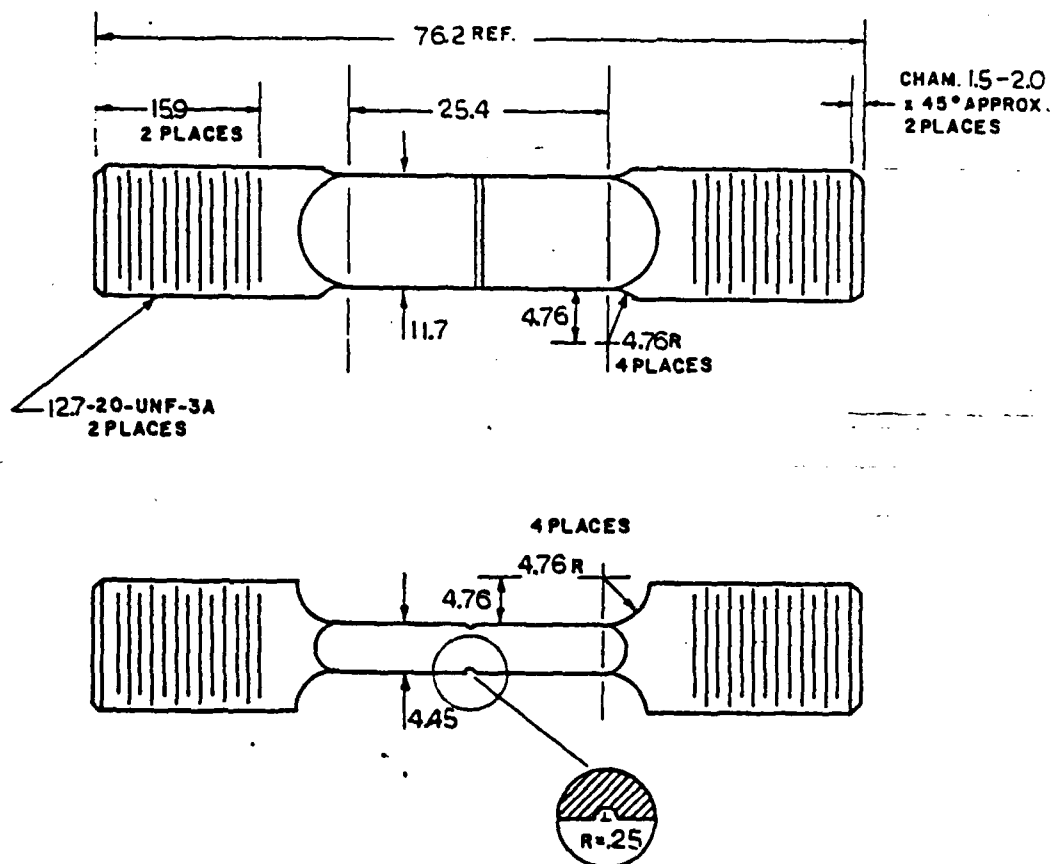


FIGURE (9) Single Edge Notched (SEN) specimen geometry used in CCGR tests. (Dimensions in mm)

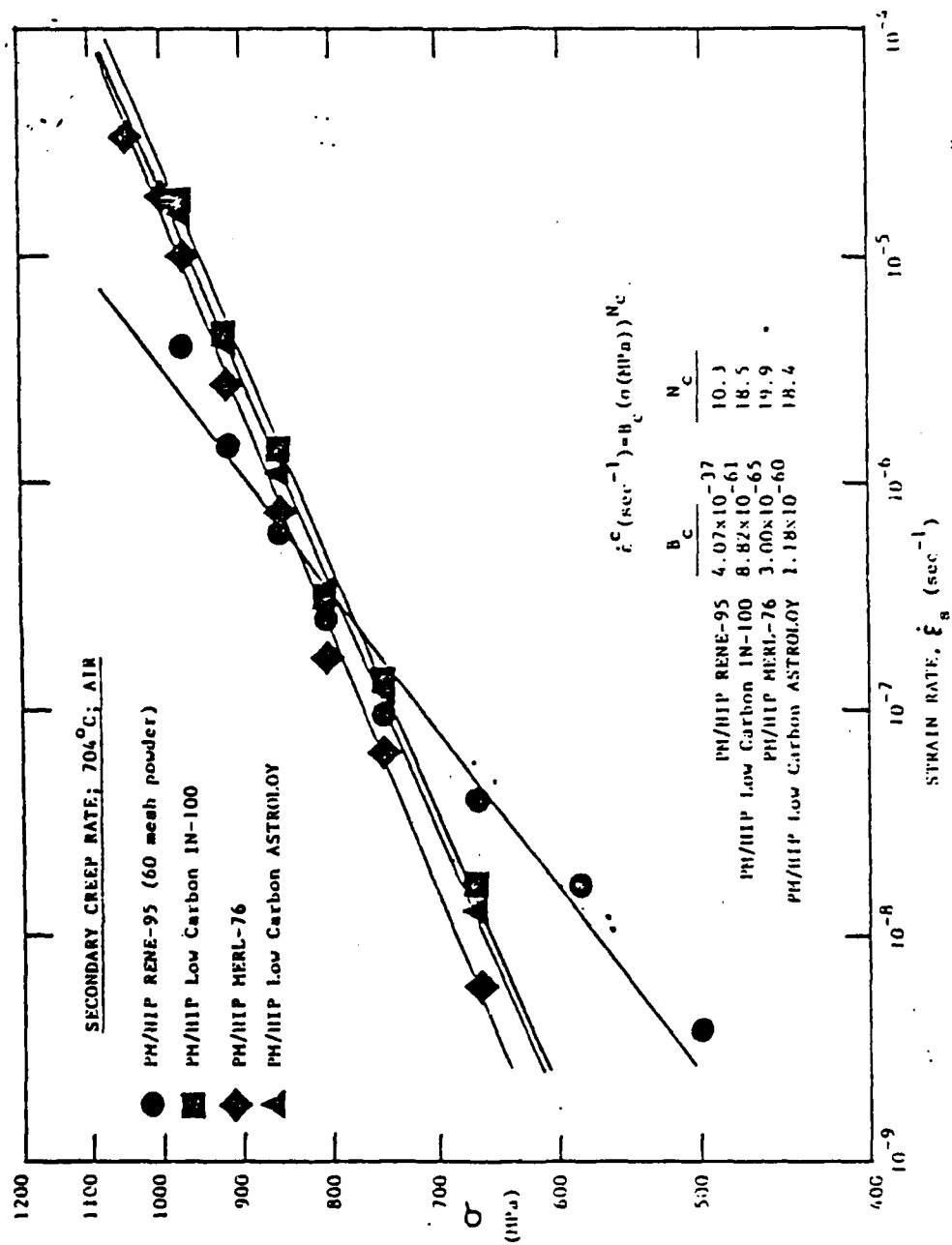


FIGURE (10) Secondary creep rate results for four PM/HiP Nickel-Ba Superalloys at 704°C.

AD-A141 193

EXPERIMENTAL AND THEORETICAL STUDIES OF CREEP CRACK
GROWTH(U) MASSACHUSETTS INST OF TECH CAMBRIDGE
R M PELLOUX ET AL. 20 MAR 84 AFOSR-TR-84-0387

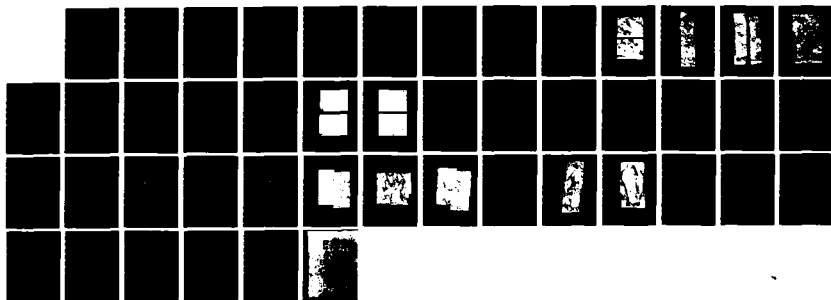
2/2

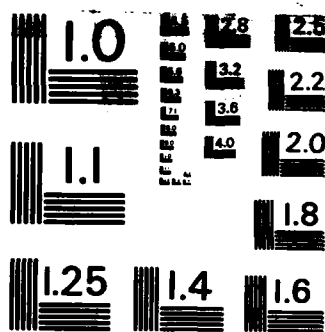
UNCLASSIFIED

AFOSR-82-0087

F/G 11/6

NL





MICROCOPY RESOLUTION TEST CHART
NATIONAL BUREAU OF STANDARDS-1963-A

CCGR PM/HIP low carbon ASTROLOY; 704C

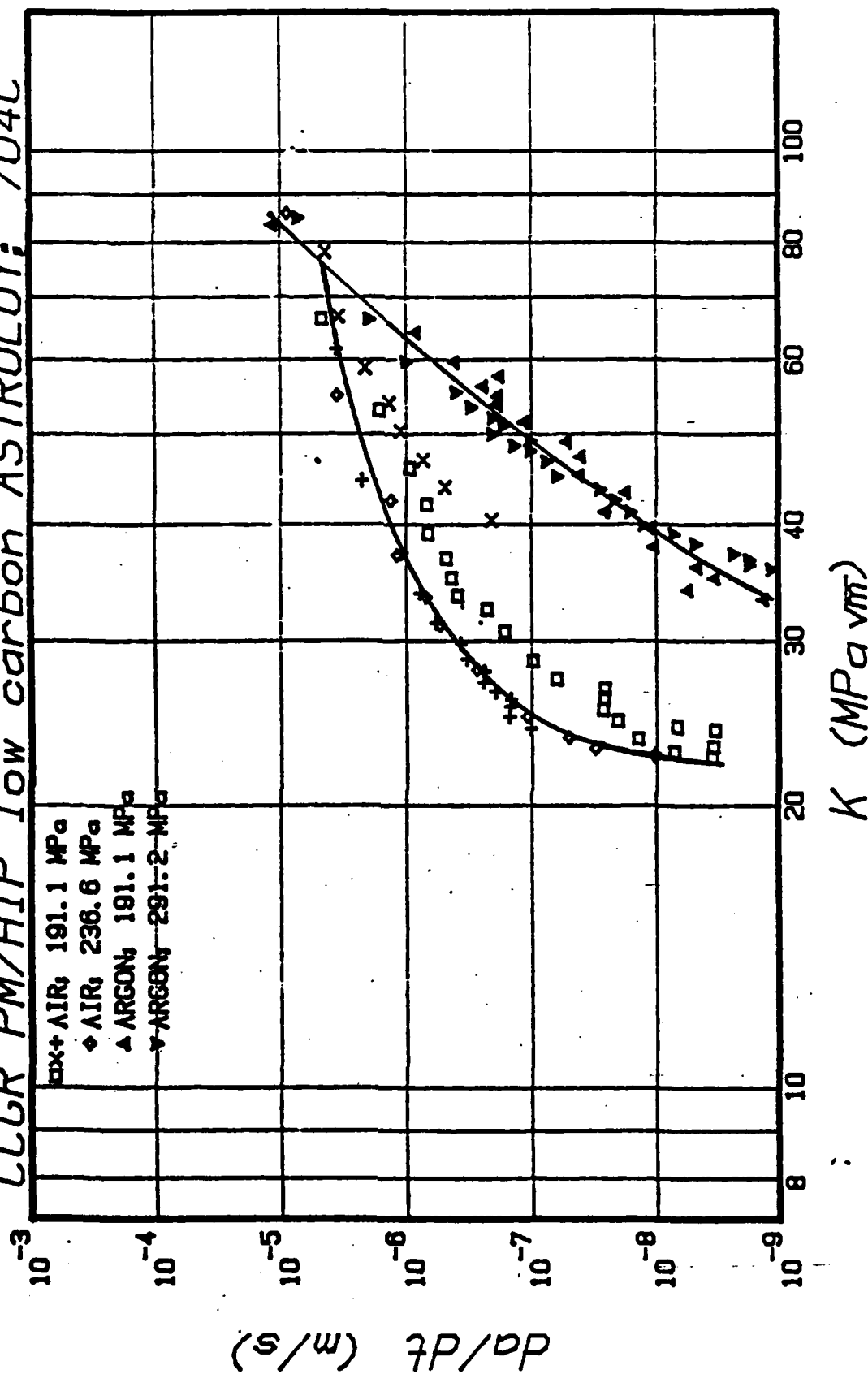


FIGURE (11) CCGR results for PM/HIP low carbon ASTROLOY at 704°C in both air and in 99.999% pure argon.

CCGR PM/HIP MERL-76; 704C

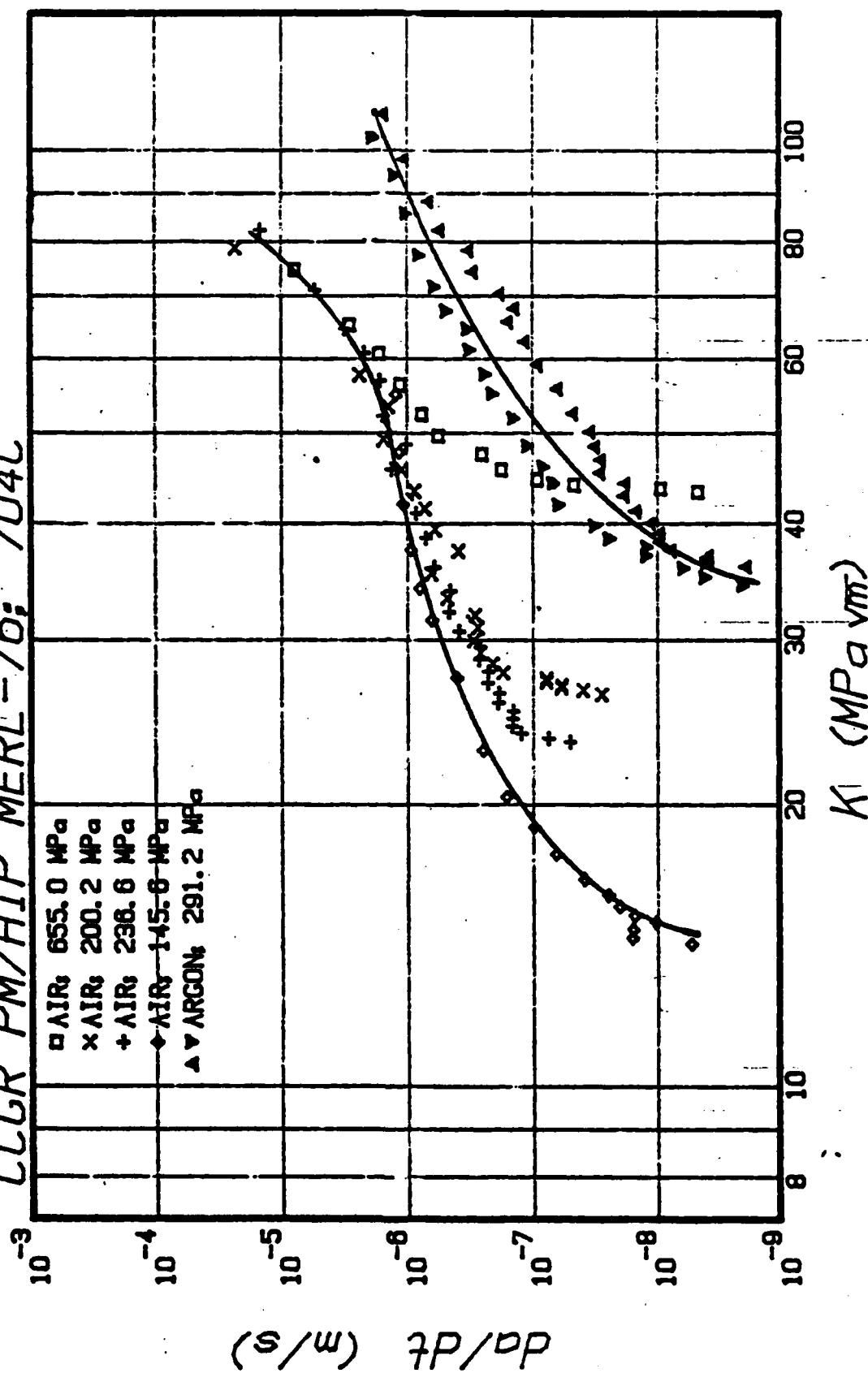
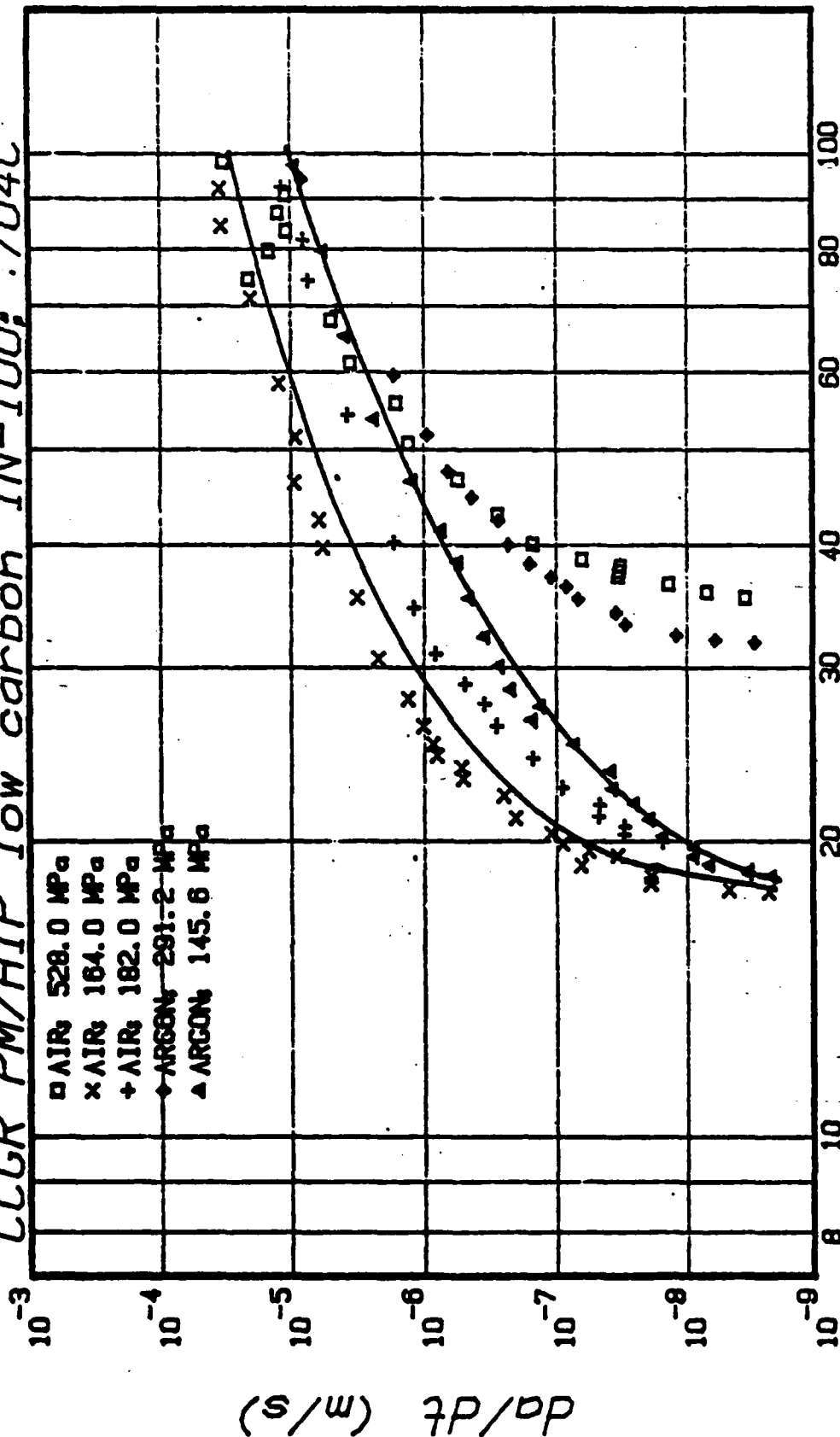


FIGURE (12) CCGR results for PM/HIP MERL-76 at 704°C in both air and 99.999% pure argon.

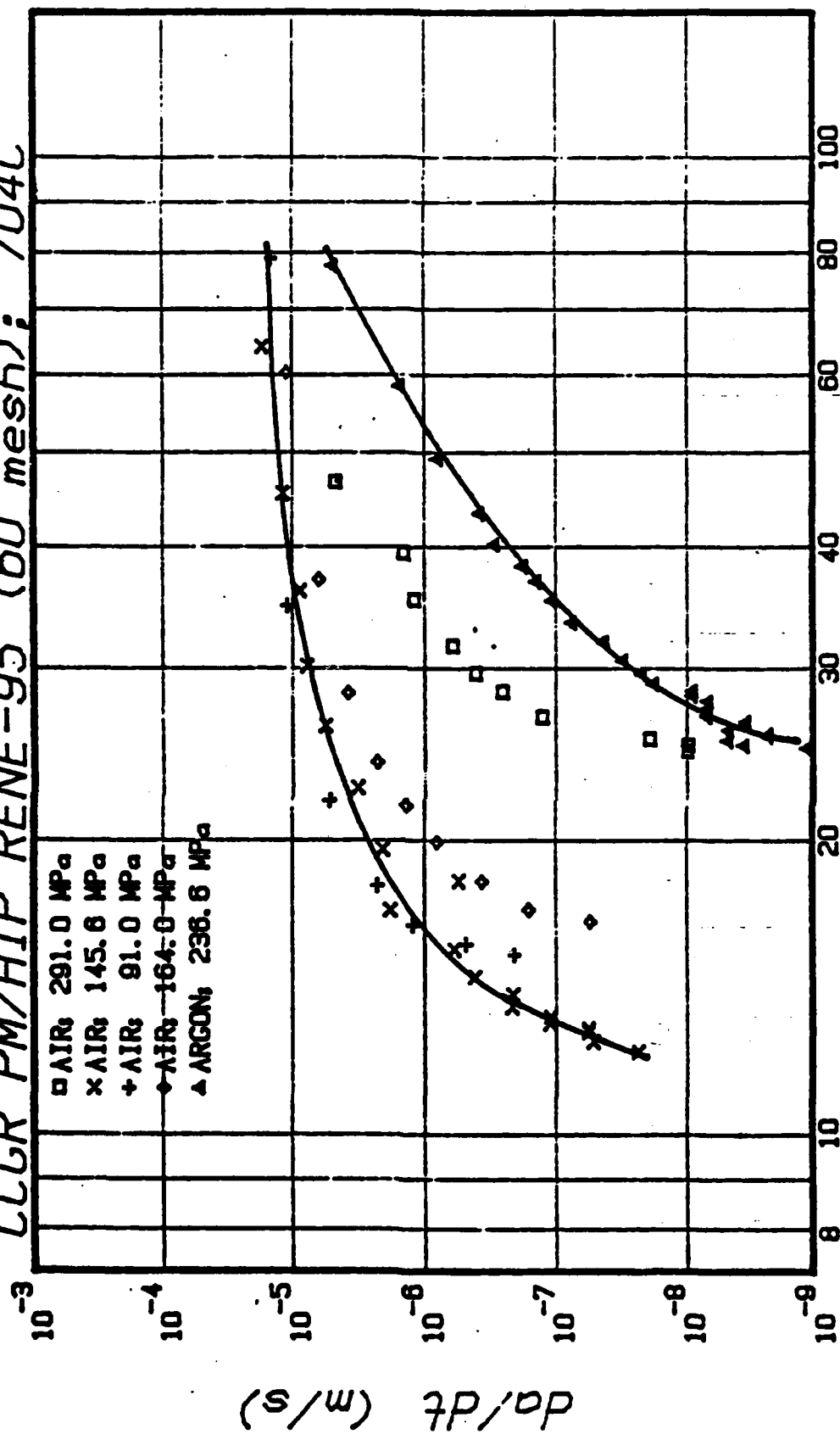
CCGR PM/HIP low carbon IN-100; 704C



$K \text{ (MPa } \sqrt{m})$

FIGURE (13) CCGR results for PM/HIP low carbon IN-100 at 704°C in both air and in 99.999% pure argon.

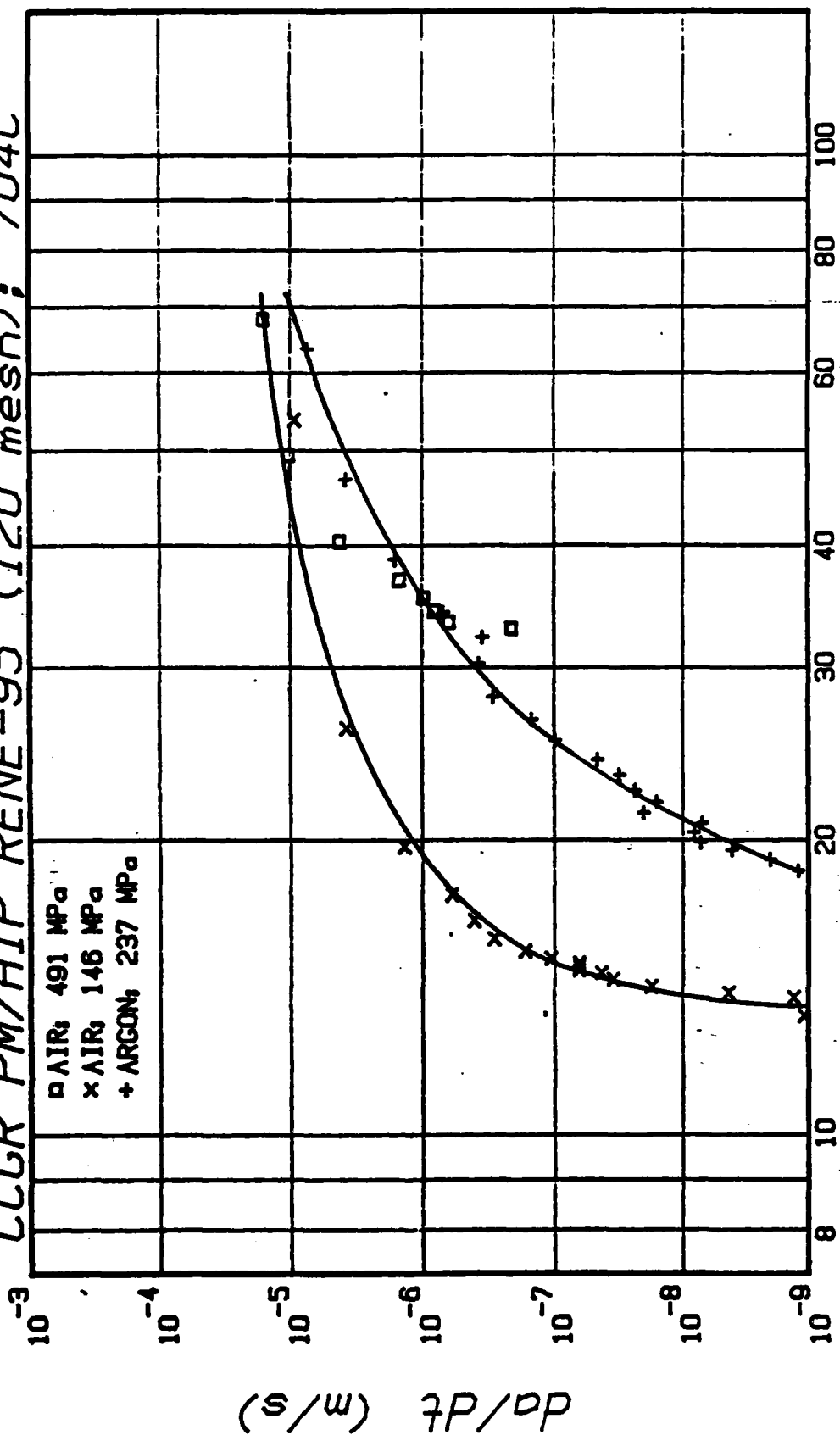
CCGR PM/HIP RENE-95 (60 mesh); 704C



K (MPa cm)

FIGURE (14) CCGR results for PM/HIP RENE-95 (60 mesh powder) at 704°C in both air and in 99.999% pure argon.

CCGR PM/HIP RENE-95 (120 mesh); 704C



K (MPa cm)

FIGURE (15) CCGR results for PM/HIP RENE-95 (120 mesh powder) in both air and in 99.999% pure argon.

CCGR PM/HIP MERL-76; 704C

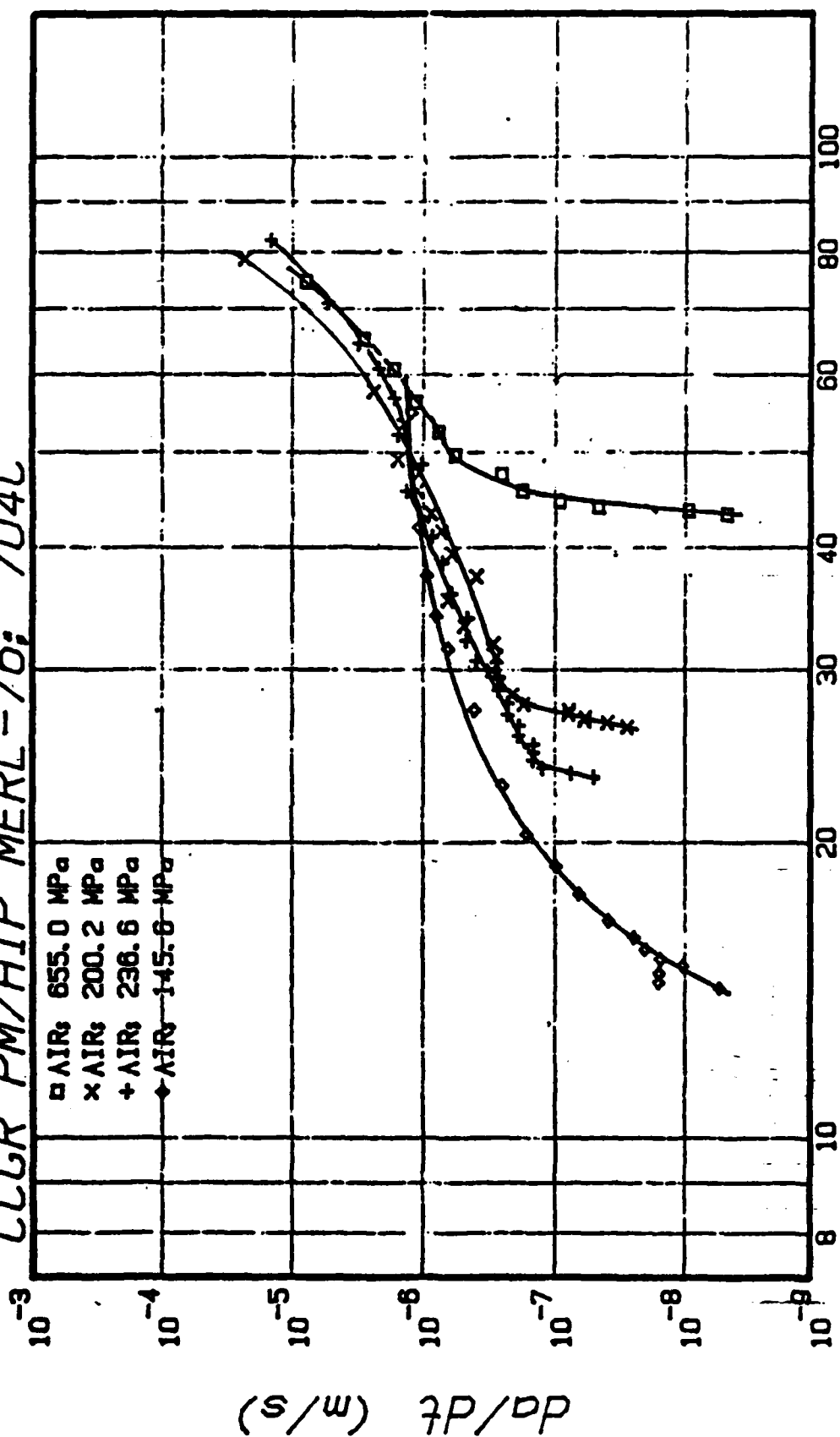


FIGURE (16) CCGR results for PM/HIP MERL-76 in air at 704°C for different initial K and gross section stresses.

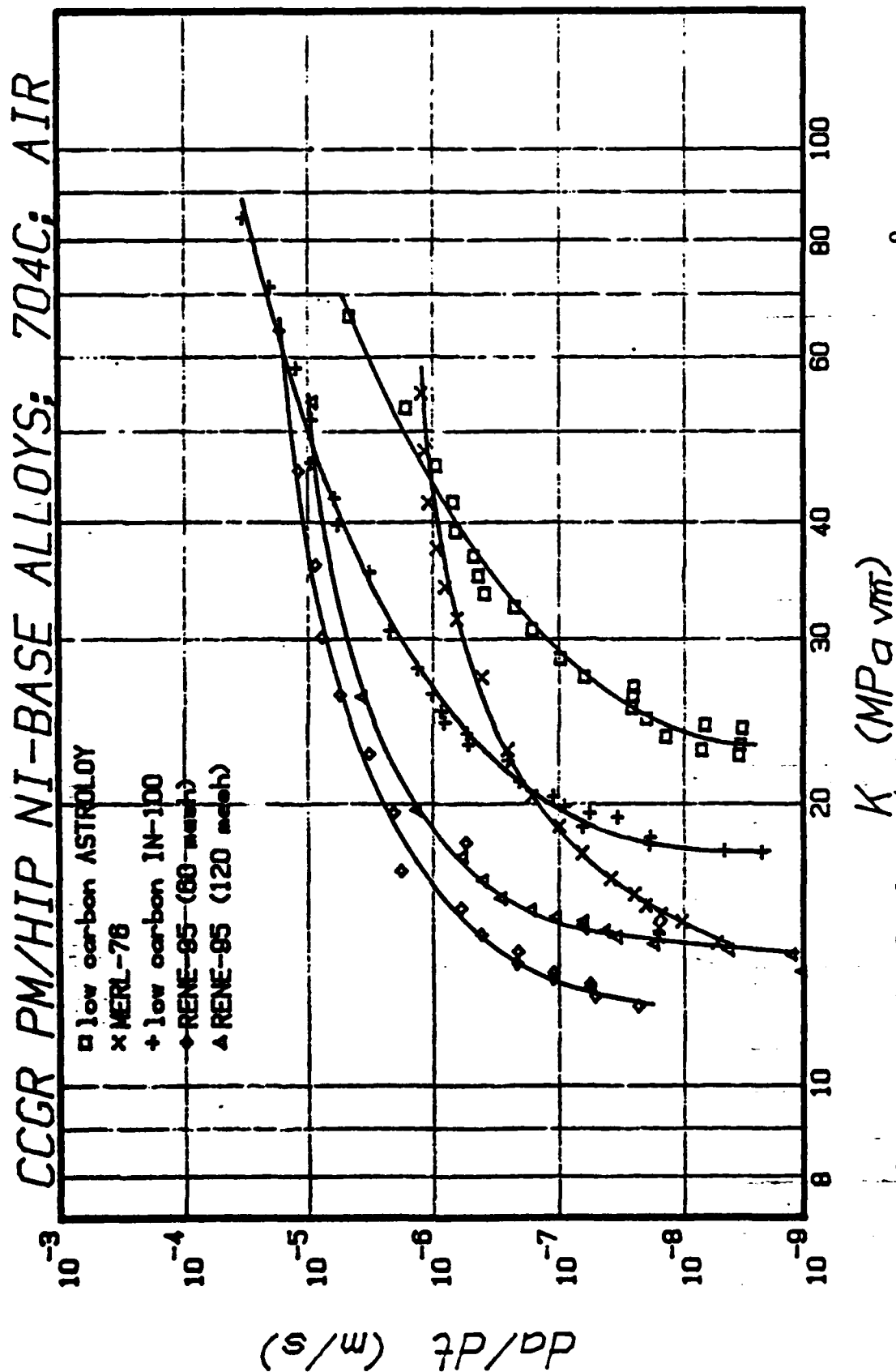
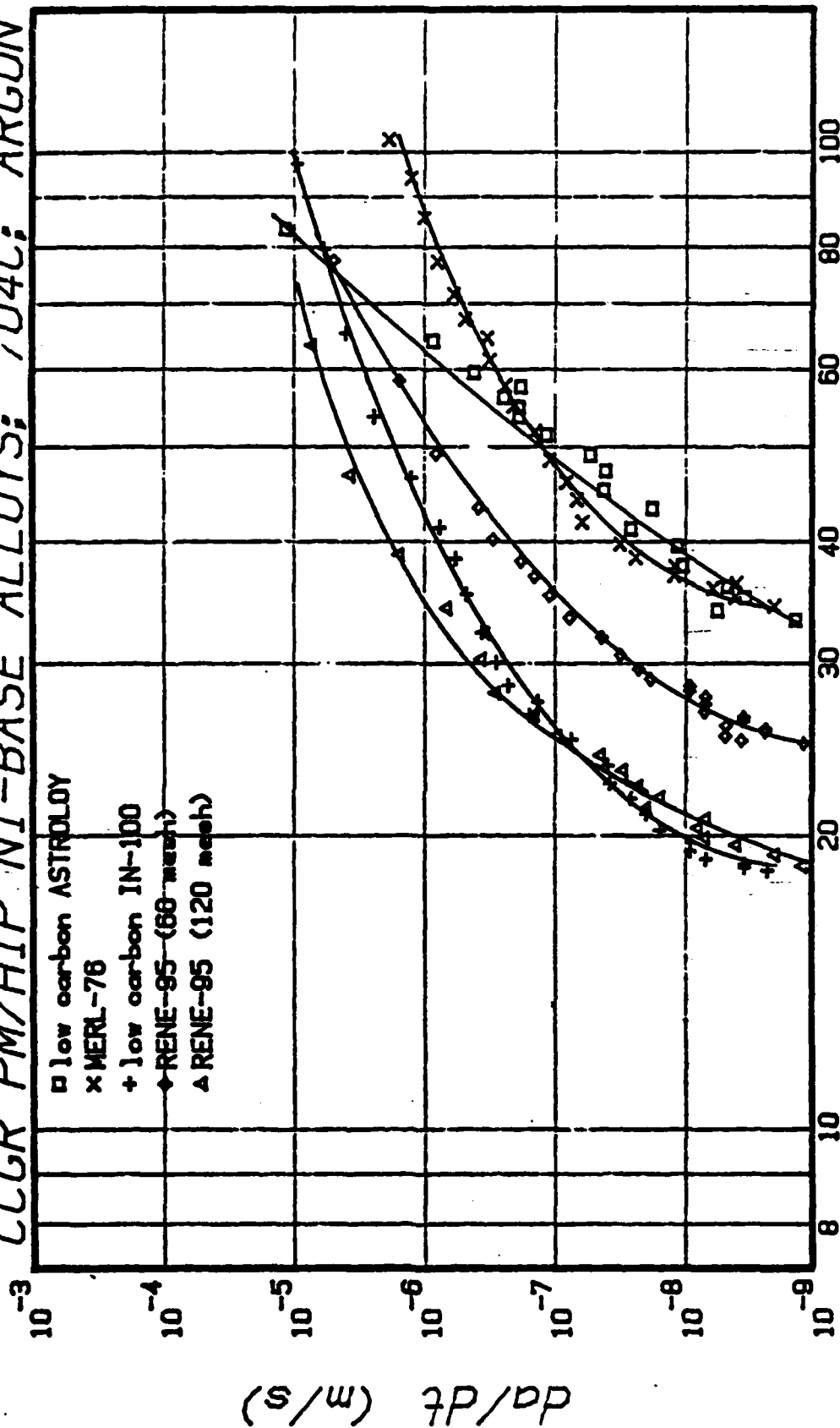


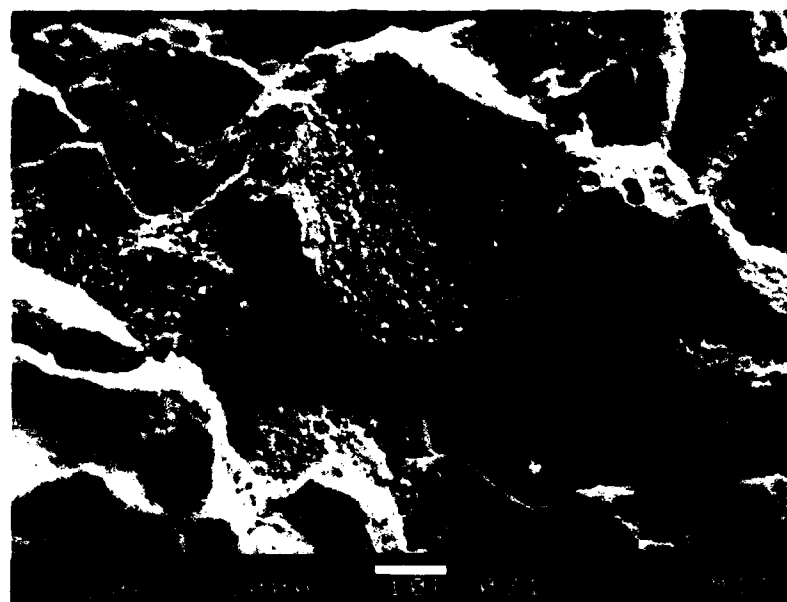
FIGURE (17) CCGR results for five PM/HIP Nickel-Base Superalloys in air at 704°C.

CCGR PM/HIP NI-BASE ALLOYS; 704C; ARGON

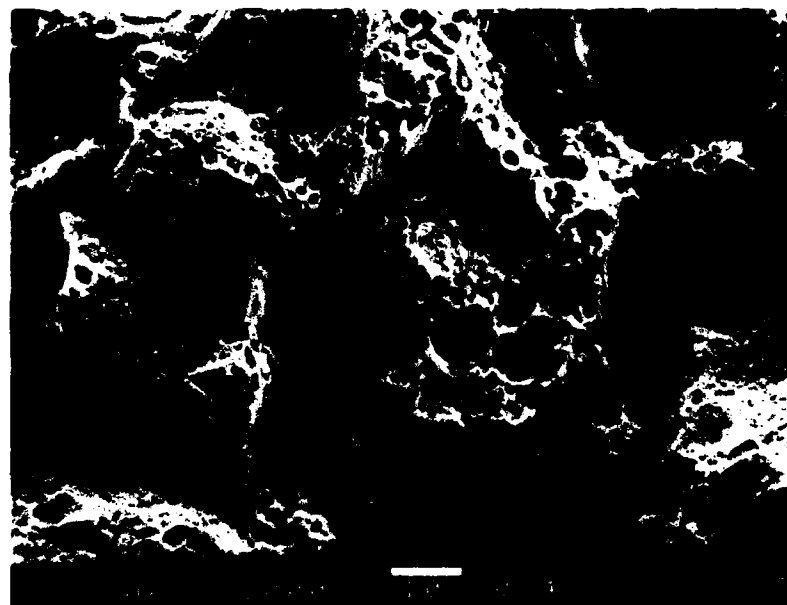


$K \text{ (MPa}\sqrt{\text{m}}\text{)}$

FIGURE(18) CCGR results for five PM/HIP Nickel-Base Superalloys in 99.999% pure argon at 704°C.



(a)



(b)

FIGURE (19) Fractographs of PM/HIP Low C ASTROLOY at 704°C.
(a) CCGR test in air; (b) CCGR test in 99.999% pure argon.

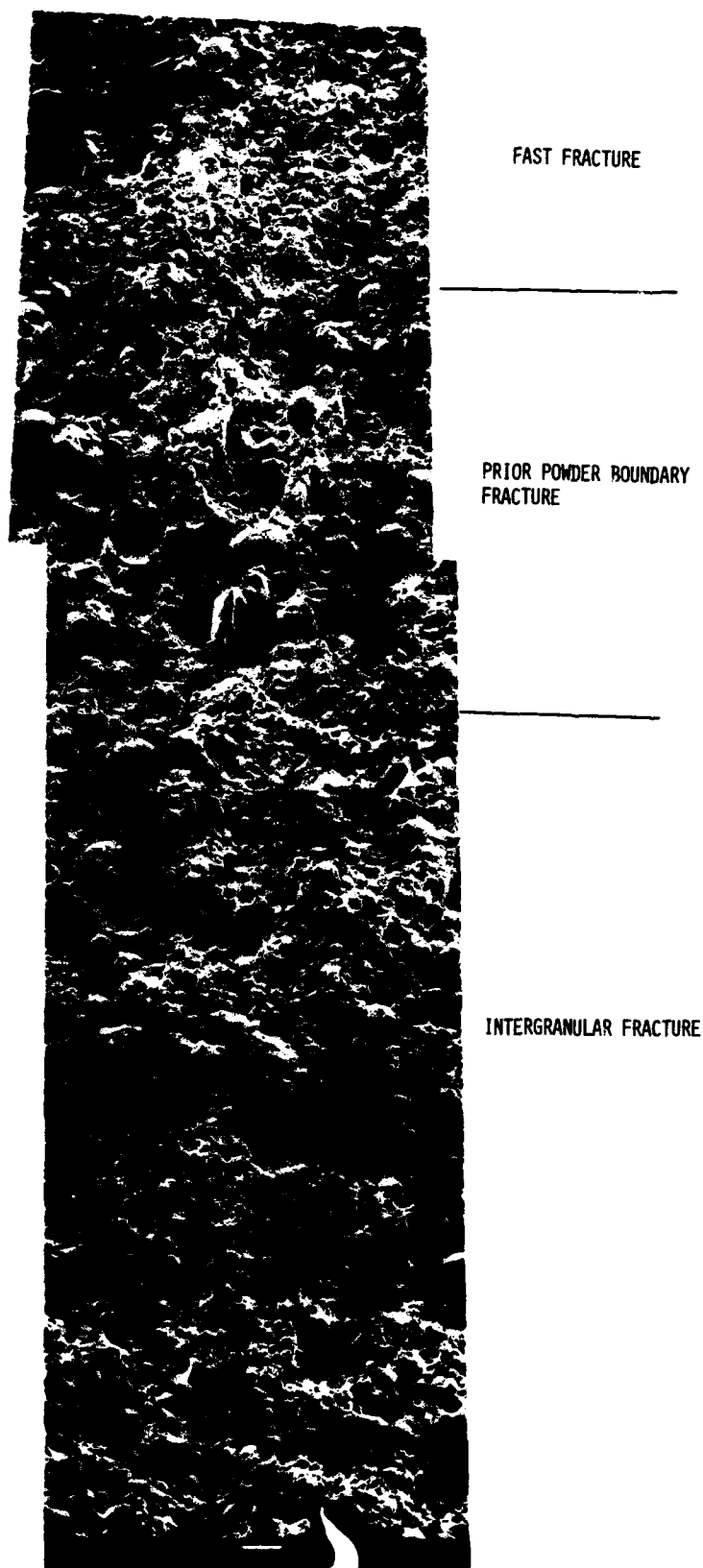


FIGURE (20) TYPICAL FRACTOGRAPH OF A (R TEST ON PM/HIP LOW C
ASTROLOY TESTED IN AIR AT 700°C.

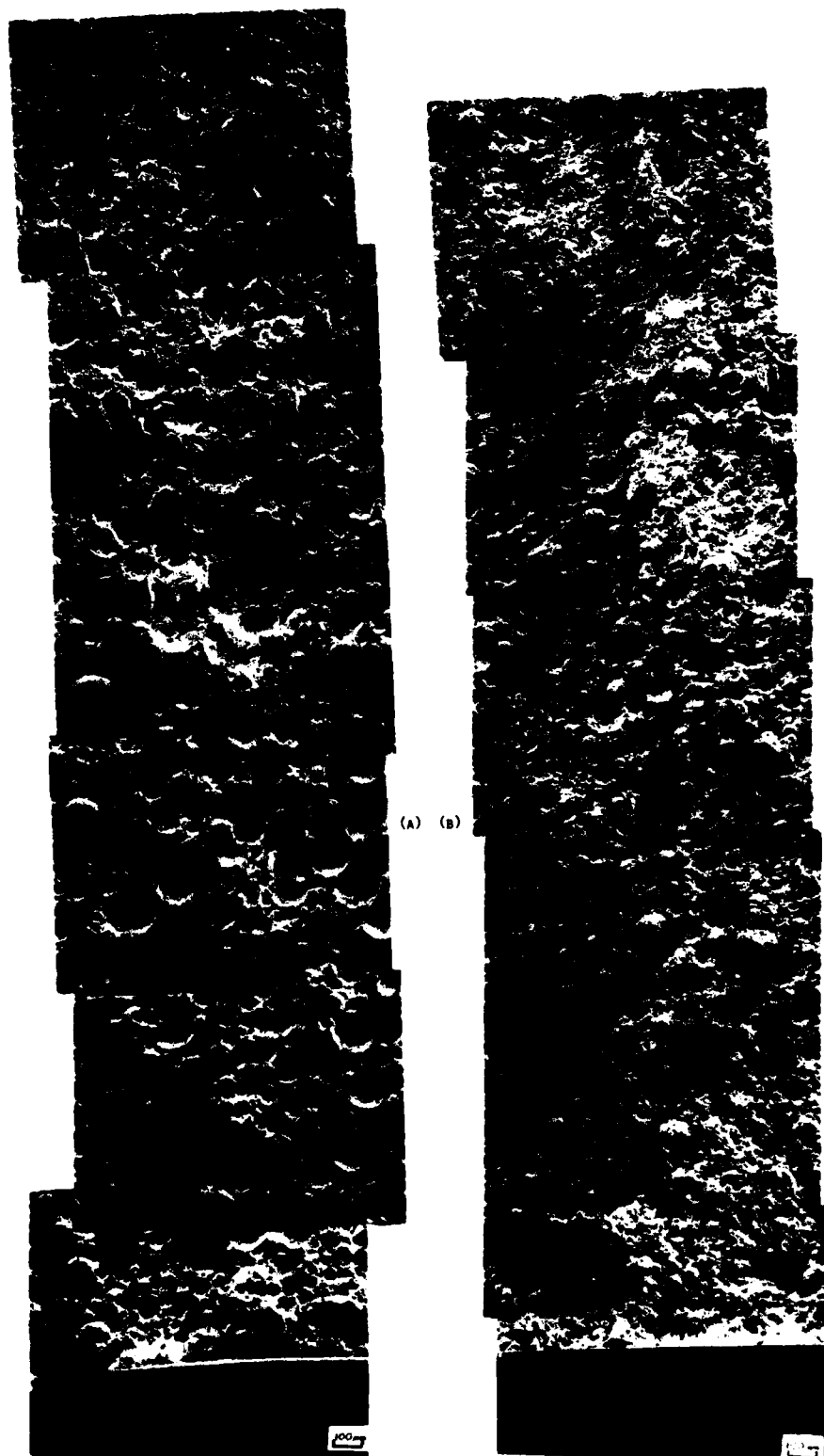


FIGURE (21) FRACTOGRAPHS OF CREEP CRACK FRACTURES IN 99.999% PURE ARGON. (A) PM/HIP LOW C IN-100; (B) PM/HIP RENE-95 (120 MESH POWDER)

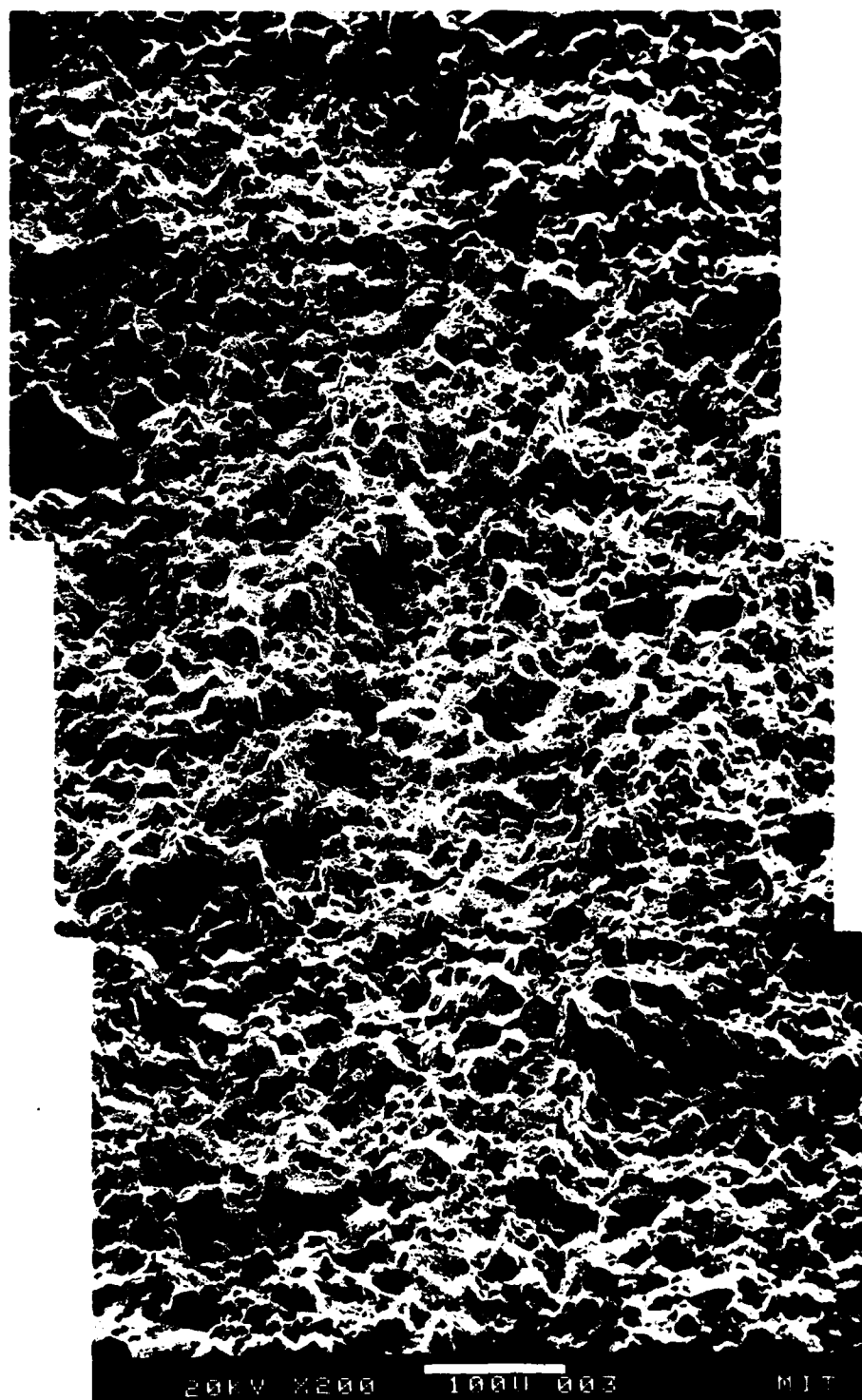


FIGURE (22) Fractograph of a CCGR specimen tested in air at 704°C.
(PM/HIP RENE-95 (120 mesh powder))

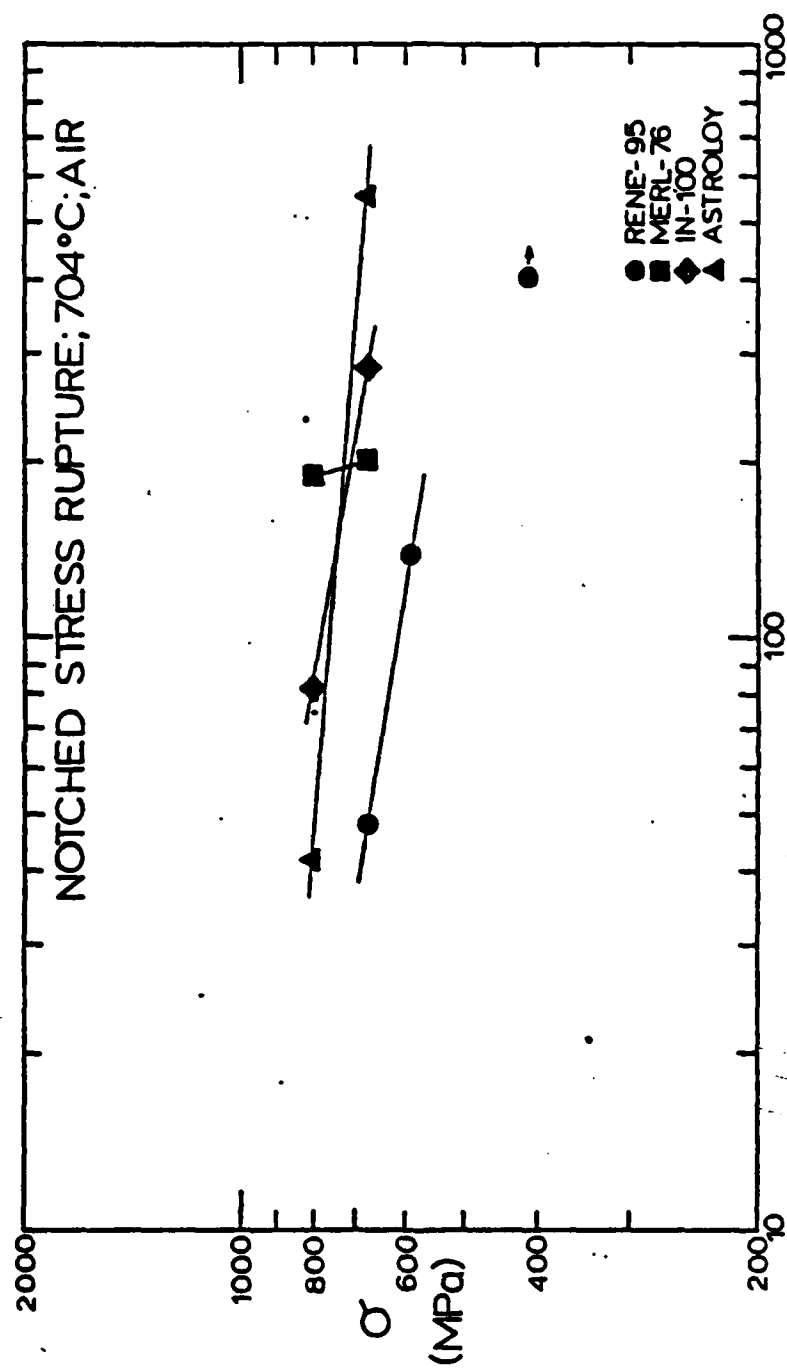


FIGURE (23) Notched stress rupture results in air at 704°C for four PH/NIP Nickel-Base Superalloys.

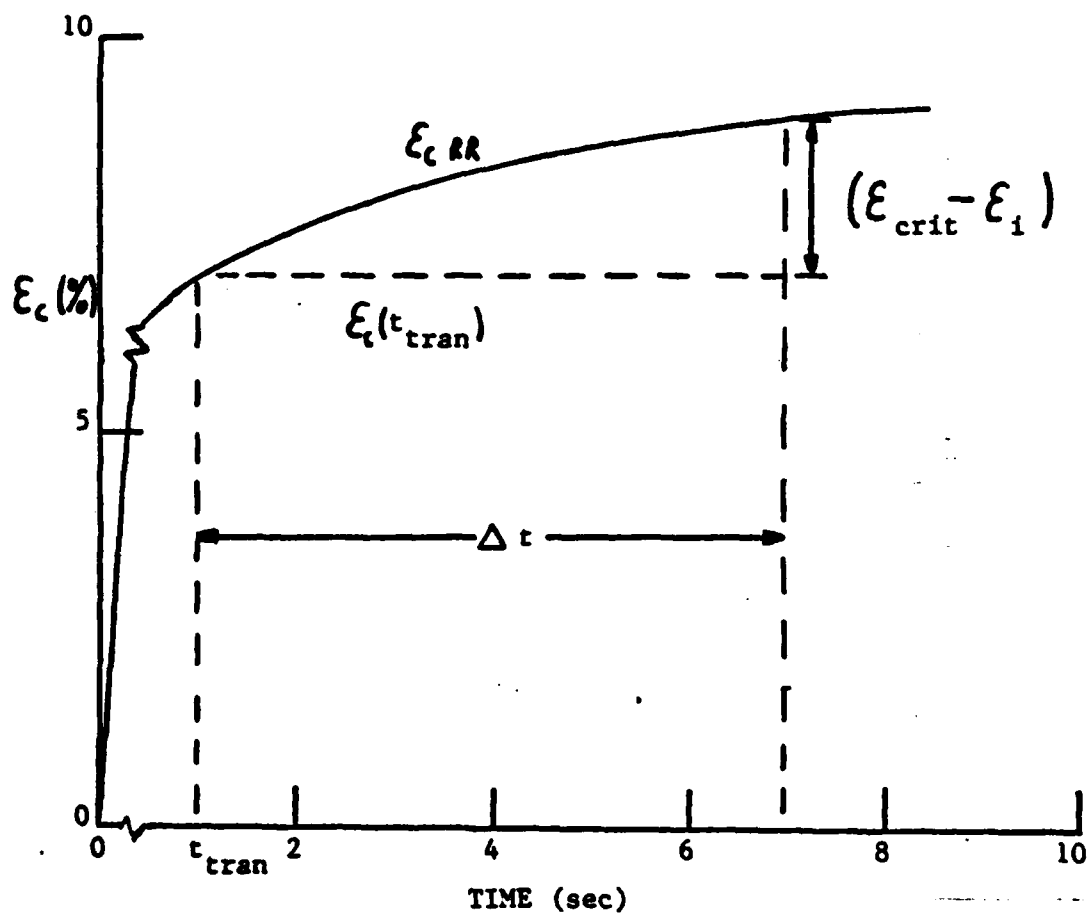


FIGURE (24) Schematic representation of the time for a crack advance in CCG, Δt .

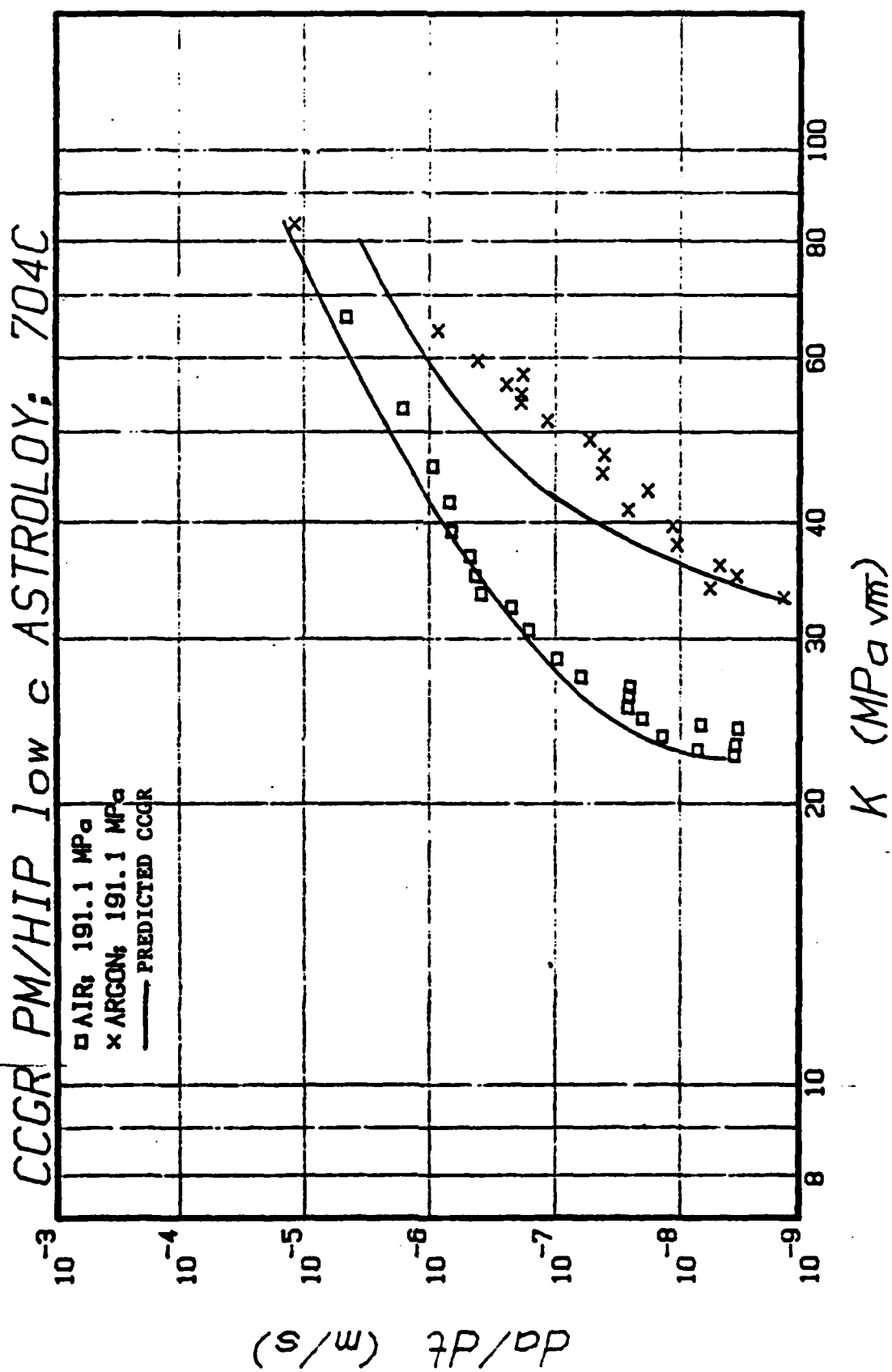


FIGURE (25) Predicted CCGR for PM/HIP low C ASTROLOY test in air and in argon at 704°C.

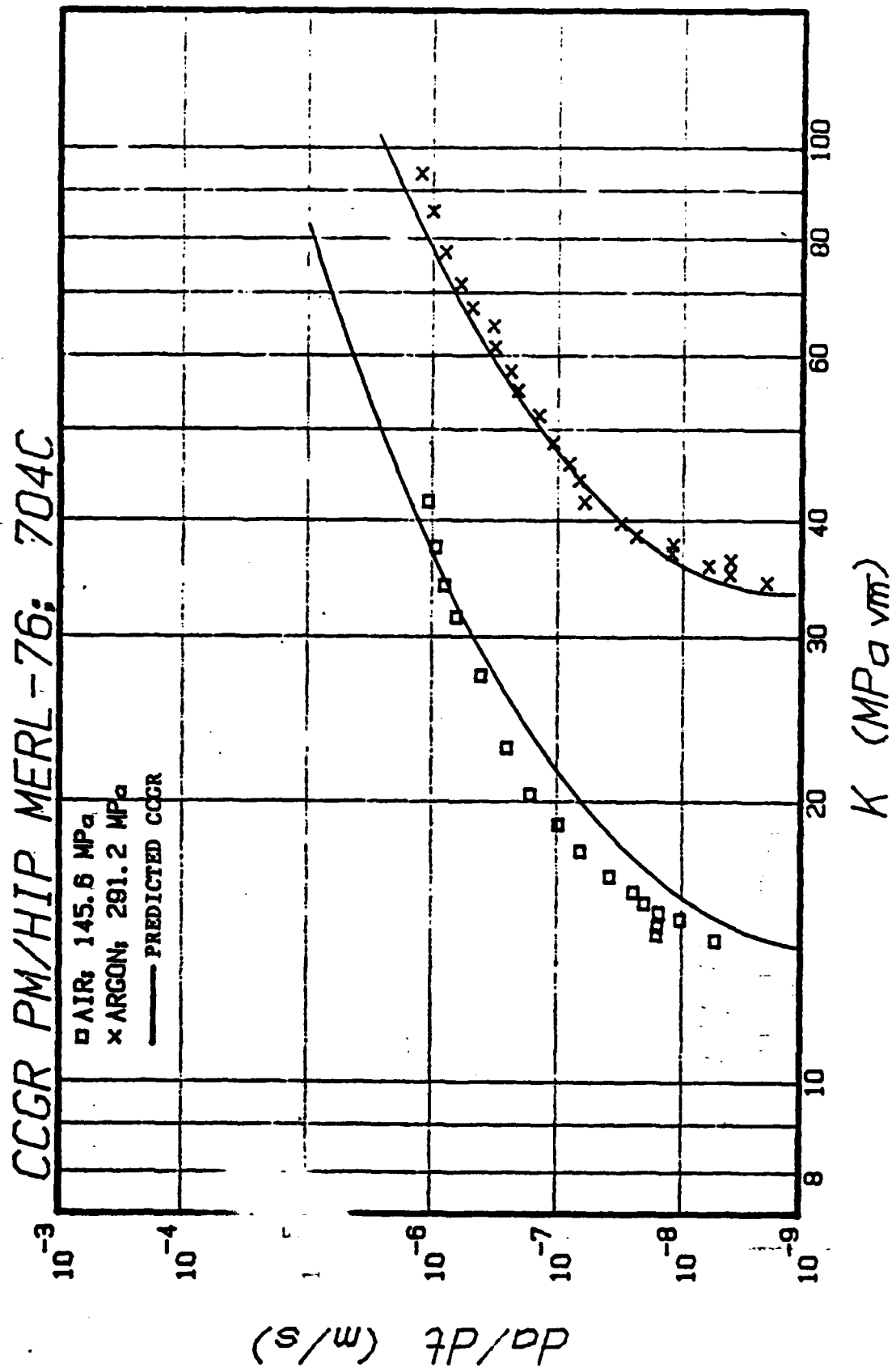


FIGURE (26). Predicted CCGR for PM/HIP MERL-76 tested in air and in argon at 704°C.

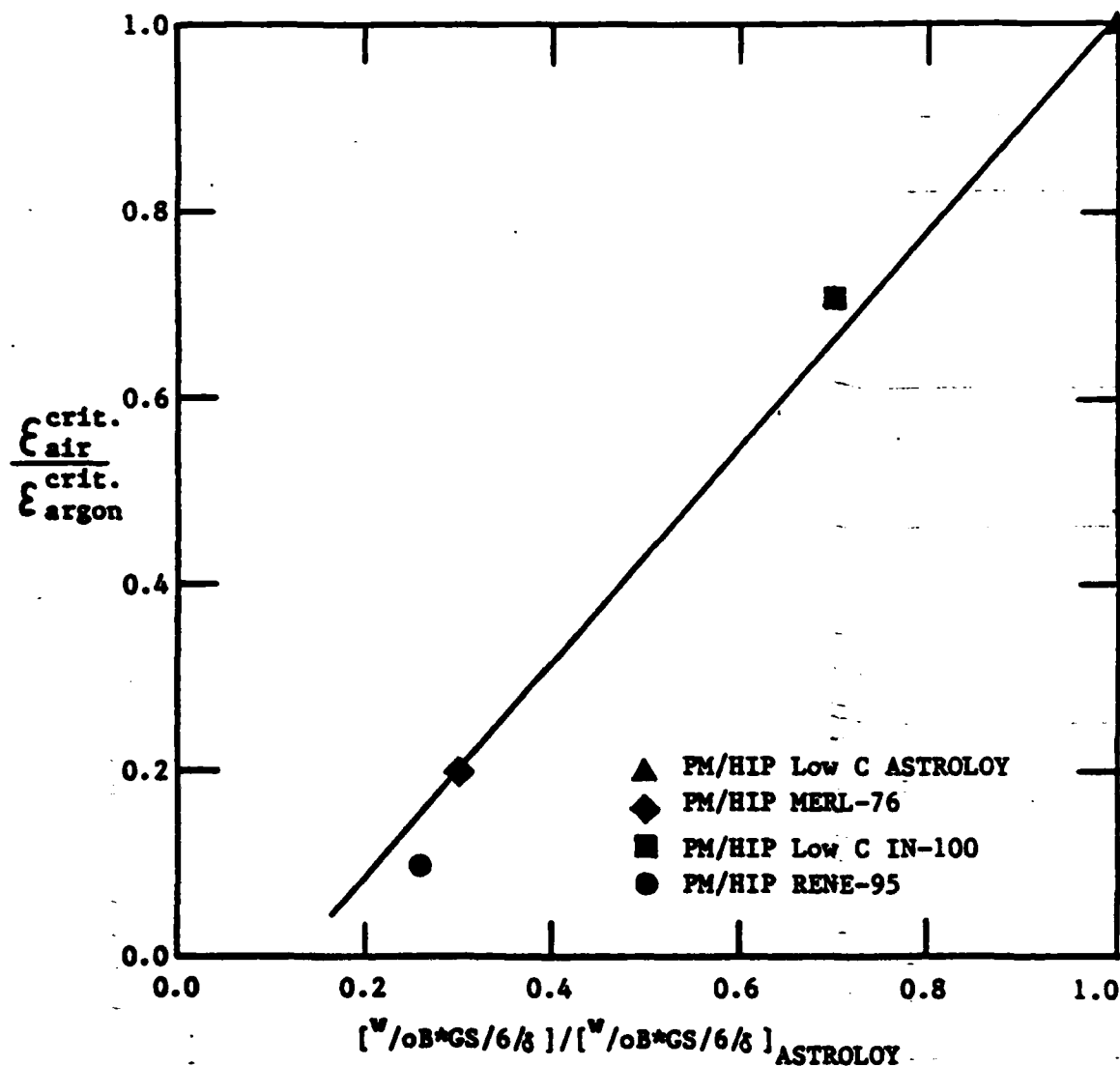
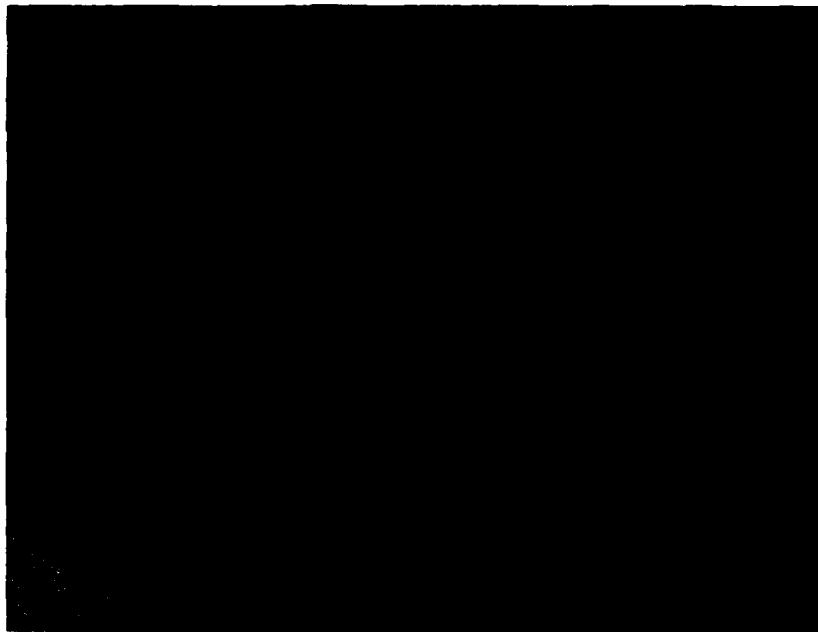
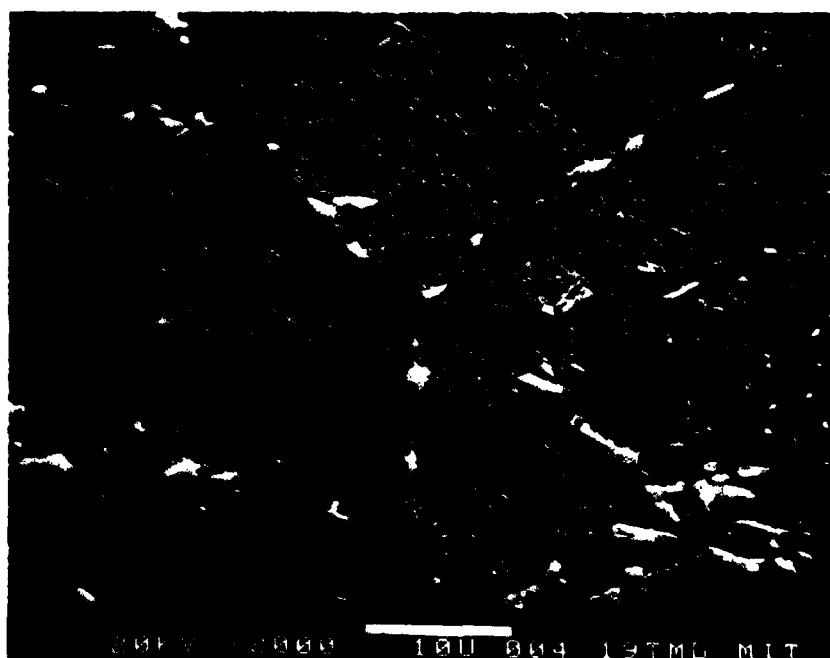
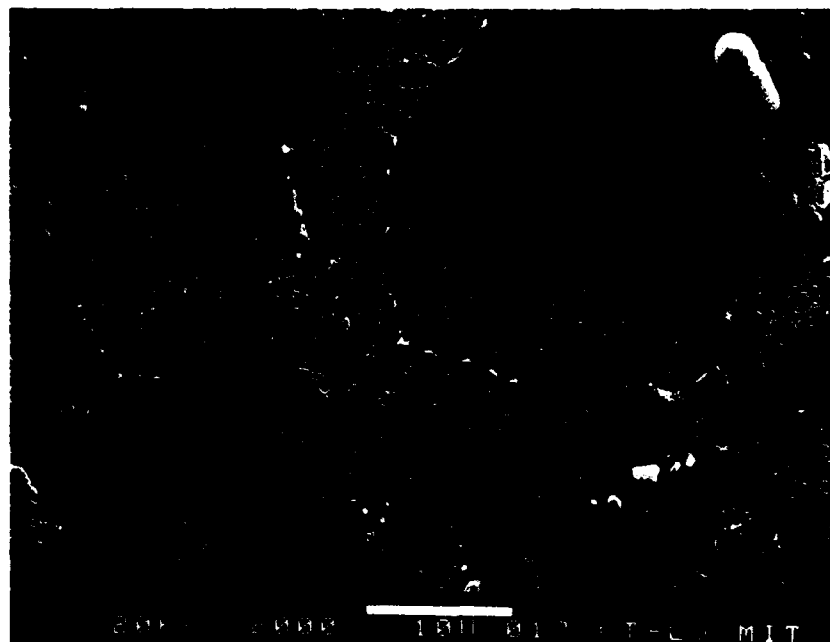


FIGURE (27) Ratio of the critical strain in air to the critical strain in argon versus the ratio of the grain boundary concentration of boron in the alloy to that in ASTROLOY. (δ =Grain Boundary Thickness, assumed to be a constant for all the alloys; GS =Grain Diameter). Assuming the boron in the bulk segregated to the grain boundaries the amount of boron will form a zone 17 mono-layers thick in PM/HIP Low C ASTROLOY.



b)

FIGURE (28) Optical micrographs of the rolling plane of:
a) 2219-T851; and b) 2219-Tmod (Kehler's
etch.)



b)

FIGURE (29) SEM micrographs of the rolling plane of:
a) 2219-T851; b) 2219-Tmod (Kehler's
etch.)

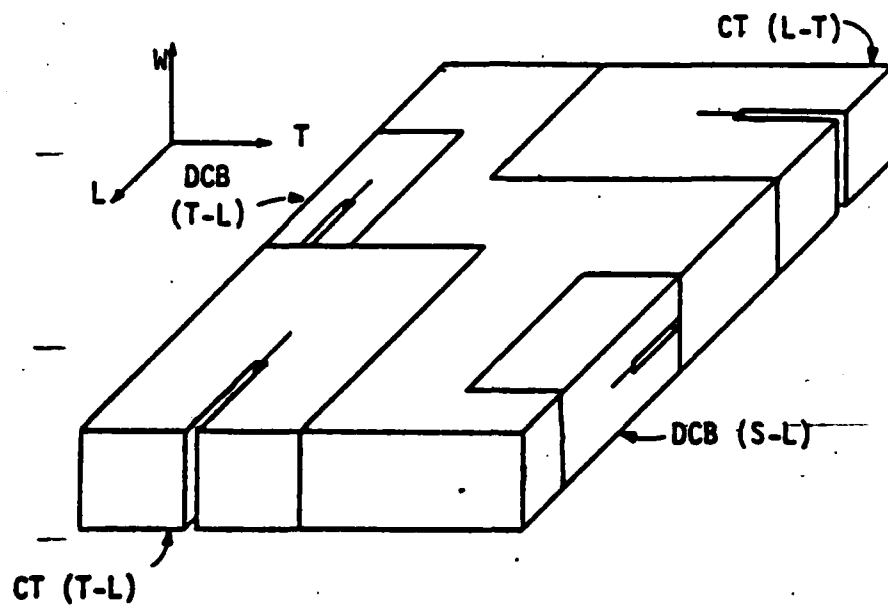


FIGURE (30): Orientations of the CT and the DCB specimens

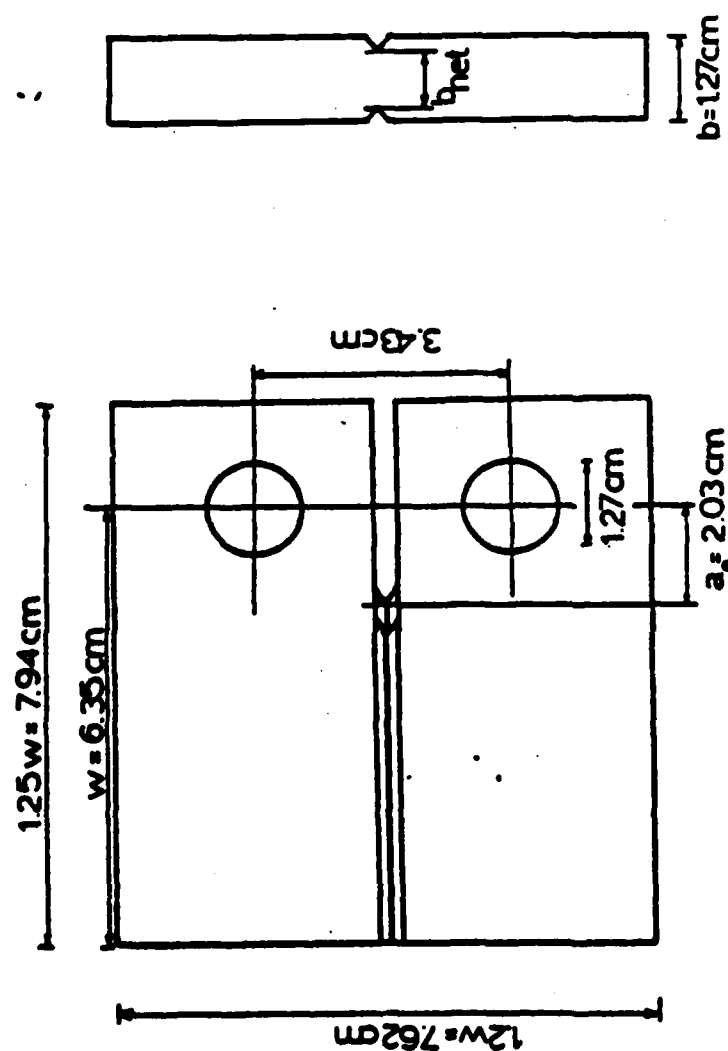
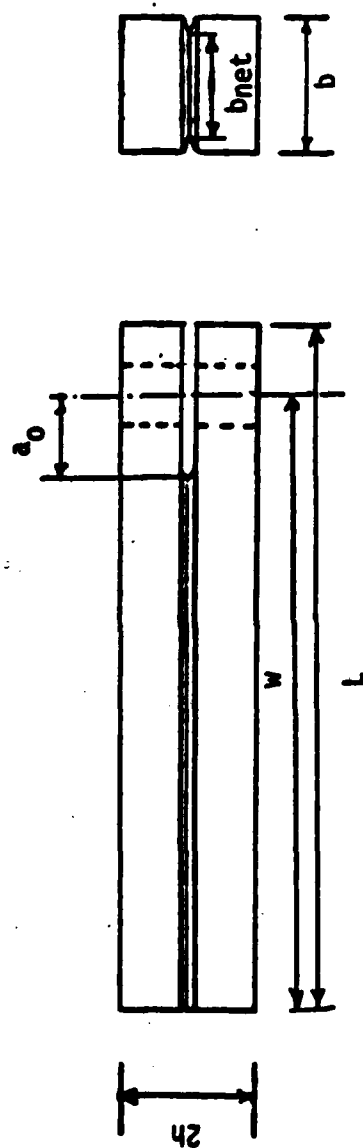


FIGURE (31) CT specimens used for load-controlled crack growth tests



$w=5.72$ cm $b = 1.27$ cm
 $L=6.35$ cm $b_{net} = .76$ cm
 $2h=1.27$ cm

FIGURE (32). DCB specimens used for constant-opening-displacement tests

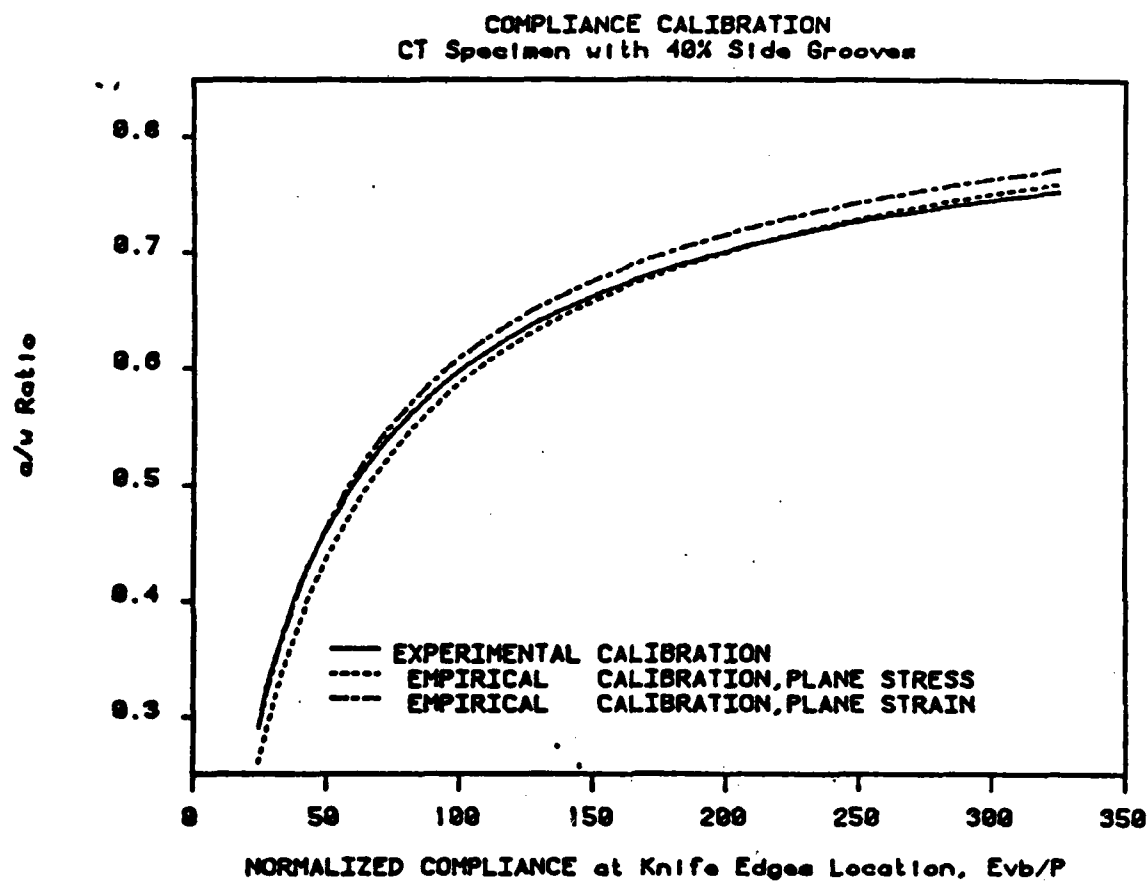


FIGURE (33) Comparison between the experimental compliance for 40% side-grooved CT specimens and the compliance reported in references (89); and (90); for side-grooved CT specimens under plane stress and plane strain conditions

2219-T851 (175 C, air) (T-L) Orientation
CT Specimen with 40% Side Grooves

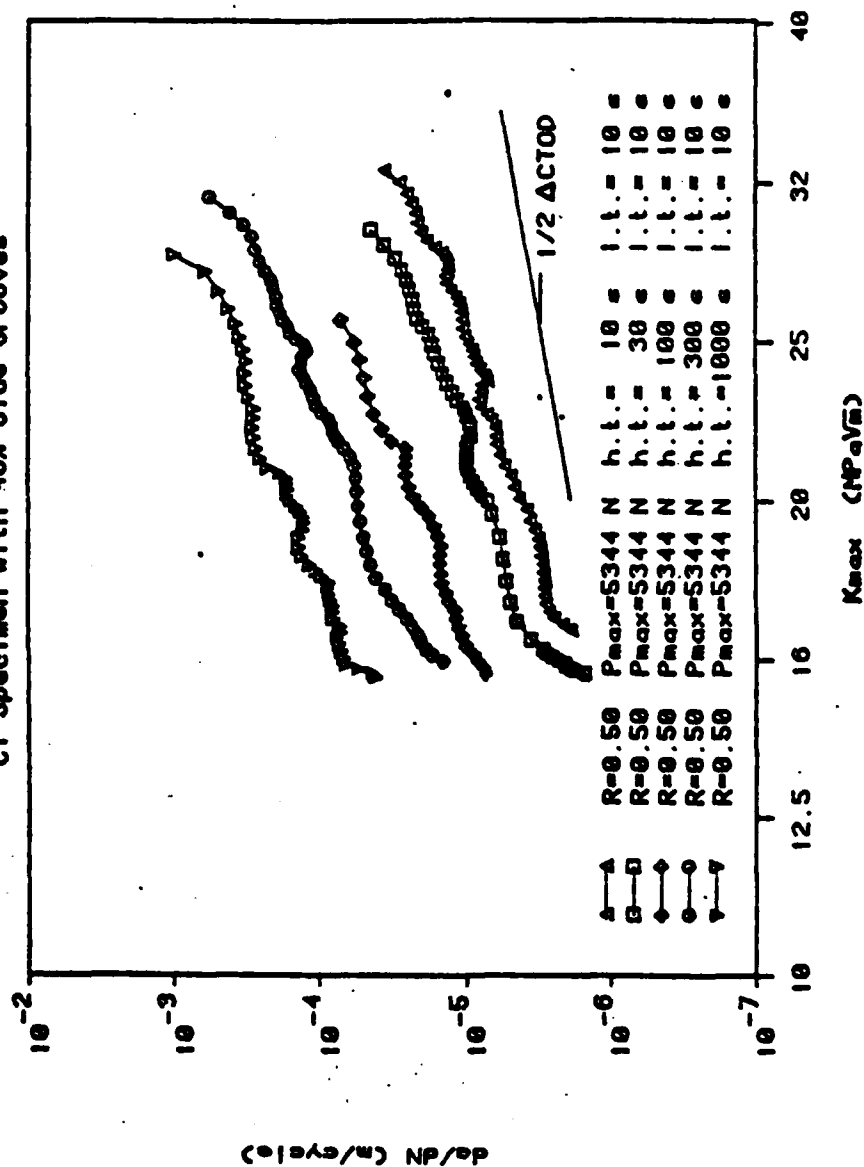


FIGURE (34)
Effect of the hold time at maximum load on
da/dN (note: Kmax = maximum stress intensity
factor, h.t. = hold time, l.t. = loading (or
unloading) time)

2219-T851 (175 C, air) (T-L) Orientation
CT Specimen with 40X Side Grooves

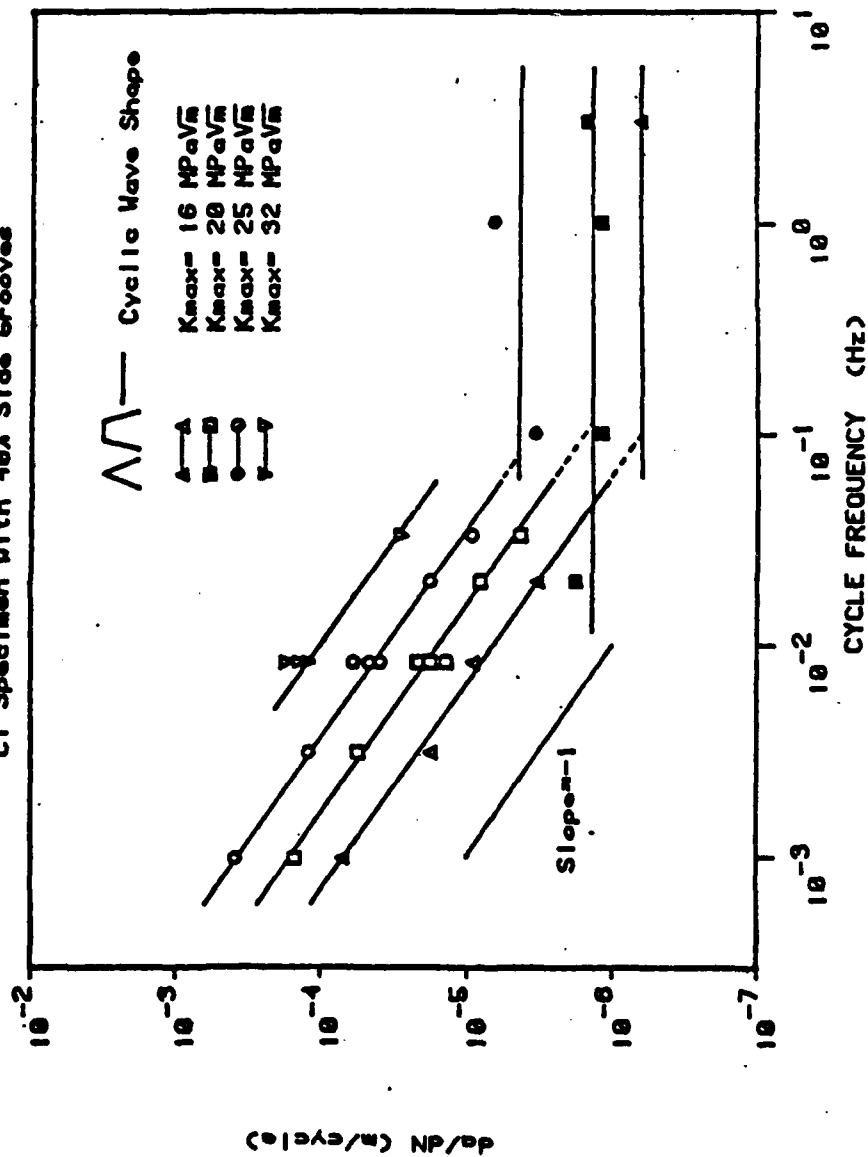


FIGURE (35) Effect of the cycle frequency and the hold time on da/dN

2219-T851 (175 C, air) (T-L) Orientation
CT Specimen with 40% Side Grooves

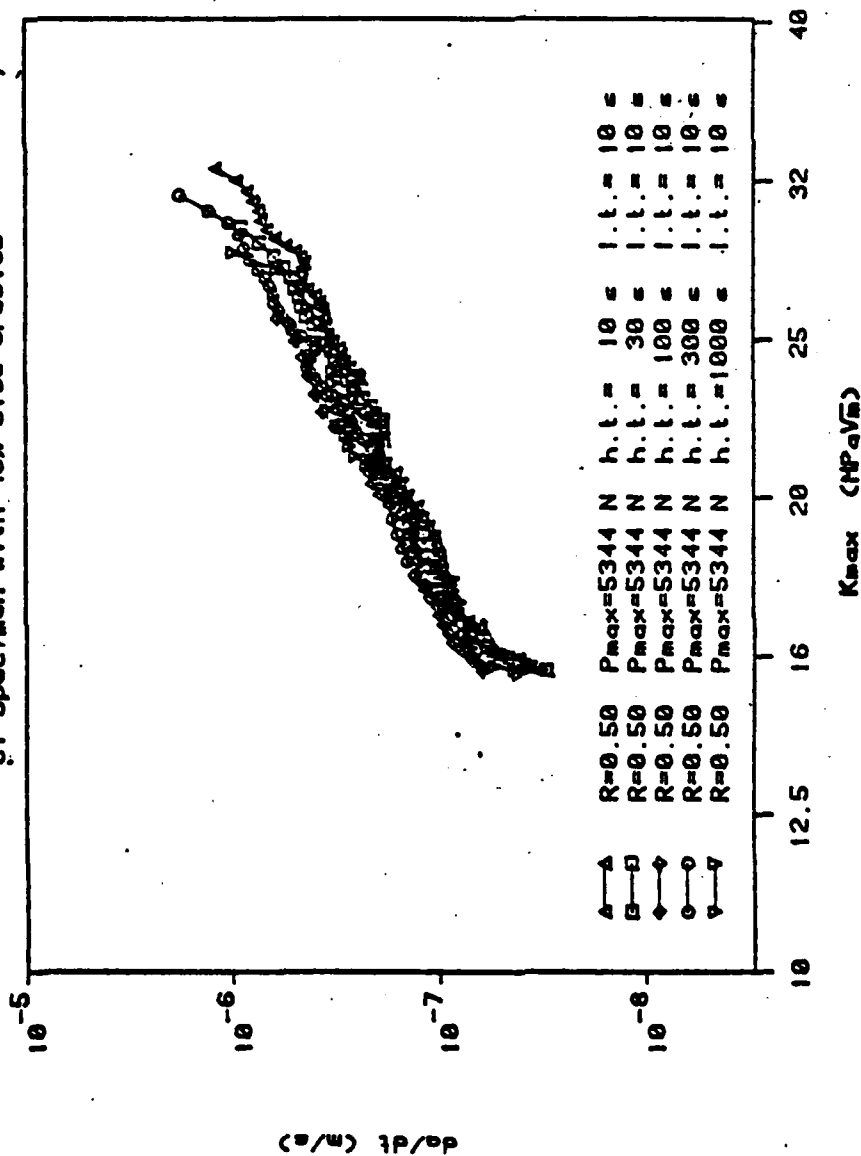


FIGURE (36) Crack growth rates per unit time for tests with hold times ranging from 10 s to 1000 s

2219-T651 (175 C, air) (T-L) Orientation
CT Specimen with 40% Side Grooves

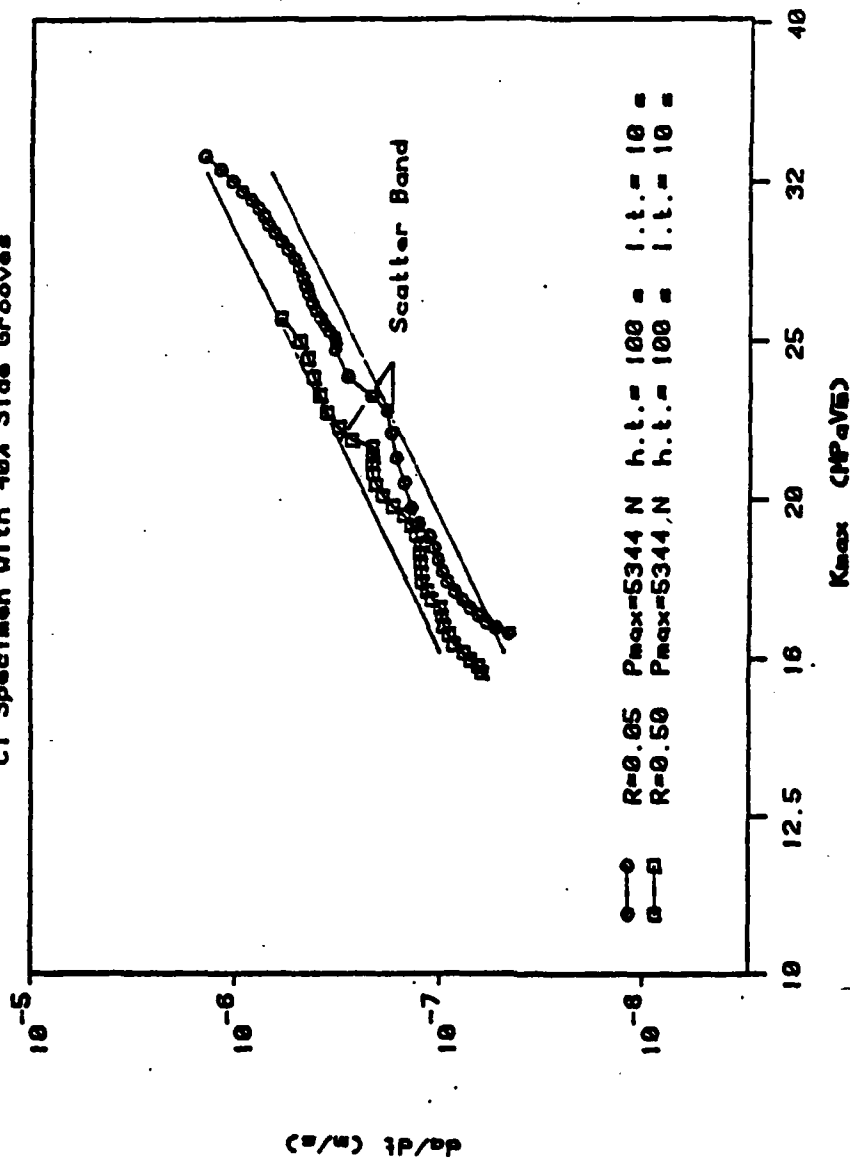


FIGURE (37) Effect of the R ratio on da/dN

2219-T851 (175 C, air) (Y-L) Orientation
CT Specimen with 40X Side Grooves

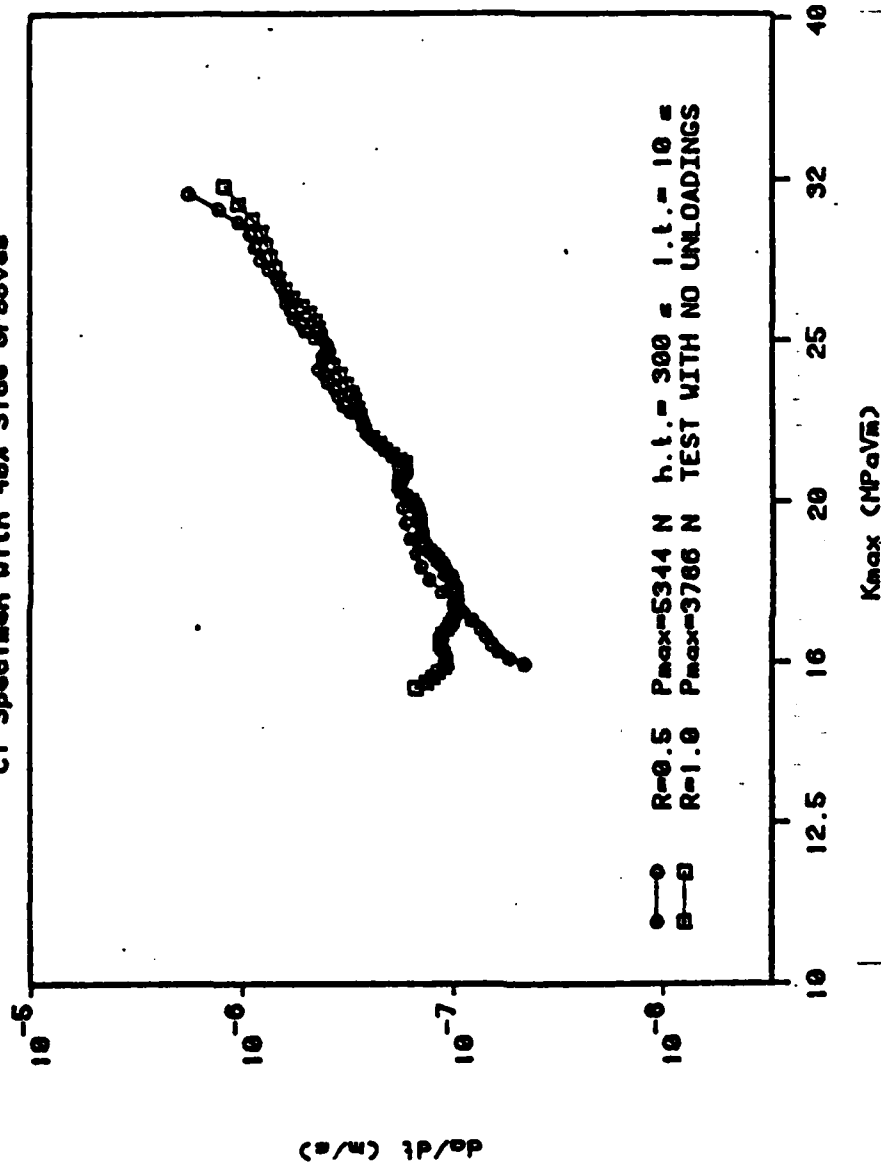


FIGURE (38) Comparison between the crack growth rates per unit time for tests with and without unloadings

2219-T651. (175 C, air). (T-L) Orientation.
CT Specimen with 40X Side Grooves.

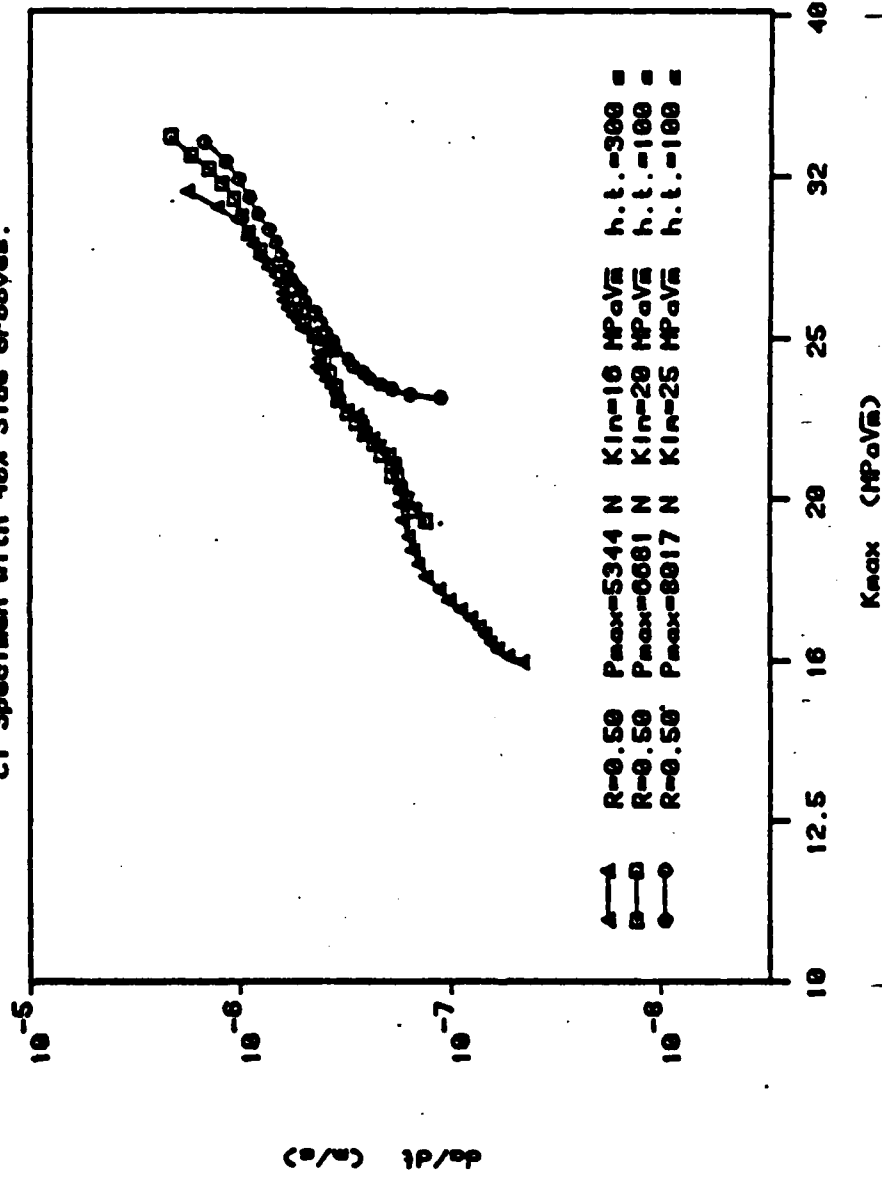


FIGURE (39) Effect of the initial stress intensity factor on da/dt

2219-1061 (175 C, air) (T-L) Orientation
CT Specimen with 40X Side Grooves

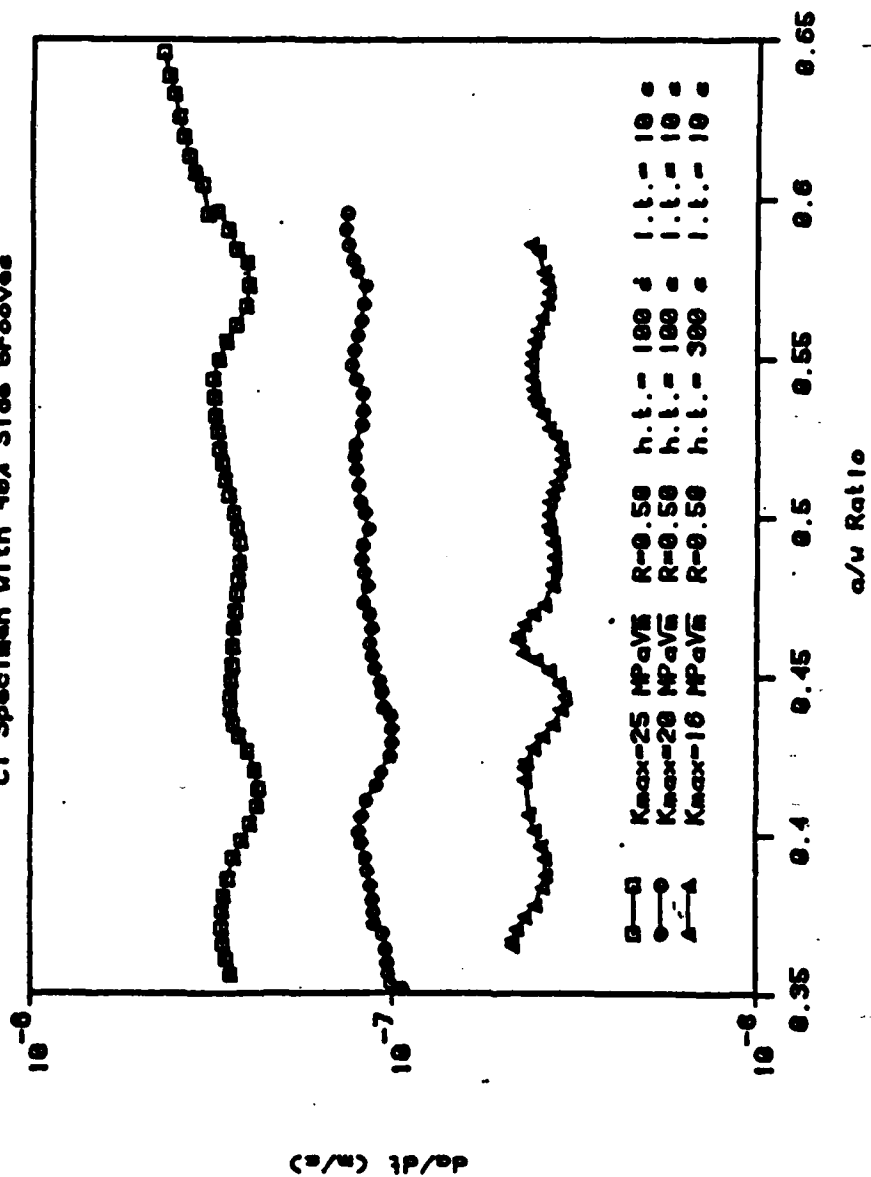


FIGURE (40) Variations of da/dt as a function of a/w for constant-K_{max} tests

EFFECT of MICROSTRUCTURE on CREEP CRACK GROWTH (175 C, air) (T-L) Orientation

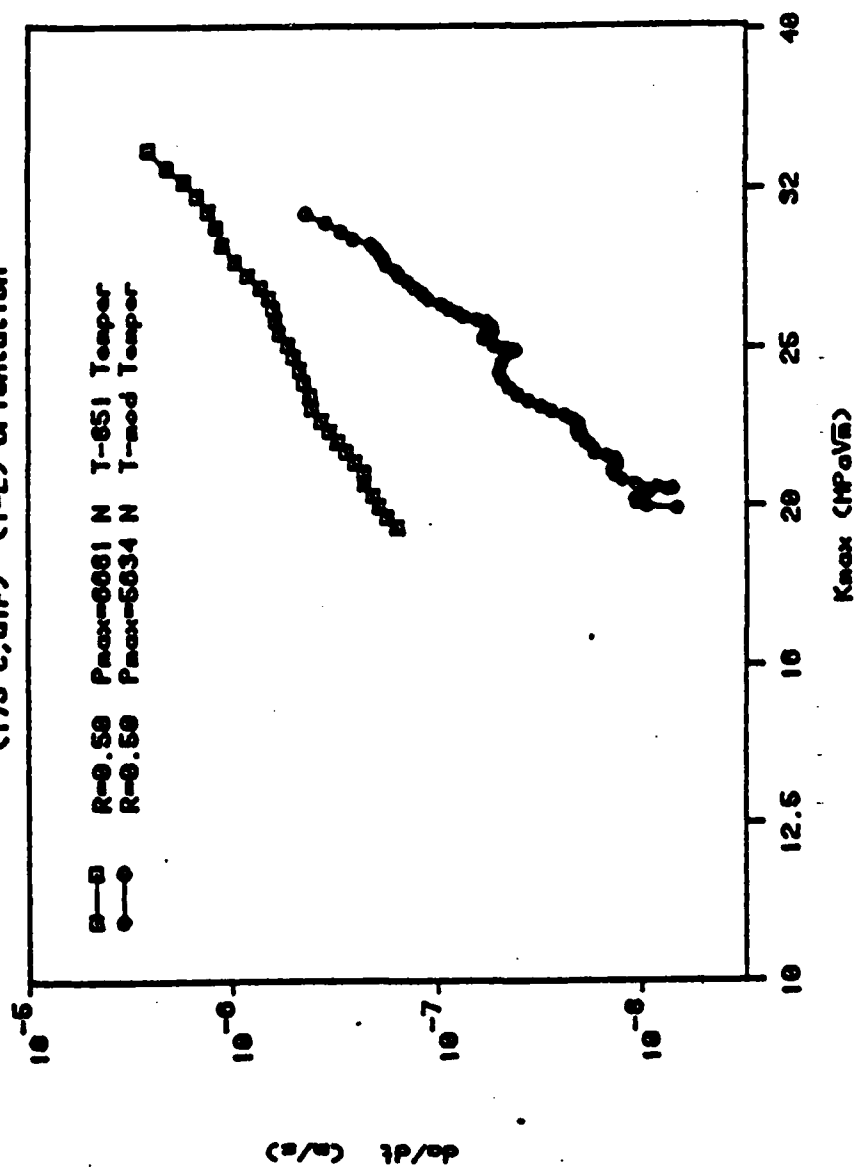


FIGURE (41) Comparison between the creep crack growth rates in 2219-T851 and 2219-Tmod

$K_{max}=16 \text{ MPa}\sqrt{\text{m}}$ $da/dt=4 \times 10^{-8} \text{ m/s}$

CRACK PROPAGATION →

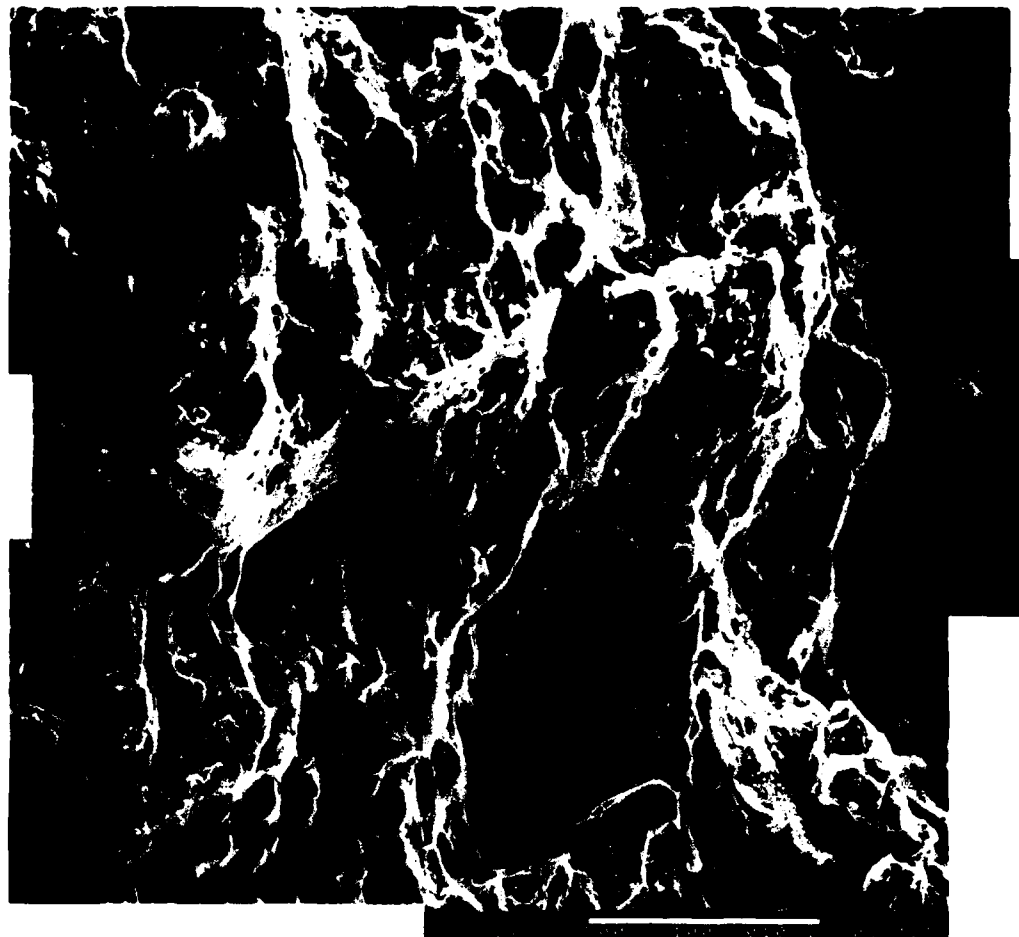


100 μm

FIGURE (42) : MONTAGE OF SEM FRACTOGRAPHS TAKEN FROM A 2219-T851 (T-L) CT
SPECIMEN : $K_{max}=16 \text{ MPa}\sqrt{\text{m}}$, $da/dt=4 \times 10^{-8} \text{ m/s}$, $T=175 \text{ }^{\circ}\text{C}$.

$$K_{\max}=20 \text{ MPa}\sqrt{\text{m}} \quad da/dt=1 \times 10^{-8} \text{ m/s}$$

CRACK PROPAGATION ↑



100 μm

FIGURE (43) .1. :MONTAGE OF SEM FRACTOGRAPHS TAKEN FROM A 2219-TMOD (T-L) CT
SPECIMEN : $K_{\max}=20 \text{ MPa}\sqrt{\text{m}}$, $da/dt=1 \times 10^{-8} \text{ m/s}$, $T=175 \text{ }^{\circ}\text{C}$.

$$K_{\max}=25 \text{ MPa}\sqrt{\text{m}} \quad da/dt=3 \times 10^{-7} \text{ m/s}$$

CRACK PROPAGATION ↑



FIGURE (44) : MONTAGE OF SEM FRACTOGRAPHS TAKEN FROM A 2219-T851 (T-L) CT
SPECIMEN : $K_{\max}=25 \text{ MPa}\sqrt{\text{m}}$, $da/dt=3 \times 10^{-7} \text{ m/s}$, $T=175 \text{ }^{\circ}\text{C}$.

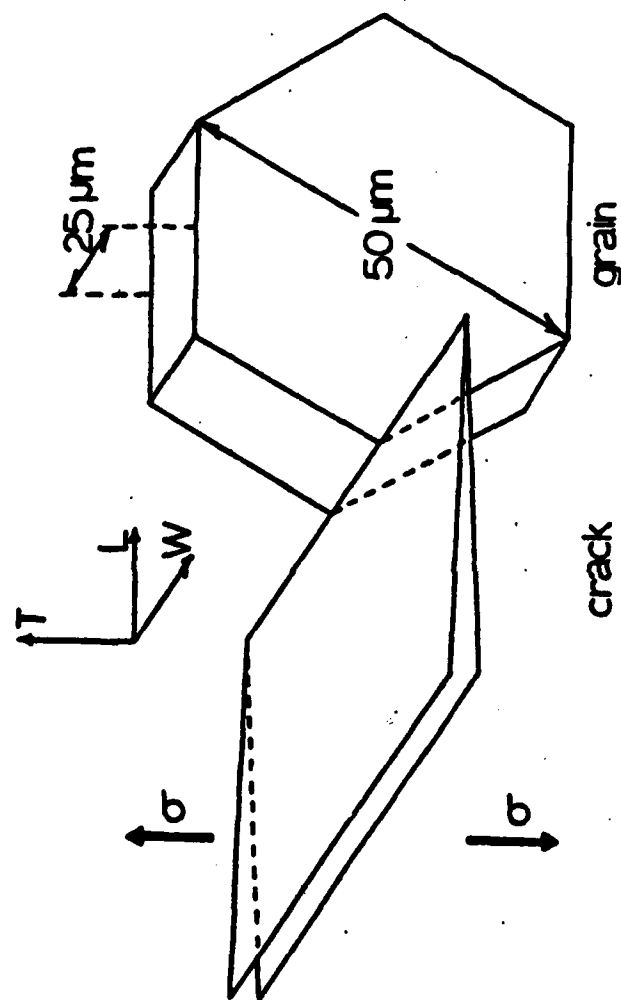


FIGURE (45) Schematic showing the grain orientation with respect to the crack plane in the (T-L) orientation

CRACK PROPAGATION ↑



FIGURE (46) HIGH MAGNIFICATION FRACTOGRAPH TAKEN FROM A 2219-T851 (T-L)
CT SPECIMEN SHOWING EVIDENCE OF GRAIN-BOUNDARY CAVITATION
(K_{MAX} = 20 MPa√m, T = 175 °C) .

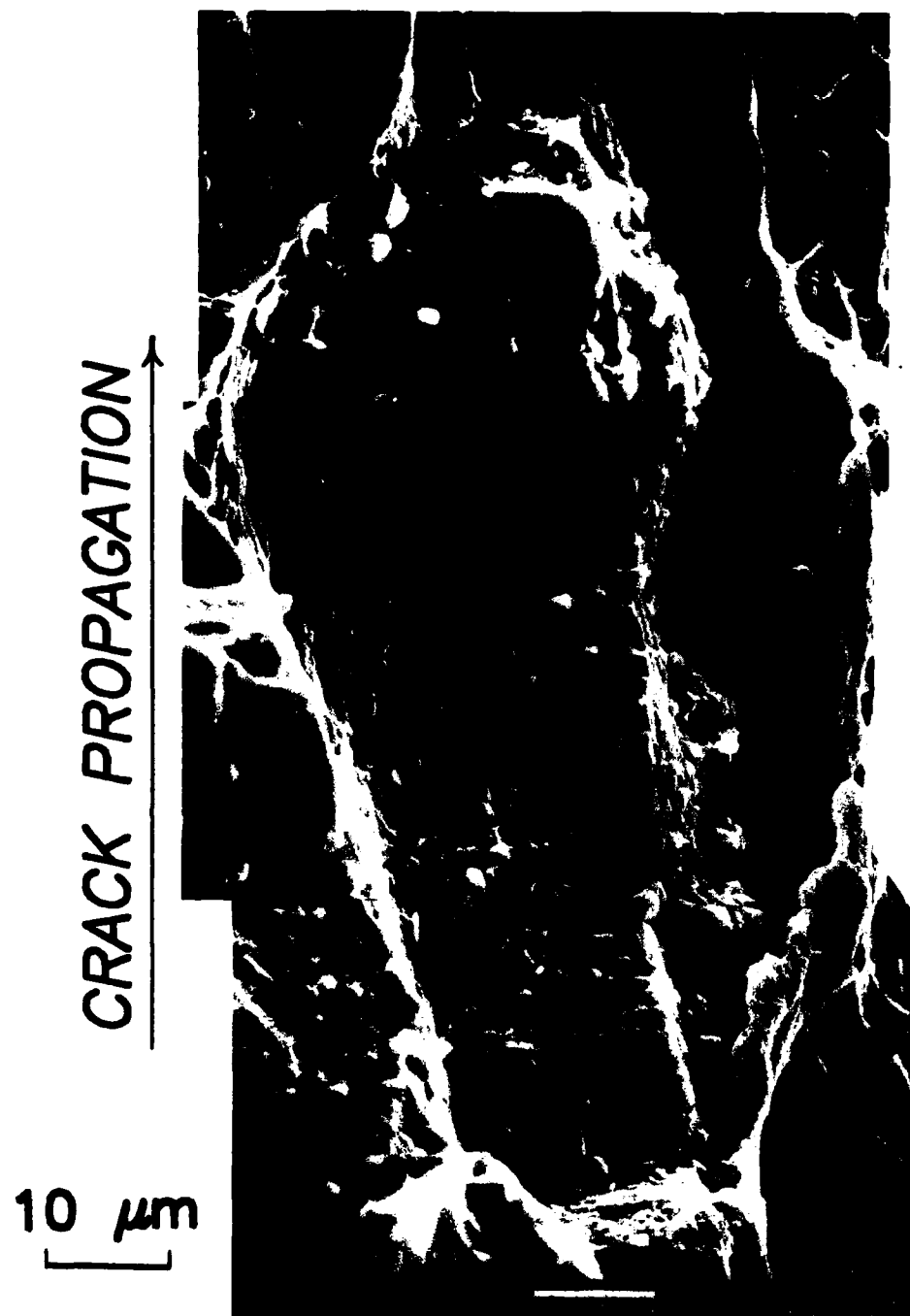


FIGURE (47) : HIGH MAGNIFICATION FRACTOGRAPH TAKEN FROM A 2219-TMOD (T-L)
CT SPECIMEN SHOWING EVIDENCE OF GRAIN-BOUNDARY CAVITATION
($K_{\text{MAX}}=20 \text{ MPa}\sqrt{\text{m}}$, $T=175 \text{ }^{\circ}\text{C}$).

2219-T051. (175 C, air). (I-L) Orientation.
CT Specimen with 40X Side Grooves.

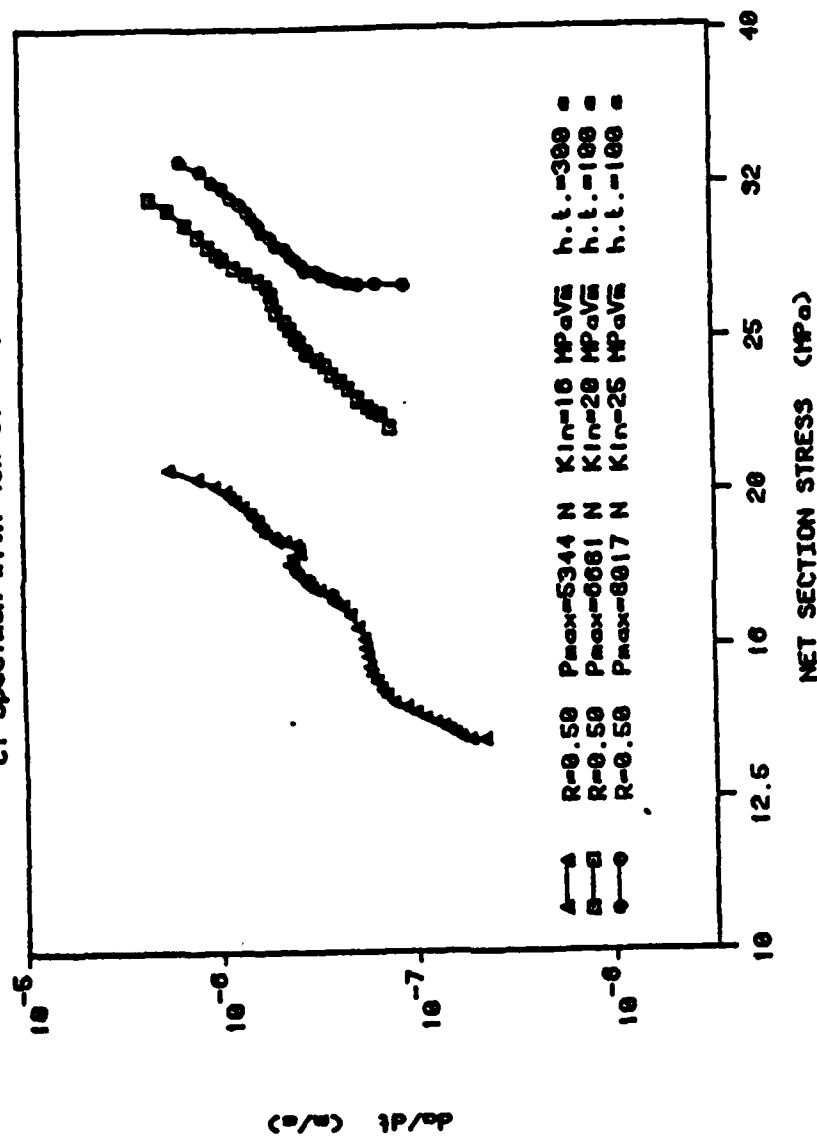


FIGURE (48) da/dt versus σ_{net} for constant- P_{max} tests

2210-T6S1. (176 C, air). (T-L) Orientation.
CT Specimen with 40X Side Groove

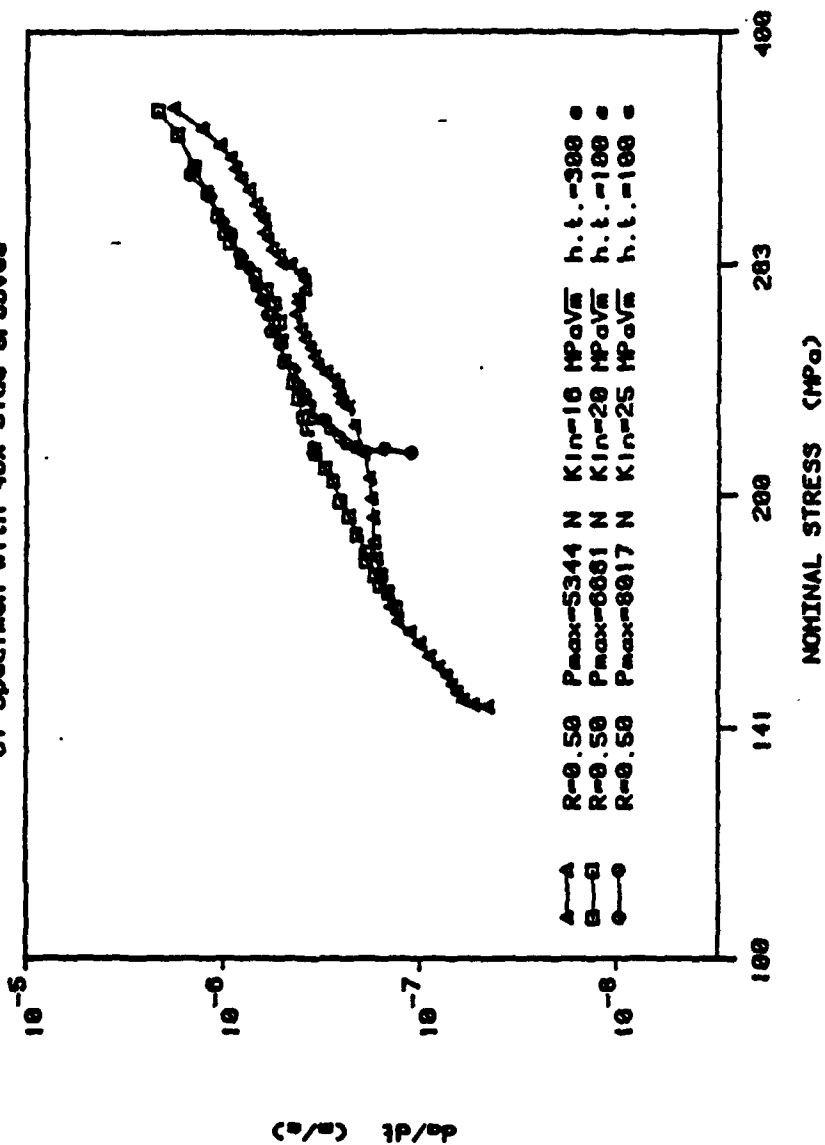


FIGURE (49) da/dt versus σ_{nom} for constant- P_{max} tests

2219-T851. (175 C, air). (T-L) Orientation.
CT Specimen with 40X Side Grooves.

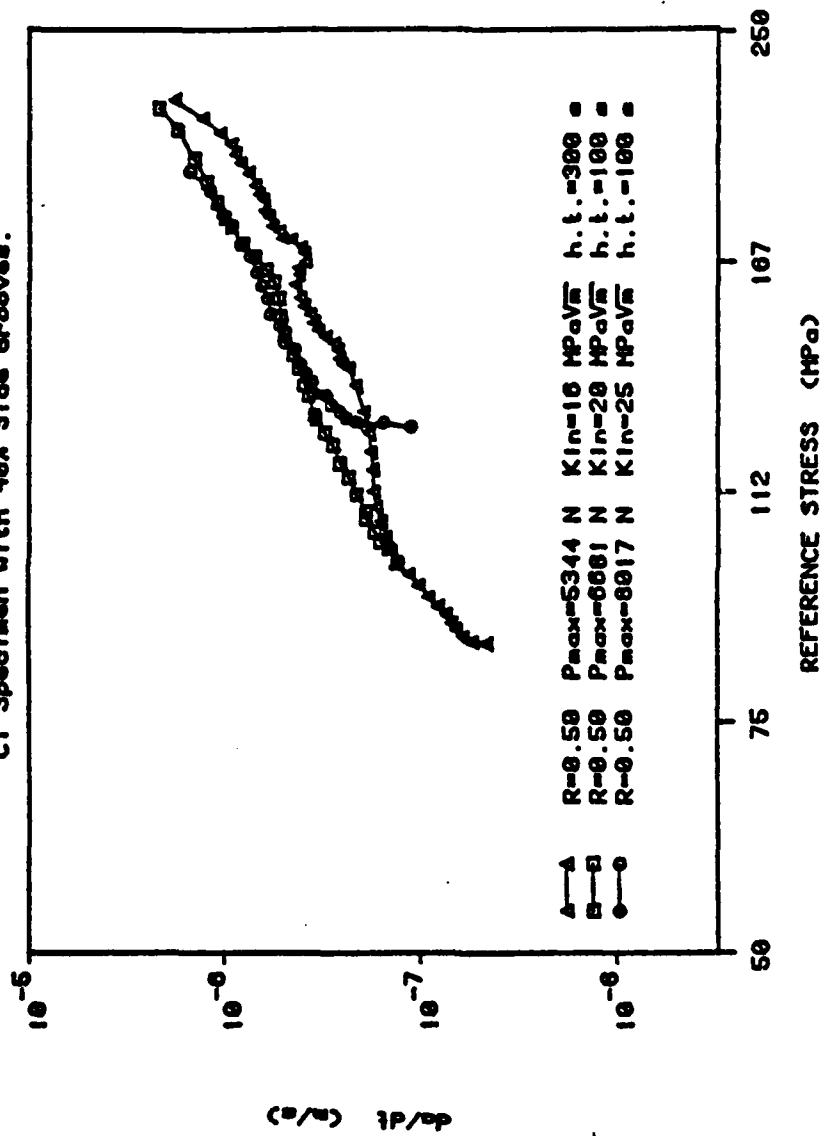


FIGURE (50) da/dt versus σ_{ref} for constant- P_{max} tests

2219-T851. (175 C, air). (T-L) Orientation.
CT Specimen with 40X Side Grooves

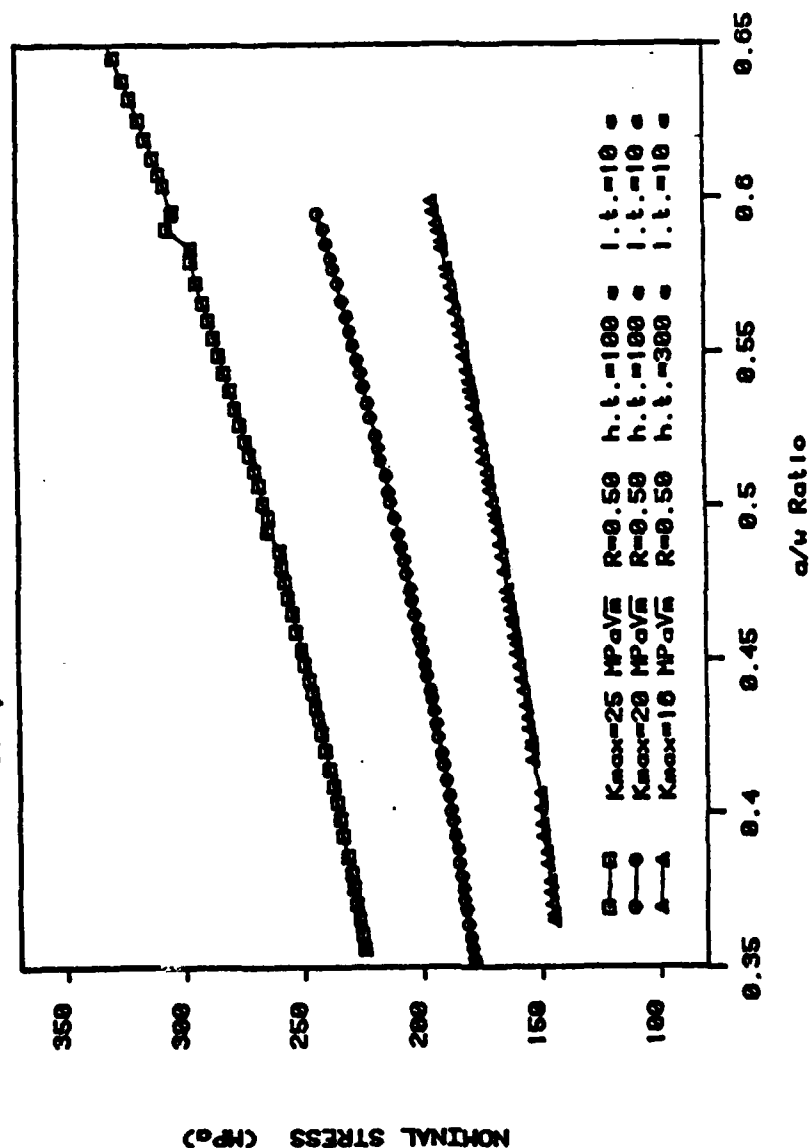


FIGURE (51) Variations of σ_{nom} with a/w for constant- K_{max} tests

2219-T851. (175 C. air). (T-L) Orientation.
CT Specimen with 40X Side Grooves.

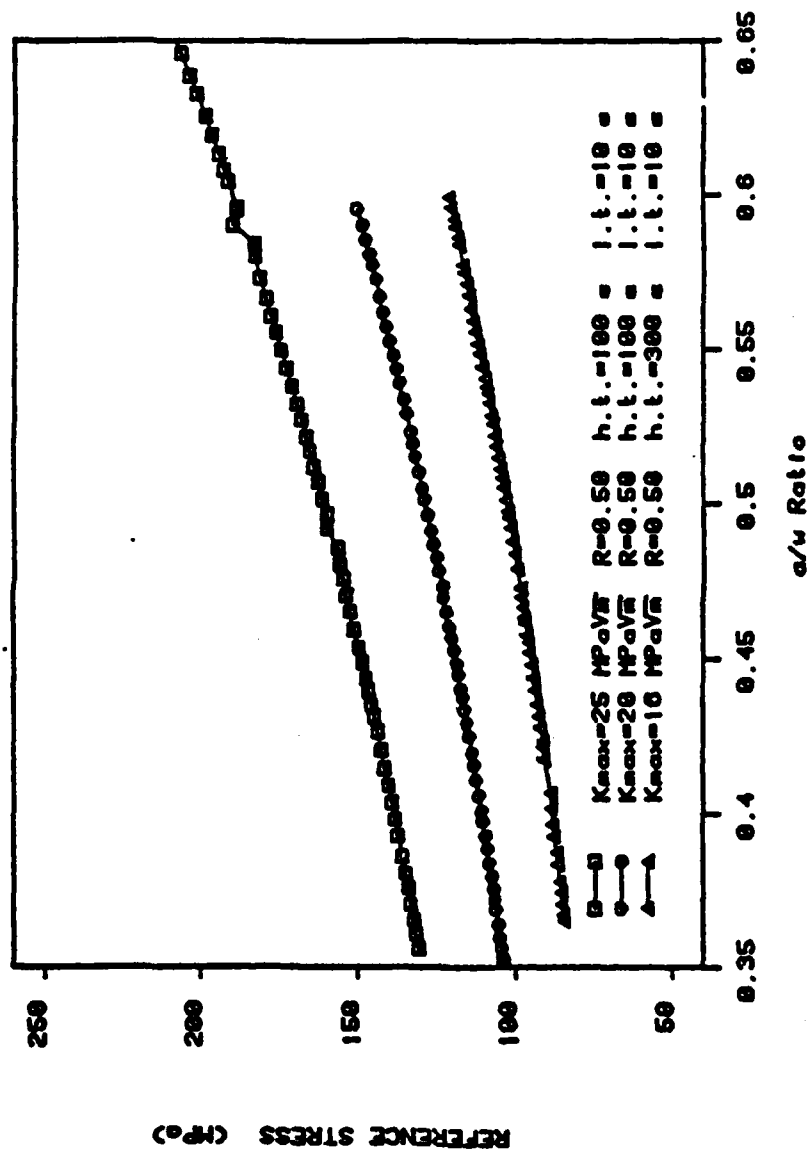


FIGURE (52) Variations of σ_{ref} with a/w for constant- K_{max} tests

2210-T651. (175 C, air). Plane Strain Calculations.
CT Specimen with 40X Side Grooves. (T-L) Orientation.

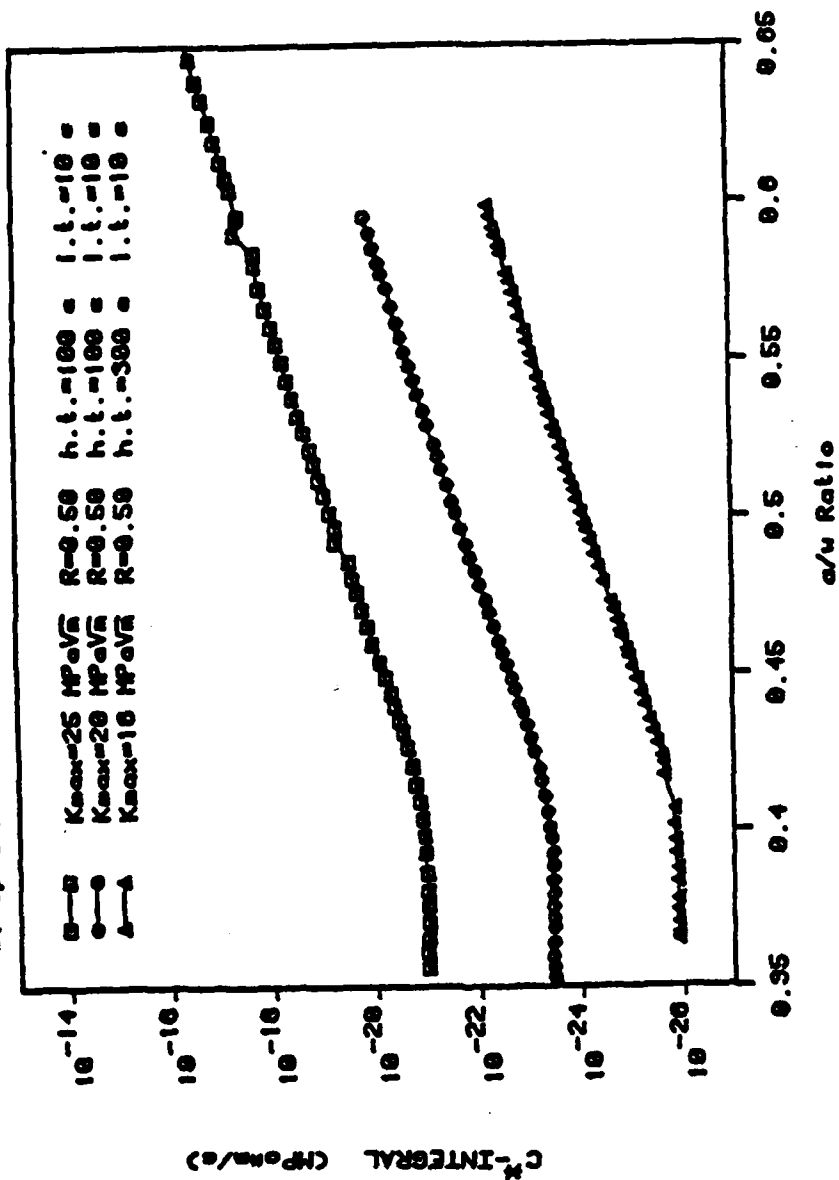


FIGURE (53) Variations of C^* with a/w for constant- K_{max} tests

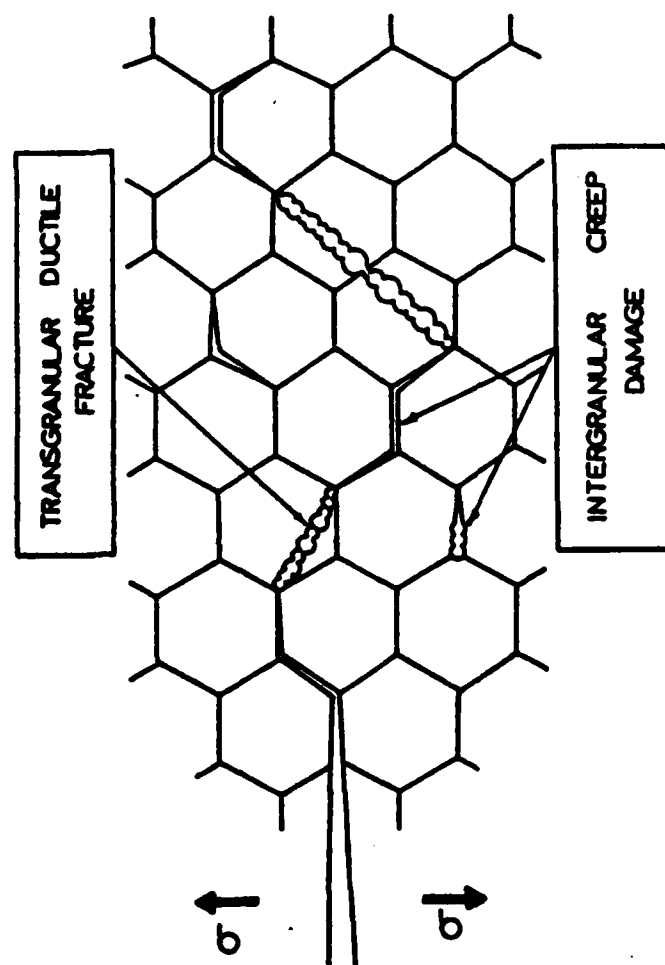


FIGURE (54) Schematic representation of the mechanism of creep crack growth in 2219 aluminum alloy

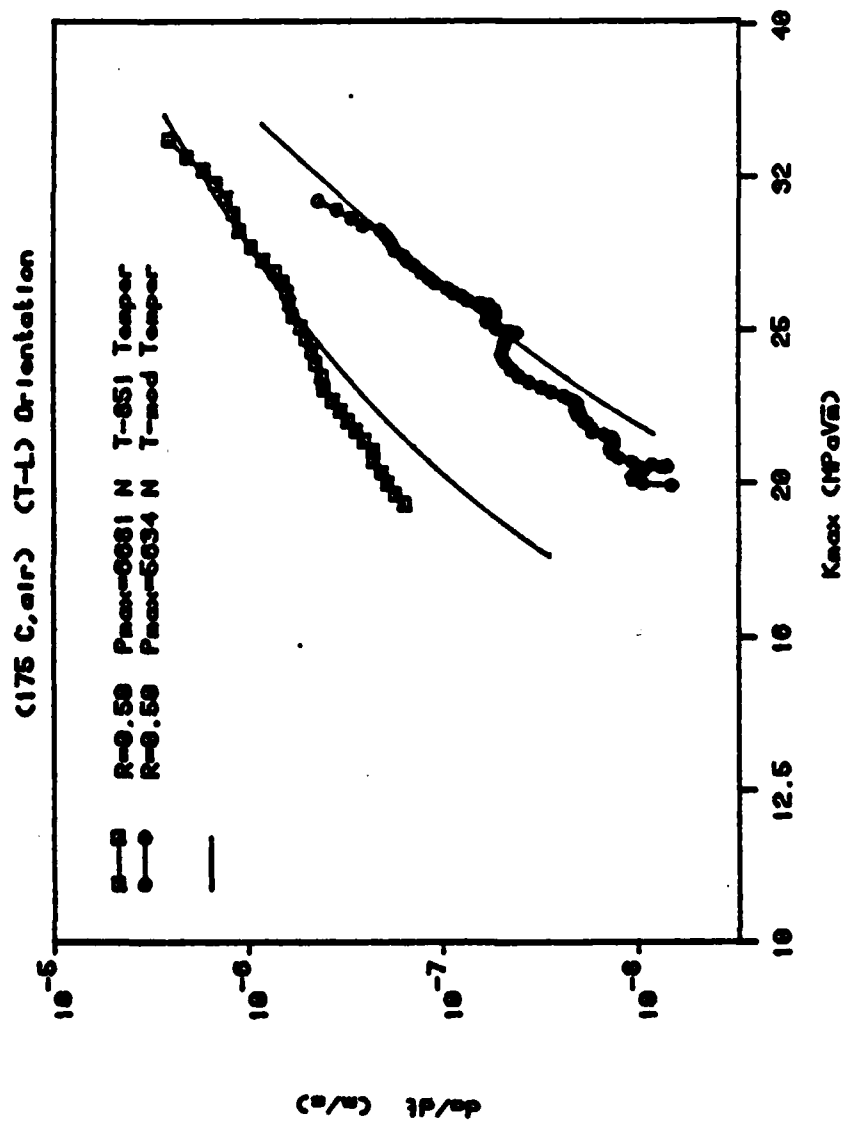


FIGURE (55) Comparison between the measured creep crack growth rates in 2219-T851 and 2219-Tmod at 175°C and the predictions of the model described in reference (55)

END

FILMED

6-84

DTIC